

UNIVERSITY OF SOUTHAMPTON

FACULTY OF ENGINEERING AND THE ENVIRONMENT

INSTITUTE OF SOUND AND VIBRATION RESEARCH

**NUMERICAL INVESTIGATION OF THE
TRUE SOURCES OF JET NOISE**

Samuel Sinayoko

Thesis for the degree of Doctor of Philosophy

October 2010

UNIVERSITY OF SOUTHAMPTON

ABSTRACT

FACULTY OF ENGINEERING AND THE ENVIRONMENT

INSTITUTE OF SOUND AND VIBRATION RESEARCH

Doctor of Philosophy

NUMERICAL INVESTIGATION OF THE TRUE SOURCES OF JET NOISE

by Samuel Sinayoko

This work is a fundamental study on the physical sources of aerodynamic noise. It is based on a combination of analytical and numerical signal processing techniques. A novel expression for the aerodynamic noise sources is proposed; it is valid for unbounded homentropic subsonic flows surrounded by a quiescent medium. This expression is based on the non-radiating components of the flow field. Such non-radiating components can be obtained numerically by using convolution filters. This is demonstrated for two problems. The first problem satisfies the linearised Euler equations and models a two-dimensional shear layer by using a parallel mean flow. The second problem deals with a laminar axisymmetric jet that satisfies the Navier–Stokes equations.

The sound sources are computed for the laminar jet problem. The noise sources based on two more classical acoustic analogies, in which the base flow corresponds either to the time-averaged part of the flow field or to a quiescent medium, are also computed for comparison. In all cases, the sources are validated by comparing the sound they generate with the exact solution. The new sound sources are found to have two important properties that make them more physical than sound sources based on classical acoustic analogies. Firstly, their amplitude is similar to that of the sound field. Secondly, they generate only sound. This contrasts with the properties of sources based on classical acoustic analogies, whose amplitudes are much larger than that of the sound field and which generate hydrodynamic fluctuations in addition to sound.

*To Koman and Lucie
for the love they gave me*

Contents

1	Introduction	1
1.1	Motivation	1
1.2	Acoustic analogies	3
1.2.1	Lighthill's analogy	3
1.2.2	On the issues regarding existing acoustic analogies	4
1.3	Physical sources of sound	5
1.4	Filtering of radiating components	5
1.5	Acoustic perturbation equations	6
1.6	Source mechanisms in subsonic jets	7
1.7	Scope of the thesis	9
1.8	Key objectives of the thesis	10
2	Aerodynamic noise sources	11
2.1	Sources based on a non-radiating base flow	12
2.1.1	Flow decomposition	12
2.1.2	Source definition	12
2.1.3	Comparison with Goldstein's approach	15
2.1.4	Physical interpretation for the propagation operator	16
2.2	Sources based on a time averaged base flow	17
2.2.1	Flow decomposition	17
2.2.2	Source definition	17
2.2.3	Comparison with expressions from the literature	19
2.3	Source based on a quiescent base flow	20
2.4	Conclusion	20
3	Non-radiating filters	21
3.1	Radiation criterion	22
3.1.1	Radiating components in a 3D flow field	22
3.1.2	Radiating components in a 2D flow field	24
3.2	Definitions	24

3.2.1	Non-radiating filter	24
3.2.2	Optimal non-radiating filter	26
3.3	Differential filter	26
3.4	Convolution filters	27
3.4.1	Theory	27
3.4.2	Numerical issues	28
3.4.3	Filtering strategies	32
3.5	Filtering of a two-dimensional shear layer	34
3.5.1	Problem description and implementation	34
3.5.2	Differential filter	35
3.5.3	Convolution filters	35
3.5.4	High pass filter with Hann window	39
3.6	Summary	41
4	Sources of sound in a laminar jet	47
4.1	Problem description	48
4.2	Flow analysis	49
4.2.1	Grids	49
4.2.2	Steady flow	49
4.2.3	Unsteady flow	51
4.2.4	Frequency analysis	52
4.2.5	Wavenumber analysis	56
4.3	Flow filtering	58
4.3.1	Algorithm	58
4.3.2	Filter definition	61
4.3.3	Results	61
4.4	NRBF sources	66
4.4.1	Algorithm	66
4.4.2	Results and discussion	67
4.4.3	Amplitude and location of the sound sources	73
4.4.4	Validation	74
4.4.5	Dominant source term	75
4.5	Effect of the size of the computational domain	77
4.5.1	Algorithm	79
4.5.2	Reducing size in the radial direction	80
4.5.3	Reducing size in the axial direction	80
4.5.4	Reducing size in both directions	82
4.6	Source based on a time averaged base flow	82
4.6.1	Algorithm	84

4.6.2	Results	85
4.6.3	Discussion	86
4.7	Source based on a quiescent base flow	90
4.7.1	Algorithm	90
4.7.2	Results and discussion	91
4.8	Conclusion	96
5	Conclusion	97
A	Hankel transform	101
A.1	Definition	101
A.2	Fourier transform of a radially symmetric signal in 2D	101
A.2.1	Scalar field	101
A.2.2	Vector field	103
A.3	Fourier transform of an axisymmetric signal in 3D	104
A.3.1	Scalar field	104
A.3.2	Vector field	104
B	Sources of sound in a laminar jet: additional results	105
B.1	Flow analysis	105
B.2	Flow filtering	112
B.3	NRBF sources	119
B.4	Source based on a time averaged base flow	129
Bibliography		133

CONTENTS

List of Figures

3.1	Radiating sphere for a 3D flow variable in the wavenumber domain	23
3.2	Radiation circle for a 2D flow variable in the wavenumber domain	25
3.3	Numerical Fourier transform of a sine wave and spectral leakage	30
3.4	Analytical Fourier transform of a sine wave	31
3.5	Schematic of a discrete one dimensional convolution product	31
3.6	Convolution product and fast Fourier transform: boundary effects	32
3.7	Illustration of two filtering strategies	33
3.8	Pressure field for benchmark problem	35
3.9	Filtered pressure field using the d'Alembertian operator	36
3.10	Fourier transform magnitude using a rectangular window	37
3.11	Fourier transform magnitude using a Hann window	38
3.12	Rectangular and Hann windows	38
3.13	Filtered pressure field magnitude in wavenumber domain (rectangular window, Gaussian filter)	39
3.14	Hann windowed pressure field	40
3.15	Fourier transform magnitude of Hann windowed pressure field	40
3.16	Pressure and filtered pressure using a Gaussian filter	42
3.17	Pressure and filtered pressure using a high pass filter and a Hann window.	43
3.18	Corrected pressure and filtered pressure for a high pass filter and a Hann window.	44
3.19	Pressure and filtered pressure for a hybrid filter.	45
4.1	Initial grid and interpolation grid in radial direction	50
4.2	Steady part of axial momentum ρu	50
4.3	Profiles of $(\rho u)_0$ for $z = 0$, $z = 5$ and $z = 10$	51

4.4	Pseudo-colour plot and directivity of unsteady modified pressure $\pi - \pi_0$	52
4.5	Profiles of unsteady modified pressure $\pi - \pi_0$	52
4.6	PSD of modified pressure at point $(z,r) = (40, 20)$	53
4.7	Instantaneous frequency decomposition of modified pressure π at $t = 157.18$	55
4.8	Unsteady pressure profiles of π compared to $\pi_{1.0}$, $\pi_{1.2}$ and $\pi_{2.2}$	56
4.9	Magnitude of the Fourier transform of $\pi_{1.0}$, $\pi_{1.2}$ and $\pi_{2.2}$ at $t = 157.18$ in the wavenumber domain	57
4.10	Algorithm (1): $q(z, r, t) \rightarrow q_{\omega_r}(z, r, t)$	60
4.11	Algorithm (2): $q_{\omega_r}(z, r, t) \rightarrow q'_{\omega_r}(z, r, t)$	60
4.12	Algorithm (3): $q'_{\omega_r}(z, r, t) \rightarrow q'(z, r, t)$	60
4.13	Gaussian radiating filter window	62
4.14	Radiating modified pressure at frequency 1.2 in the wavenumber domain	62
4.15	Pseudo colour plots and profiles of $\bar{\pi}_{1.2}$ and $\pi_{1.2}$	64
4.16	Pseudo colour plots and profiles of $\bar{\pi}$ and π	65
4.17	Source vector $(\mathbf{e})_{1.2}$ in the space and wavenumber domains	68
4.18	Source $(E_1)_{1.2}$ in wavenumber domains: varying contour levels	69
4.19	Radiating source vector $(\mathbf{e}'_{1.2})$ in the space and wavenumber domains	71
4.20	NRBF sources $(f_{1z})_{1.2}$ and $(f_{1r})_{1.2}$ at frequency 1.2	72
4.21	Evolution of axial source $(f_{1z})_{1.2}$ with time	73
4.22	Validation of the NRBF source, $\pi'_{1.2}$	76
4.23	Modified Pressure radiating from each of the terms in $(f_{1z})_{1.2}$ and $(f_{1z})_{1.2}$	78
4.24	Directivities of $\pi_{1.2}$ for terms $(e_1)'_{1.2}$ and $(e_4)'_{1.2}$ compared the directivity of the DNS solution	79
4.25	NRBF sources $(f_{1z})_{1.2}$ and $(f_{1r})_{1.2}$ at frequency 1.2 for smaller domains in the r -direction	81
4.26	NRBF sources $(f_{1z})_{1.2}$ and $(f_{1r})_{1.2}$ at frequency 1.2 for smaller domains in the z -direction	83
4.27	NRBF sources $(f_{1z})_{1.2}$ and $(f_{1r})_{1.2}$ at frequency 1.2 for smaller domains both directions	84
4.28	TABF source, f_{2z} and $(f_{2z})_{1.2}$	85
4.29	time averaged sound source, f_{2r} and $(f_{2r})_{1.2}$	86
4.30	Validation of the time averaged sound source, $\pi_{1.2}$	87
4.31	Modified Pressure radiating from each of the terms in $(f_{2z})_{1.2}$ and $(f_{2z})_{1.2}$	89

4.32 Modified Pressure radiating from each of the terms in $(f_{2z})_{1.2}$ and $(f_{2z})_{1.2}$	90
4.33 QBF source, f_{3z} and $(f_{3z})_{1.2}$	92
4.34 QBF source, f_{3r} and $(f_{3r})_{1.2}$	93
4.35 Validation of the QBF sources, $\pi_{1.2}$	94
4.36 Modified Pressure radiating from each of the terms in $(f_{3z})_{1.2}$ and $(f_{3z})_{1.2}$	95
A.1 cylindrical polar coordinate system in x-domain	101
A.2 cylindrical polar coordinate system in k-domain	102
B.1 Time averaged density, radial momentum and pressure fields	106
B.2 Error l_1 between time averaged flow variables and the pre- scribed mean flow of Stromberg.	107
B.3 Snapshots of density, axial momentum and radial momentum	108
B.4 Instantaneous flow directivity for the density, axial momen- tum and radial momentum fields	109
B.5 Profiles of density, axial momentum and radial momentum in the near field and far field.	109
B.6 pseudo-colour plots and profiles of π_{ω_r} for $\omega_r = 1.0, 1.2$ and 2.2 in the near-field.	110
B.7 Fourier transforms in space of q_{ω_r} for $q \in \{\rho, \rho u, \rho v\}$ and $\omega_r \in \{1.0, 1.2, 2.2\}$	111
B.8 Radiating and non-radiating components of Q_{ω_r} in the wavenum- ber domain	113
B.9 Pseudo colour plots and profiles of $\bar{\pi}_{1.0}$ and $\pi_{1.0}$	114
B.10 Pseudo colour plots and profiles of $\bar{\pi}_{2.2}$ and $\pi_{2.2}$	115
B.11 Pseudo colour plots and profiles of $\bar{\rho}$ and ρ	116
B.12 Pseudo colour plots and profiles of $\bar{\rho u}$ and ρu	117
B.13 Pseudo colour plots and profiles of $\bar{\rho v}$ and ρv	118
B.14 Radiating source vector ($\mathbf{q}'_{1.0}$) in the space and wavenumber domains	120
B.15 NRBF sources $(f_{1z})_{1.0}$ and $(f_{1r})_{1.0}$ at frequency 1.0	121
B.16 Radiating source vector ($\mathbf{q}'_{2.2}$) in the space and wavenumber domains	122
B.17 NRBF sources $(f_{1z})_{2.2}$ and $(f_{1r})_{2.2}$ at frequency 2.2	123
B.18 Validation of the NRBF source, $\pi'_{1.0}$	124
B.19 Validation of the NRBF source, $\pi'_{2.2}$	125
B.20 Validation of the NRBF source, $\rho'_{1.2}, (\rho u)'_{1.2}, (\rho v)'_{1.2}$	126

LIST OF FIGURES

B.21 Validation of the NRBF source, $\rho'_{1.0}$, $(\rho u)'_{1.0}$, $(\rho v)'_{1.0}$	127
B.22 Validation of the NRBF source, $\rho'_{2.2}$, $(\rho u)'_{2.2}$, $(\rho v)'_{2.2}$	128
B.23 Validation of the time averaged sound source, $\rho'_{1.2}$, $(\rho u)'_{1.2}$, $(\rho v)'_{1.2}$	130

List of Tables

3.1	Flow parameters for the two-dimensional shear layer problem	36
4.1	Error l_∞ between time averaged flow and the mean flow of Stromberg.	50
4.2	Convection velocity u_{c0} as a function of ω based on $ \pi_\omega $	56
4.3	Non-radiating wavenumber, radiating wavenumber $ \mathbf{k} = \omega/c_\infty$ and convection velocity u_c for the radiating frequencies	58
4.4	Peak value of radiating variables and non-radiating variables within the flow.	63
4.5	Peak locations of radiating and non-radiating variables within the flow.	66
4.6	Phase velocity of NRBF source $(f_{1z})_{1,2}$	73

Acknowledgements

I would like to sincerely thank Christophe Bailly, from Ecole Centrale de Lyon, as well as Rod Self and Chris Morfey, from the University of Southampton, for accepting to be my examiners and to review this thesis.

I would also like to thank the Engineering and Physical Sciences Research Council for funding this project, and Rolls-Royce plc., for the extra and much appreciated financial support offered to me for the past three years.

I must stress the pleasure I have had to be working here at the Institute of Sound and Vibration Research, first as an MSc student and then as a PhD student. I would like to thank all the members of the Fluid Dynamics and Acoustics Group, for creating such a nice and friendly atmosphere. Many thanks in particular to all the students, with whom I have shared this adventure. I would also like to thank our group secretary, Sue Brindle, for being so helpful and efficient. I have had useful discussions with Paul White, to help me with the signal processing side of my work. Gwénaël Gabard has been particularly helpful regarding the computational side and I am very grateful for his patient answers to my numerous questions. Thank you also to Zhiwei Hu and Richard Sandberg for sharing with me their expertise on computational fluid dynamics. I would like to specially thank Chris Morfey, who has humbled me by accepting to follow my progress and has given me feedback and encouragements throughout my work. His enthusiasm has been a great source of inspiration and motivation. A heartfelt thank goes to Victoria Suponitsky, who has been crucial to the success of this research. She has provided the flow simulation on which much of the results are based, and I have enjoyed working with her. I would also like to thank Peter Jordan, who has kindly invited me to spend a few weeks in Poitiers for a collaboration. He too has been a source of inspiration. A special thank goes to Peter's student, Andre Cavalieri, for his thought provoking questions. They have helped improve some aspects of this work.

Most of all, I am very grateful to have had Anurag Agarwal as my supervisor. It has been a pleasure to work with him week after week, and to overcome

together the numerous obstacles that paved our way. I have greatly enjoyed his optimism and confidence, as well as his determination to attack such an arduous topic. He has been very supportive, even going so far as getting his brains (really) dirty when I was completely stuck. I thank him very much for his commitment and his enthusiasm.

Of course, I would probably not be in this position without the dedication and love of my parents Koman and Lucie, who gave me everything, and to whom I dedicate this work. I would also like to thank Margaret, who has been at my side since the beginning of this endeavor. She has followed the ups and downs of my progress day after day, and her support has been tremendous. For that, and for everything else, I am eternally grateful.

Declaration of authorship

I, Samuel Sinayoko, declare that the thesis entitled *Numerical investigation of the true sources of jet noise* and the work presented in the thesis are both my own, and have been generated by me as the result of my own original research. I confirm that:

- this work was done wholly or mainly while in candidature for a research degree at the University;
- where any part of this thesis has previously been submitted for a degree or any other qualification at this University or any other institution, this has been clearly stated;
- where I have consulted the published work of others, this is always clearly attributed;
- where I have quoted from the work of others, the source is always given. With the exception of such quotations, this thesis is entirely my own work;
- I have acknowledged all main sources of help;
- where the thesis is based on work done by myself jointly with others, I have made clear exactly what was done by others and what I have contributed myself;
- parts of this work have been published as:
 - (a) Sinayoko, S., Agarwal, A. (2010) On computing the physical sources of jet noise, *Proceedings of the 16th AIAA/CEAS Aeroacoustics Conference (31st AIAA Aeroacoustics Conference)*, Stockholm, Sweden, 7-9 June 2010, AIAA-2010-3962,
 - (b) Sinayoko, S., Agarwal, A. and Hu, Z. (2009) On separating propagating and non-propagating dynamics in fluid-flow equations, *Proceedings of the 15th AIAA/CEAS Aeroacoustics Conference (30th AIAA Aeroacoustics Conference)*, Miami, USA, 11-13 May 2009, AIAA-2009-3381.

Chapter 1

Introduction

Contents

1.1	Motivation	1
1.2	Acoustic analogies	3
1.2.1	Lighthill's analogy	3
1.2.2	On the issues regarding existing acoustic analogies	4
1.3	Physical sources of sound	5
1.4	Filtering of radiating components	5
1.5	Acoustic perturbation equations	6
1.6	Source mechanisms in subsonic jets	7
1.7	Scope of the thesis	9
1.8	Key objectives of the thesis	10

1.1 Motivation

Aircraft noise severely impacts the quality of life of residents living near airports and is a problem that will become even more pressing in the future, with air traffic forecast almost to double in the next two decades. One of the dominant sources of aircraft noise is jet noise. The noise radiated by the first jet engines, in the 1950s, was actually so strong that it threatened to jeopardise their future. This problem quickly became the focus of intense theoretical and experimental research, which led to the publication, in 1952, of the first theory of aerodynamic sound by Lighthill [1]. An important result of Lighthill's theory was that the power of the radiated sound scaled with the eighth power of the jet velocity. This allowed for the first time to understand the crucial importance of jet velocity on jet noise. The result was soon confirmed by experimental results. At the same time, manufacturers started to build high

bypass ratio engines, that have a lower jet-exit velocity for a given thrust. Although the main reason for developing high bypass engines was aerodynamic performance, it led to significant noise reductions. However, several important problems could not be readily tackled using Lighthill's theory. It did not take into account, for example, supersonic flows or the presence of solid boundaries. However, Lighthill's work offered a foundation that subsequent researchers could build on to solve such problems. Lighthill is therefore credited for being the father of modern aeroacoustics, the science which studies the generation and propagation of flow-induced sound.

After more than 50 years of research in aeroacoustics, controlling the sound radiated by turbulent jets remains difficult. One reason is that no consensus has been reached on how turbulent flows generate sound. A major obstacle is the lack of understanding of the physical sources of sound in a jet. Ideally, the physical sources of sound should be obtained directly from the flow field. This idea has been pursued by Goldstein [2], who derived an analytical formulation whereby sources approaching the physical sources of sound can be computed. The formulation can be seen as a generalized acoustic analogy based on a silent unsteady base flow. However, it has never been implemented numerically. The main challenge is the decomposition of the flow field into radiating and non-radiating components which is a necessary element of Goldstein's theory [2]. This decomposition requires to remove the radiating waves from the flow field without distorting the non-radiating waves. This is especially difficult because the radiating waves are usually several orders of magnitude smaller than the non-radiating waves [3]. If these challenges can be overcome, however, this technique could enable the direct computation of the aerodynamic noise sources. Such a tool has the potential to provide new insights and a better understanding of the noise generation mechanisms in jets, which can translate into efficient noise reduction strategies.

The rest of the chapter is organised as follows. In the next section various acoustic-analogy based theories for subsonic jet noise are presented. The objective is to explain where Goldstein's method fits among the different theories of aerodynamic noise. Goldstein's method is then reviewed with particular attention to the difficulties involved. Finally, a summary of the source mechanisms proposed in the literature is given and the key regions of the jet currently thought to be responsible for sound generation are reviewed. This review will serve to assess the advantages and drawbacks of the noise sources defined by Goldstein.

1.2 Acoustic analogies

1.2.1 Lighthill's analogy

As will be shown in section 1.2.2, the method behind the definition of the “physical sources” of sound by Goldstein follows closely that developed by Lighthill in his pioneering paper. It is therefore useful to understand Lighthill’s method. Lighthill [1] rearranged the conservation equations for mass and momentum to obtain an equation for the density perturbation. The left-hand side of that equation has the acoustic wave operator acting on the density perturbation, and the right-hand side takes the form of the double divergence of a tensor. Lighthill’s equation is exact since it is a simple rearrangement of conservation equations. Lighthill realized that the linear operator is the one governing the propagation of an acoustic perturbation in a quiescent medium, and that the right hand side could be seen as a source term driving that linear operator. He, therefore, recognized that the sound radiated to the far field by the flow was equivalent to that radiated in a quiescent medium by his newly defined source term. This recognition constitutes Lighthill’s acoustic analogy. Its usefulness requires the right hand side (the hydrodynamic part of the flow) to be independent of the acoustic radiation: acoustic feedback is neglected. This hypothesis is thought to be sufficient for most subsonic flows, including those of interest in the present work, but in cases where acoustic coupling plays a significant role, another formulation would be required.

Lighthill also gave a simple interpretation of his source term. For low Mach numbers, i.e when the flow speed is small compared with the speed of sound, the source can be seen as a distribution of incoherent (random distribution) eddies behaving like quadrupoles. More precisely, the coherence length scale is much smaller than the acoustic wavelength. Assuming that the points within each eddy are in phase, and that the eddies’ characteristic velocity and characteristic length scale respectively with jet exit velocity and jet diameter, Lighthill showed that the radiated sound power scaled with the eighth power of jet velocity. This result was soon validated experimentally (see, for example, references [4, 5]). Lighthill also realized the consequence of the convection of sound sources with the flow. He showed that sound was amplified in the downstream direction and that its spectrum was Doppler shifted, i.e the frequency increased in the downstream direction and decreased in the upstream direction. This led to the classical understanding of the sound sources in a jet as compact incoherent quadrupoles convecting with the flow.

1.2.2 On the issues regarding existing acoustic analogies

The propagation of sound in a complex flow is affected by refraction, due to velocity gradients and variations in the speed of sound, and scattering, due to unsteadiness in the flow field such as of vortical structures. The propagation of sound in a jet is complex. A key advantage of Lighthill's acoustic analogy is to simplify the problem by finding equivalent sources which radiate in a uniform medium at rest. In such a medium, propagation is straightforward; it becomes possible to predict the sound radiated to the far field, provided the equivalent sources are estimated with sufficient accuracy. However, this comes at a cost: complex propagation effects such as refraction and scattering of sound by the flow are hidden in the equivalent source term. An important part of Lighthill's source term is, therefore, concerned with sound propagation rather than sound generation. Using this source term to draw conclusions on the sound generation mechanisms requires great care: the part of the equivalent source term concerned with sound generation must be identified and separated from the one concerned with sound propagation. Cabana et al. [6] attempted to carry out such a decomposition but found it difficult to identify the physical sources of noise.

To overcome the complexity of modelling propagation effects in the source term, some investigators derived acoustic analogies using more realistic base flows. One of the most popular analogies was obtained by Lilley [7], who used a parallel base flow, thereby leaving most of the refraction effects in the linear operator instead of the source term. The linear operator he used was the Pridmore-Brown operator [8], which describes sound propagation through a parallel flow. It is harder to solve than the wave operator present in Lighthill's analogy. Furthermore, the Pridmore-Brown operator contains instability wave modes which, when excited by the flow, can completely overwhelm the physical solution. These drawbacks were identified by Ribner [9] who concluded that they outweighed the advantages brought by Lilley's analogy regarding the improved realism of the sound sources. Besides, parallel flows are still a simplification of real flows and the corresponding sources are still equivalent sources.

Recent acoustic analogies, such as the one proposed by Bogey *et al.* [10] use the linearized Euler operator on the left hand side to remove the mean flow refraction effects from the source, and to allow for non-parallel flows. This approach is seen as an improvement over previous analogies with regard to the physical interpretation of the sound sources. However, as with previous acoustic analogies, only a small part of the computed sound sources actually

generates sound. It is unclear how to identify this part.

Sources based on classical acoustic analogies suffer from other drawbacks. First, they generate hydrodynamic waves in addition to acoustic waves; ideally, the physical sources of sound should generate only acoustic waves. Second, sources based on acoustic analogies depend on the acoustic variables they are trying to predict. This problem could be overcome by defining sources that are based only on hydrodynamic components.

1.3 Physical sources of sound

Goldstein [2] proposes a method whereby most propagation effects are removed from the source term. He assumes the existence of a linear filter, that removes the radiating components of the flow and leaves the non-radiating components unchanged. In principle this filter can be applied to a complex flow to obtain a non-radiating base flow. In practise this base flow should be very close to the original flow, since the radiating components of the flow are believed to constitute only a small part of the total flow field. Goldstein derives the equations governing the non-radiating base flow and those governing the radiating flow. The radiating flow satisfies the linearised Navier-Stokes equations with some additional source terms, which depend mainly on the non-radiating flow. Because the base flow is made of all the non-radiating components, most propagation effects are taken out of the source terms. Goldstein therefore argues that these source terms should be close to the physical sources of sound. Note, however, that Goldstein's sources still contain some radiating components. Since the physical sound sources are expected to be a small byproduct of the hydrodynamic field, they should be a function of the hydrodynamic field only. One objective of the thesis is to improve Goldstein's work and derive a simpler and more accurate definition of the sources of sound.

1.4 Filtering of radiating components

The filtering operation is the very foundation of Goldstein's method [2]. The silent part of the flow must be identified to compute the noise sources. Theoretically, this can be done by filtering out the acoustically radiating components; one of the key objectives of this thesis is to demonstrate how such filtering procedure can be achieved in nonlinear free shear flows.

For a free flow surrounded by a quiescent medium, the radiating compo-

nents are best described in the frequency–wavenumber domain, where they satisfy the dispersion relation $|\mathbf{k}| = |\omega|/c_\infty$, where \mathbf{k} is the wavenumber, ω the frequency and c_∞ the far field speed of sound. A mathematical proof of this result is given by Crighton [11]. The proof utilises Lighthill’s acoustic analogy to identify the radiating components of the source, but the result is applicable to any unbounded flow. By applying a linear filter to Lighthill’s equation and following Crighton’s proof, Goldstein shows that a filter which removes the components satisfying $|\mathbf{k}| = |\omega|/c_\infty$ renders the flow completely silent.

Interestingly, from the literature, the full criterion has never been used to identify the non-radiating part of a flow field. Nevertheless, several investigators have used a simplified version of it, that relies only on the axial wavenumber k_x . Freund [12] used the criterion $k_x < \omega/c_\infty$ to retain the radiating components and $k_x > \omega/c_\infty$ to retain the non-radiating components. He was followed by Cabana et al. [6] and Tinney and Jordan [13] who applied the same criteria to identify the radiating components of the flow. These authors rely on a commonly made analogy with the wavy-wall problem, for which the ability to radiate sound depends on the convection speed of the wall: if the wall is supersonic, i.e $k_x < \omega/c_\infty$, then sound radiates in a particular direction, and if it is subsonic, i.e $k_x > \omega/c_\infty$, the wall generates evanescent waves which do not radiate to the far field. It is important to note that the wavy-wall criterion is incomplete for two- and three-dimensional flows, because it does not take into account the effect of the transverse wavenumbers k_y and k_z .

Although the radiation criterion $|\mathbf{k}| = |\omega|/c_\infty$ is clear mathematically, it is difficult to explain physically because it corresponds to the dispersion relation for acoustic waves in a quiescent medium. Thus, it is sometimes argued that this dispersion relation is only valid in the far field. It is important to note, however, that it is incorrect to restrict a particular dispersion relation to a finite region of the flow. Dispersion relations are obtained by taking the Fourier transform (in space and time) of the flow equations. Fourier transforms are global: they depend on the value of the signal throughout the entire domain and for all times. Consequently, dispersion relations are also global, and cannot be associated with a particular region of the flow field. This explains why it is difficult to give a simple physical interpretation to the radiation criterion.

1.5 Acoustic perturbation equations

An alternative way of identifying the physical sources of sound has been proposed by Ewert and Schröder [14]. The authors obtain several systems of

linear equations, called the acoustic perturbation equations (APE), that govern the propagation of acoustic waves through a non-uniform base flow. The corresponding linear operator does not support the convection of entropic or vortical waves and is therefore stable. In the fundamental system of equations (APE 1), the velocity field is split into mean, vortical and acoustic parts. However, the authors do not explain how to carry out such a decomposition in high speed flows. Indeed, they focus on sound propagation rather than sound generation: an alternative system of equations (APE 4), for which flow decomposition is unnecessary, can be used to estimate the sound radiating to the far field.

Computing the sound sources as defined by the APE 1 system of equations requires several steps. First, the irrotational part of the source vector associated with a quiescent base flow is computed. This is done by solving several Poisson equations. Second, the source terms are decomposed to remove some of the propagation effects (the convection and refraction of acoustic components by the mean flow). However, propagation effects that involve the interaction of vorticity with acoustic waves are neglected. Unlike this method, Goldstein's approach retains all propagation effects. It will be the one pursued in this thesis. Nevertheless, both approaches are closely related.

1.6 Source mechanisms in subsonic jets

The classical view based on acoustic analogies is that jet noise is generated by incoherent multipoles, the radiating sound being subject to convective amplification and interactions with the mean flow [15]. This view started to change in the 1960s and 1970s when coherent structures were measured in jets using flow visualization and two-point correlation techniques. Crow and Champagne [16], for example, found such coherent structures in jets acoustically forced by a loudspeaker, by measuring velocity fluctuations with hot wires, while Fuchs [17] and Armstrong [18] measured coherent structures in unforced jets using pressure probes. Mollo-Christensen *et al.* [19] suggested that two different noise generation mechanisms might be responsible for jet noise: one mechanism dominating at small angles to the jet axis (less than 40°) and another one dominating at larger angles (more than 50°). Their result was based on the different similarity spectra of the sound field measured for small and large angles to the jet axis.

The idea of two different noise mechanisms has been reinforced more recently by Tam *et al.* [20] and Viswanathan [21], who identified two independent self-similar spectra from a large experimental database of sound spectra.

The idea is that turbulent jets involve both fine scales, which radiate sound over a broad range of frequencies away from the jet axis, and large scales, which radiate sound close to the jet axis. Interestingly, Viswanathan's results (for coaxial jets) suggest that the spectral shape of the fine scales is independent of the jet geometry whereas the opposite is true for the spectral shape of the large scales.

Some numerical studies also support the idea of two different source mechanisms. Bogey and Bailly [22] simulated a Mach 0.9 jet of Reynolds number 65000 using Large Eddy Simulation (LES). They found that the overall sound pressure level was in good agreement with the experimental results of Mollo-Christensen *et al.* [19] and Stromberg *et al.* [23] for angles close to the jet axis, despite the very different Reynolds numbers used in these two experiments (5.4×10^5 for Mollo-Christensen's and 3600 for Stromberg's), whereas more scatter could be seen between the experiments for larger angles: this suggests that the sound radiating from fine scales depends on the Reynolds number whereas the sound radiating from large scales is rather insensitive to it. In addition, the shape of the sound spectra measured respectively by Stromberg and Mollo-Christensen at 30° to the jet axis, as a function of the Strouhal number St , are also very similar; both spectra reach their maximum for $St \approx 0.2$. Thus, the small scales play a greater role as the Reynolds number increases until the jet becomes fully turbulent. On the contrary, noise generation by large scales depends mostly on the Mach number and on the jet geometry. These ideas are also supported by a numerical study by Bogey and Bailly [24], wherein the noise spectra from jets of different Mach numbers (0.6 and 0.9) and different Reynolds numbers (between 1700 to 4×10^5) are examined.

Several studies, both experimental and numerical, have used correlations between the far field and the jet turbulence to identify the location of the noise sources. The experimental studies of Juve *et al.* [25], Schaffar [26] and Panda [27, 28], as well as the numerical studies of Bogey *et al.* [29, 24] have all found a strong correlation between the sound radiating to the far field at angles close to the jet axis and the region near the end of the potential core. It will therefore be interesting to compare the position of the noise sources based on Goldstein's method with respect to the end of the potential core.

Although several studies identify the end of the potential core as a key region for sound radiation from large scale structures, the underlying mechanism remains poorly understood. Significant advances have been made however by Sandham *et al.* [30] and Suponitsky *et al.* [31], who suggest that the dominant source mechanism involves nonlinear interactions between differ-

ent frequency components. These interactions are such that the difference frequency corresponds to a Strouhal number of 0.2, which is the dominant frequency measured at angles around 30° to the jet axis in several experiments (Stromberg *et al.* [23], Viswanathan [32]). A similar result was actually demonstrated as early as 1979 by Ronneberger and Ackermann [33], who excited a subsonic jet by plane waves at two different frequencies and measured significant sound radiation, at the difference frequency, amplified by as much as 30dB compared to the zero flow case. An explanation for these results is that nonlinear effects between the most unstable frequencies lead to the appearance of a high amplitude spatially modulated wavepacket which can be an efficient sound radiator [31].

One notable feature of the work of Suponitsky *et al.* [31] is the forcing term that is added to the right hand side of the Navier–Stokes equations to maintain the mean flow, which allows the author to follow the evolution of the small disturbances. Most importantly the flow is only weakly non-linear so that the mean flow is largely unaffected by the disturbances. The advantage is that only a small number of frequencies and wavenumbers are involved. This limits the complexity of the problem compared to a full direct numerical simulation (DNS) or large eddy simulation (LES), where a broad range of frequencies and wavenumbers would be involved. This flow is a good test case for computing the sources of sound: it captures a sound generation mechanism which is thought to be significant in subsonic jets over a large range of Reynolds numbers, while remaining more tractable than three dimensional DNS or LES. However, because the Reynolds number is small (3600), only the sound sources linked to the large coherent structures are expected to be captured, not the ones related to small turbulent structures.

1.7 Scope of the thesis

The flows studied in this thesis are assumed to have the following characteristics:

- free flow with no solid boundaries, surrounded by a quiescent medium
- isentropic
- subsonic
- low Reynolds number ($< 10^4$)

These conditions are sufficient to capture the sound generation from large scale structures in subsonic jets. Other effects, due for example to the presence of solid boundaries [34], temperature gradients [35] or supersonic speeds [36] will be ignored for simplicity.

1.8 Key objectives of the thesis

The first objective of this thesis is to derive an expression for the sources of sound that is independent of the radiating variables and that generates only acoustic waves. It should be free from the propagation effects that affect classical acoustic analogies. Such expression will be obtained by building on Goldstein's work. Goldstein's sources satisfy most of the desired properties but are complex and still depend on the radiating variables. The aim will be to derive an expression that is both simpler and more accurate.

The physical sources of sound are based solely on the hydrodynamic part of the flow. The second objective is to show that it is possible to identify the hydrodynamic part of the flow by designing non-radiating filters. Both differential filters, defined in the time domain, and convolution filters, applied in the Fourier domain, will be studied; they will be tested on the linear flow field proposed by Agarwal *et al.* [37].

Finally, the entire method will be implemented numerically to identify the sound sources in one of the laminar subsonic jets obtained by Suponitsky *et al.* [31]. These sources will be validated by letting the sound they generate propagate to the far field and by comparing the result to the original solution. The physical properties of the sources, such as their location, amplitude and dynamics will also be investigated. These sources will be compared to those based on classical acoustic analogies.

Chapter 2

Aerodynamic noise sources

Contents

2.1	Sources based on a non-radiating base flow	12
2.1.1	Flow decomposition	12
2.1.2	Source definition	12
2.1.3	Comparison with Goldstein's approach	15
2.1.4	Physical interpretation for the propagation operator	16
2.2	Sources based on a time averaged base flow	17
2.2.1	Flow decomposition	17
2.2.2	Source definition	17
2.2.3	Comparison with expressions from the literature	19
2.3	Source based on a quiescent base flow	20
2.4	Conclusion	20

In section 2.1, in the spirit of Goldstein's work [2], an expression for the sources of aerodynamic noise is derived. It is based on a non-radiating base flow (NRBF) and the corresponding sources will hereafter be referred to as the NRBF sources. The expression assumes the possibility of decomposing the flow into its radiating and non-radiating components. Such decomposition can be achieved by using optimal non-radiating filters, which are studied in chapter 3. Section 2.2 shows how to derive an expression for the sources of aerodynamic noise based on a time-average base flow (the TABF sources). This expression is similar to the one derived by Bogey *et al.* [10]. Finally, section 2.3 shows how to derive an expression for the sources of aerodynamic sound based on a quiescent base flow (the QBF sources). This expression is equivalent to the one derived by Lighthill[1]. The different sources defined in this chapter will be applied to a high speed subsonic jet in chapter 4.

2.1 Sources based on a non-radiating base flow (NRBF)

2.1.1 Flow decomposition

For an unbounded flow-field surrounded by a quiescent ambient medium, the radiating components are those which satisfy the dispersion relation $|\mathbf{k}| = |\omega|/c_\infty$ (see Crighton [11] or Goldstein [2]), where \mathbf{k} denotes the wavenumber, ω the angular-frequency and c_∞ the ambient speed of sound. The non-radiating components are those which do not satisfy the above dispersion relation.

As pointed out by Goldstein [2], it is difficult to identify the acoustic components within the unsteady flow region. For definiteness, the acoustic components are identified with the radiating part of the flow field, which has been defined in the preceding paragraph. The hydrodynamic field is considered to be the unsteady part of the non-radiating field.

Let \mathcal{L} be a linear filter that captures the entire non-radiating part of a flow variable. Such filters are called optimal non-radiating filters and are studied in chapter 3. Any flow variable q can then be decomposed as

$$q = \bar{q} + q', \quad (2.1)$$

where $\bar{q} \equiv \mathcal{L}q$ represents the non-radiating part of q and q' contains only the radiating components. The radiating components can also be obtained directly by applying the linear filter \mathcal{L}' defined as

$$\mathcal{L}' \equiv \mathcal{I} - \mathcal{L}, \quad (2.2)$$

where \mathcal{I} denotes the identity operator.

2.1.2 Source definition

The flow variables satisfy the Navier–Stokes equations:

$$\frac{\partial \rho}{\partial t} + \frac{\partial}{\partial x_j} \rho v_j = 0, \quad (2.3)$$

$$\frac{\partial}{\partial t} \rho v_i + \frac{\partial}{\partial x_j} \rho v_i v_j + \frac{\partial p}{\partial x_i} = \frac{\partial}{\partial x_j} \sigma_{ij}, \quad (2.4)$$

where ρ , p and $\mathbf{v} = (v_i)$ denote the density, pressure and flow velocity, and σ_{ij} the viscous stress tensor. The flow is assumed to be homentropic, so that

$\sigma_{ij} = 0$. For a perfect gas, the energy equation can be written as [38]

$$\frac{\partial p}{\partial t} + v_j \frac{\partial p}{\partial x_j} + \gamma p \frac{\partial v_j}{\partial x_j} = 0. \quad (2.5)$$

Introducing the variable $\pi \equiv p^{1/\gamma}$ allows us to rewrite (2.4) and (2.5) as [35]

$$\frac{\partial}{\partial t} \rho v_i + \frac{\partial}{\partial x_j} \rho v_i v_j + \frac{\partial}{\partial x_i} \pi^\gamma = 0, \quad (2.6)$$

$$\frac{\partial \pi}{\partial t} + \frac{\partial}{\partial x_j} \pi v_j = 0. \quad (2.7)$$

Applying \mathcal{L}' to (2.3), (2.6) and (2.7) gives the governing equations for the radiating components:

$$\frac{\partial \rho'}{\partial t} + \frac{\partial}{\partial x_j} (\rho v_j)' = 0, \quad (2.8)$$

$$\frac{\partial}{\partial t} (\rho v_i)' + \frac{\partial}{\partial x_j} (\rho v_i v_j)' + \frac{\partial}{\partial x_i} (\pi^\gamma)' = 0, \quad (2.9)$$

$$\frac{\partial \pi'}{\partial t} + \frac{\partial}{\partial x_j} (\pi v_j)' = 0. \quad (2.10)$$

Each of the above equations are rearranged to obtain an operator that is linear in the radiating dependent variables $\{\rho', (\rho v_i)'\}$ and $\{\pi'\}$ on the left-hand side. In (2.9), the term $\rho v_i v_j$ can be expanded by decomposing each of the flow variables using (2.1):

$$\rho v_i v_j = \frac{\rho v_i \rho v_j}{\rho} \quad (2.11)$$

$$= \frac{\overline{\rho v_i} \overline{\rho v_j}}{\bar{\rho}} + \frac{\overline{\rho v_j}}{\bar{\rho}} (\rho v_i)' + \frac{\overline{\rho v_i}}{\bar{\rho}} (\rho v_j)' - \frac{\overline{\rho v_i} \overline{\rho v_j}}{\bar{\rho}^2} \rho' + O(\rho'^2), \quad (2.12)$$

$$= \bar{\rho} \tilde{v}_i \tilde{v}_j + \tilde{v}_j (\rho v_i)' + \tilde{v}_i (\rho v_j)' - \tilde{v}_i \tilde{v}_j \rho' + O(\rho'^2), \quad (2.13)$$

where

$$\tilde{v}_i = \frac{\overline{\rho v_i}}{\bar{\rho}}, \quad (2.14)$$

so that \tilde{v}_i represents Favre-averaged v_i , and where $O(\rho'^2)$ represents terms that are at least quadratic in the radiating variables. Because the radiating part of the flow is normally several orders of magnitude smaller than the non-radiating part, these higher order terms are expected to be small and will be

neglected. Applying \mathcal{L}' to (2.13) gives

$$(\rho v_i v_j)' \approx \underbrace{(\bar{\rho} \tilde{v}_i \tilde{v}_j)' + (\tilde{v}_j (\rho v_i)' + \tilde{v}_i (\rho v_j)' - \tilde{v}_i \tilde{v}_j \rho')'}_{(a)} \quad (2.15)$$

A one-way coupling is assumed between hydrodynamics and acoustics: the hydrodynamic field is responsible for the production of sound but the sound field does not affect the hydrodynamic field. The source of sound must therefore be independent of the radiating components. The only terms satisfying this requirement are those in group (b). The terms in group (a) involve a radiating component interacting with the non-radiating base flow. These terms represent propagation effects such as refraction and can be excluded from the source. The other non-linear term in (2.9) is $(\pi^\gamma)'$ which can be decomposed as follows:

$$\pi^\gamma = (\bar{\pi} + \pi')^\gamma = \bar{\pi}^\gamma + \gamma \bar{\pi}^{\gamma-1} \pi' + O(\pi'^2), \quad (2.16)$$

$$(\pi^\gamma)' \approx \underbrace{(\bar{\pi}^\gamma)' + (\gamma \bar{\pi}^{\gamma-1} \pi')'}_{(a)} \quad (2.17)$$

However, π^γ can also be expressed as

$$\pi^\gamma = p = \bar{p} + p', \quad (2.18)$$

so, by identifying the zeroth and first order terms between (2.16) and (2.18),

$$\bar{p} = \bar{\pi}^\gamma, \quad p' \approx \gamma \bar{\pi}^{\gamma-1} \pi'. \quad (2.19)$$

From (2.19) ones can write $(\bar{\pi}^\gamma)' = (\bar{p})' = 0$, so the source term (b) of equation (2.17) is equal to zero.

Similarly, in equation (2.10), $(\pi v_j)'$ can be decomposed as follows

$$(\pi v_j)' \approx \underbrace{(\bar{\pi} \tilde{v}_j)' + \left(\frac{\bar{\pi}}{\bar{\rho}} (\rho v_j)' + \tilde{v}_j \pi' - \frac{\bar{\pi}}{\bar{\rho}} \tilde{v}_j \rho' \right)'}_{(a)} \quad (2.20)$$

Since the flow is assumed to be homentropic,

$$p = \alpha \rho^\gamma, \quad \bar{p} = \alpha \bar{\rho}^\gamma, \quad p' = \alpha \gamma \bar{\rho}^{\gamma-1} \rho', \quad (2.21)$$

where α is a constant. From (2.19), (2.21) and (2.14), it can be seen that

$$(\bar{\pi} \tilde{v}_j)' = \alpha^{1/\gamma} (\bar{\rho} \tilde{v}_j)' = \alpha^{1/\gamma} (\bar{\rho} v_j)' = 0, \quad (2.22)$$

so the source term (b) in equation (2.20) is equal to zero.

Equations (2.8–2.10) can be rearranged by pushing the sound source (b) of (2.15) to the right hand side, and leaving the interaction terms (a) on the left hand side, which gives

$$\frac{\partial \rho'}{\partial t} + \frac{\partial}{\partial x_j} (\rho v_j)' = 0, \quad (2.23)$$

$$\frac{\partial}{\partial t} (\rho v_i)' + \frac{\partial}{\partial x_j} [\tilde{v}_j(\rho v_i)' + \tilde{v}_i(\rho v_j)' - \tilde{v}_i \tilde{v}_j \rho']' + \gamma \frac{\partial}{\partial x_i} [\bar{\pi}^{\gamma-1} \pi']' = f_{1i}, \quad (2.24)$$

$$\frac{\partial \pi'}{\partial t} + \frac{\partial}{\partial x_j} \left[\frac{\bar{\pi}}{\bar{\rho}} [(\rho v_j)' - \tilde{v}_j \rho'] + \tilde{v}_j \pi' \right]' = 0, \quad (2.25)$$

where the momentum equation source term f_{1i} is defined as

$$f_{1i} \equiv -\frac{\partial}{\partial x_j} (\bar{\rho} \tilde{v}_i \tilde{v}_j)' . \quad (2.26)$$

The equation shows that the noise source f_{1i} is a radiating quantity; this is expected because the left hand side of (2.23–2.25) depends linearly on the radiating variables. This means that f_{1i} produces only acoustic waves. Also, as expected, the source is expressed as a (nonlinear) function of only the non-radiating components: it is free of the dependant (radiating) variables. Therefore, this source should represent the true source of aerodynamically generated sound. These key features distinguish the present source from past representations based on acoustic analogies.

Note that for a homentropic flow, no sound source is present in the energy equation (2.25). In the general case, one would expect to have additional sources. Assuming homentropy is mostly applicable to low Mach number flows but the above procedure could be extended by using a more general energy equation.

2.1.3 Comparison with Goldstein's approach

The present approach differs from that of Goldstein [2]. It applies only to homentropic flows and is approximate because quadratic terms are neglected in radiating quantities. Secondly, a different set of dependent radiating variables is used. Nevertheless, the two sources are related. Assuming homentropy and neglecting quadratic terms in the radiating quantities, Goldstein's

sound sources (equation (2.13) in [39]) can be expressed as

$$f_{1gi} \approx \frac{\partial}{\partial x_j} (\bar{\rho} \bar{v}_i \bar{v}_j - \bar{\rho} \tilde{v}_i \tilde{v}_j) \quad (2.27)$$

Applying \mathcal{L} to equation (2.13) above and substituting the result into (2.27) gives,

$$f_{1gi} \approx \frac{\partial}{\partial x_j} \left(\bar{\rho} \tilde{v}_i \tilde{v}_j + \overline{\tilde{v}_j (\rho v_i)'} + \overline{\tilde{v}_i (\rho v_j)'} - \tilde{v}_i \tilde{v}_j \rho' - \bar{\rho} \tilde{v}_i \tilde{v}_j \right) \quad (2.28)$$

$$= \underbrace{-\frac{\partial}{\partial x_j} (\bar{\rho} \tilde{v}_i \tilde{v}_j)' \quad (a)}_{(a)} + \underbrace{\frac{\partial}{\partial x_j} \left[\overline{\tilde{v}_j (\rho v_i)'} + \overline{\tilde{v}_i (\rho v_j)'} - \tilde{v}_i \tilde{v}_j \rho' \right]}_{(b)} \quad (2.29)$$

Terms in (b) are clearly non-radiating (each of them is of the form \bar{q}) and can be taken out of the source. This leaves the source term (a), which is identical to f_{1i} . Thus, Goldstein's sources contain extra propagation terms, which when removed, reduce the sources to those derived in section 2.1.2.

2.1.4 Physical interpretation for the propagation operator

The terms within the square brackets on the left hand side of (2.23-2.25) can be interpreted as follows. Each non-radiating term, e.g. \tilde{v}_i , can be decomposed into a steady mean part v_{i0} and an unsteady part v_{ih} , which represents hydrodynamic components. Assuming that $v'_i \ll v_{ih} \ll v_{i0}$, the leading order term in $\tilde{v}_i \tilde{v}_j \rho'$ is $v_{i0} v_{j0} \rho'$. The term $v_{i0} v_{j0} \rho'$ has the same frequency content as ρ' . However, if the steady flow variables v_{i0} and v_{j0} are non uniform, the wavenumber content can be slightly different: although ρ' is purely radiating, $v_{i0} v_{j0} \rho'$ will contain some non-radiating components. Assuming that these are negligible, one can write

$$(\tilde{v}_i \tilde{v}_j \rho')' \approx (v_{i0} v_{j0} \rho')' \approx v_{i0} v_{j0} \rho'. \quad (2.30)$$

Following such an approximation, the interactions between radiating and non-radiating components are reduced to interactions between radiating components and the steady mean flow; equations (2.23-2.25) become inhomogeneous Euler equations linearized about a steady base flow. A similar approximation of the propagation operator will be used to validate the NRBF sources in chapter 4.

2.2 Sources based on a time-averaged base flow (TABF)

2.2.1 Flow decomposition

To derive the TABF sources, every flow variable q is decomposed as

$$q = q_0 + q'' \quad (2.31)$$

where q_0 and q'' denote respectively the steady (time-averaged) and unsteady parts of q .

2.2.2 Source definition

Because taking the time average is a linear operation, following the procedure of section 2.1.2 leads to

$$\frac{\partial \rho''}{\partial t} + \frac{\partial}{\partial x_j} (\rho v_j)'' = 0, \quad (2.32)$$

$$\frac{\partial}{\partial t} (\rho v_i)'' + \frac{\partial}{\partial x_j} (\rho v_i v_j)'' + \frac{\partial (\pi^\gamma)''}{\partial x_i} = 0, \quad (2.33)$$

$$\frac{\partial \pi''}{\partial t} + \frac{\partial}{\partial x_j} (\pi v_j)'' = 0. \quad (2.34)$$

The term $\rho v_i v_j$ can be decomposed as

$$\rho v_i v_j = \begin{cases} (a) & \rho_0 \widehat{v}_i \widehat{v}_j + \\ (b) & \widehat{v}_j (\rho v_i)'' + \widehat{v}_i (\rho v_j)'' - \widehat{v}_i \widehat{v}_j \rho'' + \\ (c) & \frac{1}{\rho_0} (\rho v_i)'' (\rho v_j)'' - \frac{\widehat{v}_j}{\rho_0} (\rho v_i)'' \rho'' - \frac{\widehat{v}_i}{\rho_0} (\rho v_j)'' \rho'' + \frac{\widehat{v}_i \widehat{v}_j}{\rho_0} \rho''^2 + O(\rho''^3), \end{cases} \quad (2.35)$$

where the hats denotes Favre-averaged quantities defined as

$$\widehat{v}_i = \frac{(\rho v_i)_0}{\rho_0}. \quad (2.36)$$

They are analogous to the tilde notation, i.e. \tilde{v}_i , but use a time averaged base flow rather than a non-radiating base flow. The terms (a) to (c) in (2.35) behave as follows:

- (a) is steady, i.e. $(a)'' = 0$,
- (b) is purely unsteady, i.e. $(b)'' = (b)$, and corresponds to interactions between the mean flow and the unsteady flow,
- (c) is non-linear in unsteady variables and contains the sources.

The term $(\pi^\gamma)''$ is decomposed as

$$\pi^\gamma = (\pi_0 + \pi'')^\gamma = \pi_0^\gamma + \gamma \pi_0^{\gamma-1} \pi'' + \frac{1}{2} \gamma(\gamma-1) \pi_0^{\gamma-2} \pi''^2 + O(\pi''^3) \quad (2.37)$$

$$(\pi^\gamma)'' \approx \gamma \pi_0^{\gamma-1} \pi'' + \frac{1}{2} \gamma(\gamma-1) \pi_0^{\gamma-2} (\pi''^2)''. \quad (2.38)$$

Finally, the term πv_j is decomposed as follows:

$$\pi v_j = \begin{cases} (a) & \frac{\pi_0}{\rho_0} (\rho v_j)_0 + \\ (b) & \frac{\pi_0}{\rho_0} (\rho v_j)'' + \hat{v}_j \pi'' - \frac{\pi_0}{\rho_0} \hat{v}_j \rho'' + \\ (c) & \frac{1}{\rho_0} \pi'' (\rho v_j)'' - \frac{\hat{v}_j}{\rho_0} \rho'' \pi'' - \frac{\pi_0}{\rho_0^2} \rho'' (\rho v_j)'' + \frac{\pi_0 \hat{v}_j}{\rho_0^2} \rho''^2 + O(\rho''^3), \end{cases} \quad (2.39)$$

where (a) has no unsteady part, (b) corresponds to interaction terms and (c) to source terms. However, (c) can be expressed as

$$\frac{1}{\rho_0} \left(\pi'' - \frac{\pi_0}{\rho_0} \rho'' \right) ((\rho v_j)'' - \rho'' \hat{v}_j). \quad (2.40)$$

Using the hypothesis of homentropy, i.e. $p = \alpha \rho^\gamma$, it can be shown that

$$\pi'' = \alpha^{1/\gamma} \rho'', \quad (2.41)$$

where $\alpha = (\pi_0 / \rho_0)^\gamma$, so (c) is equal to zero.

One can now rewrite equations (2.32–2.34) by pushing the sound sources to the right hand side and leaving the propagation terms on the left hand side:

$$\frac{\partial \rho''}{\partial t} + \frac{\partial}{\partial x_j} (\rho v_j)'' = 0, \quad (2.42)$$

$$\frac{\partial}{\partial t} (\rho v_i)'' + \frac{\partial}{\partial x_j} (\hat{v}_j (\rho v_i)'' + \hat{v}_i (\rho v_j)'' - \hat{v}_i \hat{v}_j \rho'') + \gamma \frac{\partial}{\partial x_i} \pi_0^{\gamma-1} \pi'' = f_{2i}, \quad (2.43)$$

$$\frac{\partial \pi''}{\partial t} + \frac{\partial}{\partial x_j} \left(\frac{\pi_0}{\rho_0} (\rho v_j)'' + \hat{v}_j \pi'' - \frac{\pi_0}{\rho_0} \hat{v}_j \rho'' \right) = 0, \quad (2.44)$$

where the momentum equation source term f_{2i} is defined as

$$f_{2i} \equiv -\frac{\partial}{\partial x_j} \left(\frac{1}{\rho_0} (\rho v_i)'' (\rho v_j)'' - \frac{\hat{v}_j}{\rho_0} (\rho v_i)'' \rho'' - \frac{\hat{v}_i}{\rho_0} (\rho v_j)'' \rho'' + \frac{\hat{v}_i \hat{v}_j}{\rho_0} \rho''^2 \right)'' - \frac{1}{2} \gamma(\gamma-1) \frac{\partial}{\partial x_i} (\pi_0^{\gamma-2} (\pi'')^2)'' \quad (2.45)$$

2.2.3 Comparison with expressions from the literature

The expression of the TABF sources is analogous to earlier contributions by Bogey *et al.* [10] and Goldstein [40]. Goldstein's expression for the TABF sources is given by

$$f_{2gi} = -\frac{\partial}{\partial x_j} (\rho v_i'' v_j'')'' \approx -\frac{\partial}{\partial x_j} (\rho_0 v_i'' v_j'')'', \quad (2.46)$$

where the third order terms have been neglected and where the unsteady velocity components are defined as

$$v_i'' = v_i - \hat{v}_i. \quad (2.47)$$

In the above section, the momentum density variable ρv_i has been used instead of the velocity variable v_i . The fluctuating variable v_i'' can be expressed in terms of ρ_0 , \hat{v}_i , ρ' and $(\rho v_i)''$ as follows. From

$$\rho v_i = (\rho v_i)_0 + (\rho v_i)'', \quad (2.48)$$

$$v_i = \frac{(\rho v_i)_0}{\rho} + \frac{(\rho v_i)''}{\rho}, \quad (2.49)$$

$$= \hat{v}_i + \frac{1}{\rho_0} (\rho v_i)'' - \frac{\rho''}{\rho_0} \hat{v}_i + O(\rho'^3), \quad (2.50)$$

one can write

$$v_i'' \approx \frac{1}{\rho_0} (\rho v_i)'' - \frac{\rho''}{\rho_0} \hat{v}_i \quad (2.51)$$

Substituting equation (2.51) into equation (2.46),

$$f_{2gi} \approx f_{2i} + \frac{1}{2} \gamma(\gamma-1) \frac{\partial}{\partial x_i} (\pi_0^{\gamma-2} (\pi'')^2)''. \quad (2.52)$$

Thus, the expression (2.45) defining the TABF sources is similar to Goldstein's expression. The differences are that

- Goldstein's expression is exact whereas (2.45) is second order accurate

- Expression (2.45) includes an additional pressure term.

Note that the second point comes from choosing of the modified pressure π as a dependent variables.

2.3 Sources based on a quiescent base flow (QBF)

In Lighthill's acoustic analogy [1], the base flow is taken to be a quiescent medium, defined by

$$\rho = \rho_\infty, \quad \pi = \pi_\infty, \quad u = v = 0. \quad (2.53)$$

The governing equations and associated sources are given by

$$\frac{\partial}{\partial t}(\rho - \rho_\infty) + \frac{\partial}{\partial x_j}(\rho v_j) = 0, \quad (2.54)$$

$$\frac{\partial}{\partial t}(\rho v_i) + \gamma \pi_\infty^{\gamma-1} \frac{\partial}{\partial x_i}(\pi - \pi_\infty) = f_{3i}, \quad (2.55)$$

$$\frac{\partial}{\partial t}(\pi - \pi_\infty) + \frac{\partial}{\partial x_j} \left(\frac{\pi_\infty}{\rho_\infty} \rho v_j \right) = 0, \quad (2.56)$$

where the momentum equation source term f_{3i} is defined as

$$f_{3i} \equiv -\frac{\partial}{\partial x_j} (\rho_\infty v_i v_j) - \frac{1}{2} \gamma(\gamma-1) \pi_\infty^{\gamma-2} \frac{\partial}{\partial x_i} (\pi - \pi_\infty)^2. \quad (2.57)$$

The above equations have been obtained by substituting q'' with $q - q_\infty$ and q_0 with q_∞ in equations (2.42) to (2.45), for q in $\{\rho, \rho u, \rho v, \pi\}$. Because the modified pressure π is used, an additional source term, which is quadratic in $(\pi - \pi_\infty)$, is necessary compared to the classical expression.

2.4 Conclusion

The sound sources have been derived by using three different flow decompositions. Equations (2.26), (2.45) and (2.57) are the main results of this chapter and defined respectively the NRBF, TABF and QBF sources.

Chapter 3

Non-radiating filters

Contents

3.1	Radiation criterion	22
3.1.1	Radiating components in a 3D flow field	22
3.1.2	Radiating components in a 2D flow field	24
3.2	Definitions	24
3.2.1	Non-radiating filter	24
3.2.2	Optimal non-radiating filter	26
3.3	Differential filter	26
3.4	Convolution filters	27
3.4.1	Theory	27
3.4.2	Numerical issues	28
3.4.3	Filtering strategies	32
3.5	Filtering of a two-dimensional shear layer	34
3.5.1	Problem description and implementation	34
3.5.2	Differential filter	35
3.5.3	Convolution filters	35
3.5.4	High pass filter with Hann window	39
3.6	Summary	41

In chapter 2 it was shown how the NRBF sources are expressed in terms of the non-radiating part of the flow field. The non-radiating part of the flow field can be computed by using an optimal non-radiating filter. The present chapter explains how such filters can be designed and implemented.

3.1 Radiation criterion

When dealing with sound radiation, it is convenient to describe a flow in terms of its wavenumber and frequency content. It turns out that there is a

simple relationship between wavenumber and frequency for acoustically radiating components in an unbounded flow-field surrounded by a quiescent medium: the radiating components are those that satisfy the dispersion relation $|\mathbf{k}| = |\omega|/c_\infty$, where \mathbf{k} denotes the wavenumber, ω the angular frequency and c_∞ the ambient speed of sound. The proof by Crighton [11], for three-dimensional flows, constitutes the foundation of this work. It is reproduced below and is extended to two-dimensional flows.

3.1.1 Radiating components in a three-dimensional flow-field

Consider a sound radiating flow-field, surrounded by a quiescent medium. The flow satisfies the Navier-Stokes equations and the radiated sound in the far field can be obtained by using an acoustic analogy. The pressure p satisfies an equation of the form

$$\nabla^2 p(\mathbf{x}, t) - \frac{1}{c_\infty^2} \frac{\partial^2 p(\mathbf{x}, t)}{\partial t^2} = s(\mathbf{x}, t), \quad (3.1)$$

where s is a function of the flow variables (Morfey and Wright [41]).

Taking the Fourier transform in time of equation (3.1) gives, for any $\omega \neq 0$,

$$\nabla^2 p(\mathbf{x}, \omega) + k_\infty^2 p(\mathbf{x}, \omega) = s(\mathbf{x}, \omega), \quad (3.2)$$

where $k_\infty = \omega/c_\infty$ and the Fourier transform is defined as

$$p(\mathbf{x}, \omega) = \int_{-\infty}^{+\infty} p(\mathbf{x}, t) e^{i\omega t} dt. \quad (3.3)$$

Equation (3.2) can be solved by using a free-field Green's function [42]:

$$p(\mathbf{x}, \omega) = \int_{\mathcal{V}} s(\mathbf{y}, \omega) g(\mathbf{x}|\mathbf{y}) d\mathbf{y}, \quad (3.4)$$

where \mathcal{V} is the bounded volume over which s is non-zero and

$$g(\mathbf{x}|\mathbf{y}) = -\frac{e^{ik_\infty|\mathbf{x}-\mathbf{y}|}}{4\pi|\mathbf{x}-\mathbf{y}|}. \quad (3.5)$$

In the far field, $|\mathbf{y}| \ll |\mathbf{x}|$, and the Fraunhofer approximation [43] leads to

$$p(\mathbf{x}, \omega) \underset{|\mathbf{x}| \rightarrow \infty}{\sim} -\frac{e^{ik_\infty|\mathbf{x}|}}{4\pi|\mathbf{x}|} \int_{\mathcal{V}} s(\mathbf{y}, \omega) e^{-ik_\infty \frac{\mathbf{x} \cdot \mathbf{y}}{|\mathbf{x}|}} d\mathbf{y}, \quad (3.6)$$

$$p(\mathbf{x}, \omega) \underset{|\mathbf{x}| \rightarrow \infty}{\sim} -\frac{e^{ik_\infty|\mathbf{x}|}}{4\pi|\mathbf{x}|} S(\mathbf{k}_\infty, \omega), \quad (3.7)$$

where $\mathbf{k}_\infty = k_\infty \mathbf{x} / |\mathbf{x}|$ and S denotes the space–time Fourier transform of the source, which is defined as

$$S(\mathbf{k}, \omega) = \int_V s(\mathbf{y}, \omega) e^{-i\mathbf{k}\cdot\mathbf{y}} d\mathbf{y}. \quad (3.8)$$

Equation (3.7) shows that, for any position \mathbf{x} in the far field and any non-zero frequency ω , the amplitude of the acoustic pressure is proportional to the amplitude of the source at frequency ω and wavenumber $(\omega/c_\infty)\mathbf{x}/|\mathbf{x}|$. The magnitude of such wavenumber is $|\mathbf{k}| = |\omega|/c_\infty$. The only source components that can generate acoustic waves are hence those that satisfy the dispersion relationship $|\mathbf{k}| = |\omega|/c_\infty$. They are called acoustically matched components, or radiating components. A flow field devoid of such components is silent.

As illustrated in figure 3.1, for a given frequency $\omega \neq 0$, the radiating components lie on a sphere of radius $|\mathbf{k}_\infty| = |\omega|/c_\infty$ in the wavenumber domain (k_x, k_y, k_z) . If the radiating sound contains a number of discrete frequencies $\omega_0 < \omega_1 < \dots < \omega_n$, then the radiating components will lie on the radiating spheres corresponding to each of these frequencies in the wavenumber domain.

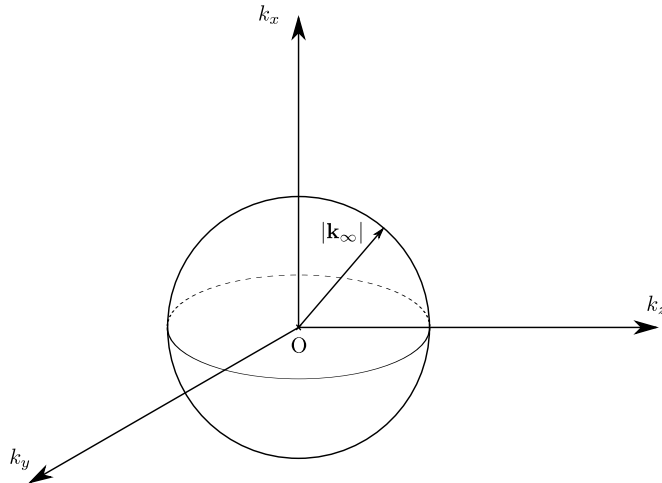


Figure 3.1 – For a three dimensional flow field surrounded by a quiescent medium of sound speed c_∞ , for each frequency ω , the radiating components lie on the sphere defined by $|\mathbf{k}| = |\omega|/c_\infty$ in the wavenumber domain.

3.1.2 Radiating components in a two-dimensional flow-field

The above proof can be readily extended to two-dimensional flow-fields surrounded by a quiescent medium. In such flows, the radiating pressure is

given by

$$p(\mathbf{x}, \omega) = \int_{\mathcal{S}} s(\mathbf{y}, \omega) g(\mathbf{x}|\mathbf{y}) d\mathbf{y}, \quad (3.9)$$

where \mathcal{S} is the bounded part of the flow over which source s is non-zero, and where

$$g(\mathbf{x}|\mathbf{y}) = \frac{i}{4} H_0^{(1)}(k_\infty |\mathbf{x} - \mathbf{y}|), \quad (3.10)$$

where $H_0^{(1)}$ denotes the Hankel function of the first kind of order 0. As shown for example in [44], an asymptotic form of $H_0^{(1)}$ for large arguments is given by

$$H_0^{(1)}(x) \underset{|\mathbf{x}| \rightarrow \infty}{=} \frac{1-i}{\sqrt{\pi x}} e^{ix}. \quad (3.11)$$

From (3.11) and (3.10), for \mathbf{x} in the far field and y in the bounded source region,

$$g(\mathbf{x}|\mathbf{y}) \underset{|\mathbf{x}| \rightarrow \infty}{=} \frac{(1+i)e^{ik_\infty |\mathbf{x}-\mathbf{y}|}}{4\sqrt{\pi|\mathbf{x}|}}, \quad (3.12)$$

The same arguments as in section 3.1.1 lead to a far field solution of the form

$$p(\mathbf{x}, \omega) \underset{|\mathbf{x}| \rightarrow \infty}{=} \frac{(1+i)e^{ik_\infty |\mathbf{x}|}}{4\sqrt{\pi|\mathbf{x}|}} S(\mathbf{k}_\infty, \omega), \quad (3.13)$$

which shows that, in a two-dimensional flow-field surrounded by a quiescent medium, radiating components satisfy the dispersion relation $|\mathbf{k}| = |\omega|/c_\infty$. As illustrated in figure 3.2, for a given frequency ω , the radiating components lie on the circle defined by $|\mathbf{k}| = |\omega|/c_\infty$ in the wavenumber domain (k_x, k_y) .

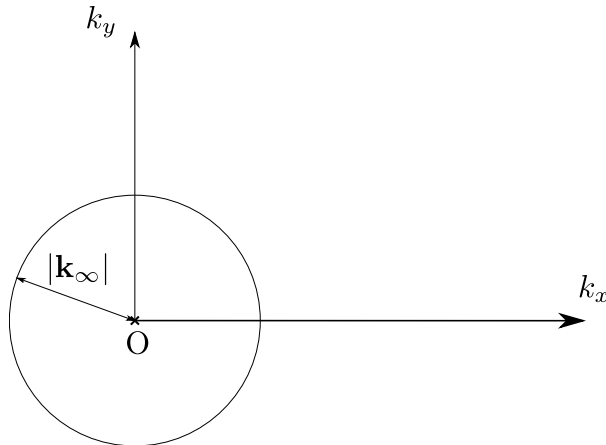


Figure 3.2 – For a two dimensional flow field surrounded by a quiescent medium of sound speed c_∞ , for each frequency ω , the radiating components lie on the circle of radius $|\mathbf{k}_\infty| = |\omega|/c_\infty$ in the wavenumber domain.

3.2 Definitions

3.2.1 Non-radiating filter

Definition Let \mathcal{L} be a filter, q a flow variable and $\bar{q} = \mathcal{L}q$ the corresponding filtered variable. The flow is assumed to be surrounded by a quiescent medium of sound speed c_∞ . \mathcal{L} is a non-radiating filter if and only if

$$\overline{Q}(\mathbf{k}, \omega) = 0 \quad \text{for all } (\mathbf{k}, \omega) \text{ such that } |\mathbf{k}| = |\omega|/c_\infty, \quad (3.14)$$

where $\omega \neq 0$ and \overline{Q} is the space–time Fourier transform of \bar{q} defined as

$$\overline{Q}(\mathbf{k}, \omega) \equiv \int_{-\infty}^{+\infty} \int_{\mathcal{V}} \bar{q}(\mathbf{x}, t) e^{i(\omega t - \mathbf{k} \cdot \mathbf{x})} d\mathbf{x} dt. \quad (3.15)$$

The associated inverse Fourier transform is defined as

$$\bar{q}(\mathbf{x}, t) = \frac{1}{(2\pi)^4} \int_{-\infty}^{+\infty} \int_{\mathcal{V}} \overline{Q}(\mathbf{k}, \omega) e^{-i(\omega t - \mathbf{k} \cdot \mathbf{x})} d\mathbf{k} d\omega. \quad (3.16)$$

Property Let \mathcal{L} be a linear non-radiating filter which commutes with partial derivatives in space and time. Applying \mathcal{L} to a flow field surrounded by a quiescent medium renders the flow non-radiating.

The proof is as follows. Applying \mathcal{L} to the second order wave equation (3.1) gives,

$$\left\{ \nabla^2 - \frac{1}{c_\infty^2} \frac{\partial^2}{\partial t^2} \right\} \bar{p} = \bar{s}, \quad (3.17)$$

where \bar{p} and \bar{s} are respectively the filtered pressure and the filtered source. Substituting p and S with \bar{p} and \bar{S} in (3.7), for any frequency $\omega \neq 0$,

$$\lim_{|\mathbf{x}| \rightarrow \infty} \bar{p}(\mathbf{x}, \omega) = - \lim_{|\mathbf{x}| \rightarrow \infty} \frac{e^{ik_\infty |\mathbf{x}|}}{4\pi |\mathbf{x}|} \bar{S}(\mathbf{k}_\infty, \omega) = 0 \quad (3.18)$$

since $\bar{S}(\mathbf{k}_\infty, \omega) = 0$ from (3.14), so the filtered pressure is non-radiating.

In the far field, the acoustic pressure at any frequency $\omega \neq 0$ is proportional to the other acoustic variables, i.e. velocity \mathbf{v} and density ρ . As the filter is linear, $\bar{\mathbf{v}}$ and $\bar{\rho}$ are also proportional to \bar{p} . Therefore, for any frequency $\omega \neq 0$,

$$\lim_{|\mathbf{x}| \rightarrow \infty} \bar{\mathbf{v}}(\mathbf{x}, \omega) = 0, \quad \lim_{|\mathbf{x}| \rightarrow \infty} \bar{\rho}(\mathbf{x}, \omega) = 0, \quad (3.19)$$

which shows that the filtered flow field is non-radiating.

3.2.2 Optimal non-radiating filter

A filter \mathcal{L} is an optimal non-radiating filter if and only if for any flow variable q , $q' = q - \mathcal{L}q$ is such that

$$\overline{Q}(\mathbf{k}, \omega) = 0 \quad \text{if } |\mathbf{k}| = |\omega|/c_\infty \quad (3.20)$$

$$\overline{Q}(\mathbf{k}, \omega) = 1 \quad \text{if } |\mathbf{k}| \neq |\omega|/c_\infty. \quad (3.21)$$

Optimal non-radiating filters are highly desirable: as shown in section 2.1, they lead to an unambiguous expression of the sound sources (the NRBF sources). In contrast, non-radiating filters are insufficient to derive the noise sources, since they can distort the hydrodynamic flow field or leave hydrodynamic components within the fluctuating field. For example, the time average filter is a non-radiating filter but it leads to the TABF sources of section 2.2 which are a priori less physical than the NRBF sources.

3.3 Differential filter

Obtaining an optimal non-radiating filter in the space–time domain is desirable because it could be implemented easily within the explicit time-domain methods used for solving the Navier–Stokes equations. One interesting feature of differential filters is that, unlike convolution filters, they are localised in space and time. One example of a non-radiating filter in the space–time domain is the d’Alembertian operator, defined by

$$\square^2 = \frac{1}{c_\infty^2} \frac{\partial^2}{\partial t^2} - \nabla^2. \quad (3.22)$$

If $\bar{q} = \square^2 q$, then it can be easily shown that

$$\overline{Q}(\mathbf{k}, \omega) = \left(|\mathbf{k}|^2 - \frac{\omega^2}{c_\infty^2} \right) Q(\mathbf{k}, \omega). \quad (3.23)$$

Provided that Q is not singular over the radiating sphere, which holds for a physical flow variable, the above equation proves that \overline{Q} satisfies (3.14): the d’Alembertian filter is a non-radiating filter. It can be used directly in the time domain, using (3.22), or by windowing in the frequency domain, using (3.23). However, comparing (3.23) with (3.21) shows that the d’Alembertian filter is not an optimal non-radiating filter; it distorts the non-radiating components of the flow variable. It should therefore be supplemented with a filter correcting these distortions. Unfortunately it is not clear how such a corrective filter can

be designed in the time domain.

3.4 Convolution filters

Convolution filters can be used to overcome the limitations of the differential filters.

3.4.1 Theory

Convolution filters are non-local; they are of the form $\bar{q} = w * q$, where

$$\bar{q}(\mathbf{x}, t) = \int_{-\infty}^{+\infty} \int_{\mathcal{V}} w(\mathbf{y}, \tau) q(\mathbf{x} - \mathbf{y}, t - \tau) d\mathbf{y} d\tau. \quad (3.24)$$

The behavior of the filter is determined by function w . These filters use information from the entire signal q , which gives more flexibility to extract some desirable features from q . In addition, from the convolution theorem, the Fourier transform of (3.24) is given by

$$\bar{Q}(\mathbf{k}, \omega) = W(\mathbf{k}, \omega) Q(\mathbf{k}, \omega). \quad (3.25)$$

Convolution filters can therefore be conveniently applied as windowing operations in the frequency domain. For signals that involve large sets of data, this is more efficient than using (3.24). The problem is then to define an appropriate filter window W , in the wavenumber–frequency domain, so that the associated filter w in the space time domain is non-radiating. For a non-radiating filter, the filter window $W(\mathbf{k}, \omega)$ should be such that

$$W(\mathbf{k}, \omega) = 0 \quad \text{for} \quad |\mathbf{k}| = |\omega|/c_\infty, \quad (3.26)$$

for any frequency $\omega \neq 0$. For an optimal non-radiating filter, from (3.21), the filter window $W(\mathbf{k}, \omega)$ must be such that

$$W(\mathbf{k}, \omega) = 1 \quad \text{for} \quad |\mathbf{k}| \neq |\omega|/c_\infty, \quad (3.27)$$

Physically, the filter window must be zero over acoustically matched components, i.e. when $|\mathbf{k}| = |\omega|/c_\infty$, and one when $|\mathbf{k}| \neq |\omega|/c_\infty$.

3.4.2 Numerical issues

Spectral leakage

In practice, the Fourier transform of a flow variable is computed over a finite domain (the computational domain). This is equivalent to multiplying the input signal by a rectangular window whose value is one over the computational domain and zero elsewhere. As a result, from the convolution theorem, the computed Fourier transform is equal to the convolution of the Fourier transform of the flow variable with the Fourier transform of the rectangular window. Mathematically, if q denotes the flow variable and q_{cd} its representation in the computational domain, then

$$q_{cd}(t) = g(t)q(t), \quad Q_{cd}(\omega) = G(\omega) * Q(\omega), \quad (3.28)$$

where g denotes the rectangular window. The convolution of every frequency component with G results in a spreading of that frequency component over a much wider range of frequencies. This phenomenon is called spectral leakage. Due to spectral leakage, a radiating component at frequency ω_0 can be leaked into a much wider range of frequencies, thereby overlapping with non-radiating components. Spectral leakage complicates the separation of the radiating components from the non-radiating components.

Another way to look at the origin of spectral leakage is to understand the effect of discretizing the Fourier transform in the spectral domain. This discretization renders the input signal periodic in the time domain: the signal is replicated towards plus and minus infinity. This can introduce implicit discontinuities in the input signal. These discontinuities generate higher and lower frequencies in the Fourier transform. This is illustrated by comparing figure 3.4 with figure 3.3(a-c). Figure 3.4 shows the exact representations of a sine wave in the time and spectral domain. Figure 3.3 shows the same plane wave over the computational domain (a), as well as three consecutive periods of the input signal (b), and the magnitude of the Fourier transform of the input signal (c). Figure 3.3(b) shows that a discontinuity is introduced implicitly at the extremities of the input signal. This explains the leakage of energy from the frequency of the plane wave onto other frequencies.

Two techniques can be used to mitigate spectral leakage. One is to use a smoothly tapered window instead of a rectangular window. The amount of spectral leakage depends on the properties of the tapered window. The tapered window generally has one main lobe plus a number of side lobes in the spectral domain. The lower the side lobes, the smaller the amount of

spectral leakage. In figure 3.3(d-f) a Hann window, defined as

$$h(t) \equiv \frac{1}{2} \left[1 - \cos \left(2\pi \frac{t - t_{min}}{t_{max} - t_{min}} \right) \right], \quad t_{min} \leq t \leq t_{max}, \quad (3.29)$$

is applied to the input signal. Comparing figures 3.3(b) and 3.3(e) shows that the discontinuity has now vanished from the replicated signal in the time domain. One can see from 3.3(f) that the side lobes have a much lower amplitude compared to those in figure 3.3(c). However, the main lobe is wider and has a lower amplitude than when applying a rectangular window, and the input signal is distorted. The second technique that can be used to mitigate spectral leakage is a careful choice of the size of the computational domain. Figure 3.3(g-i) shows that the replicated signal in the computational domain (h) can be made identical to the physical signal of figure 3.4(a) by making use of the periodic nature of the input signal. Therefore, this technique can only be applied to periodic signals.

Spectral resolution

The spectral resolution of the Fourier transform depends on the length or duration of the input signal. If $q(x)$ is a one dimensional signal that is discretized over N samples separated by distance Δx , then the resolution in the spectral domain is given by

$$\Delta k = \frac{2\pi}{N\Delta x}. \quad (3.30)$$

For a given frequency ω , the radiating components are associated with wavenumber $k_{x,r} = \omega/c_\infty$, whereas the non-radiating components are expected to be associated with wavenumber $k_{x,nr} = \omega/u_x$, where u_x is the convection velocity of the large-scale structures in the flow field. To be able to separate non-radiating from radiating components requires that $\Delta k < k_{x,nr} - k_{x,r}$, i.e.

$$\frac{2\pi}{N\Delta x} < \frac{1 - M_c}{M_c} \frac{\omega}{c_\infty}, \quad (3.31)$$

where $M_c = u_x/c_\infty$ is the convection Mach number. Physically, $N\Delta x$ represents the total length of the input signal. The domain size must be sufficiently large to allow the separation of radiating and non-radiating components.

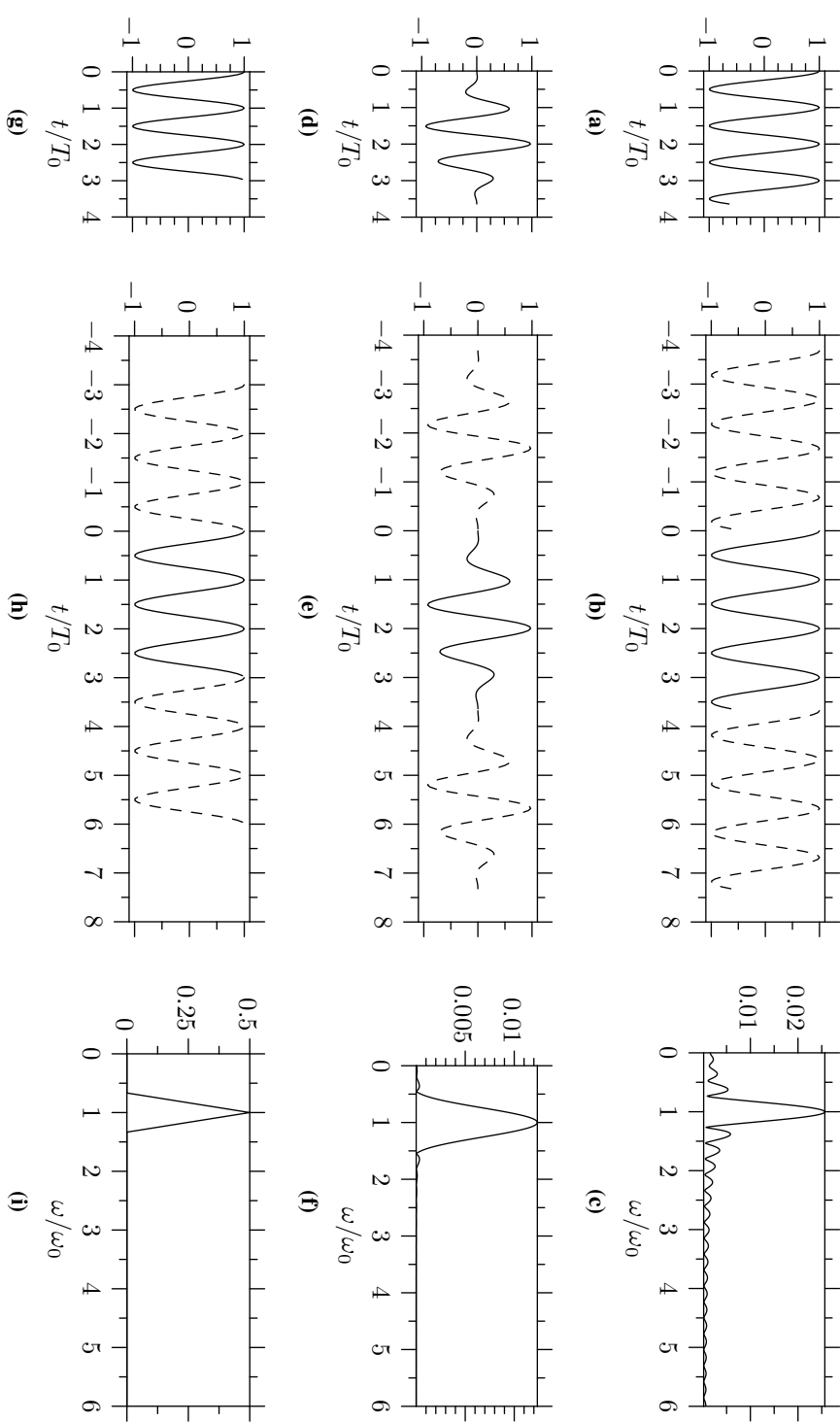


Figure 3.3 – The three rows correspond to three different ways to compute the Fourier transform of a sine wave numerically. The left column shows the input signal. The Fast Fourier transform makes the input signal periodic (second column). The magnitude of the Fourier transform is in column three. In the top row, the signal is multiplied by a rectangular window (a) which leads to high spectral leakage (c). In the middle, the input signal is multiplied by a Hann window (d) which reduces spectral leakage (f). At the bottom, the signal is cropped so that it contains an integer number of periods (g): its discrete representation is periodic (h) and the Fourier transform is exact (h).

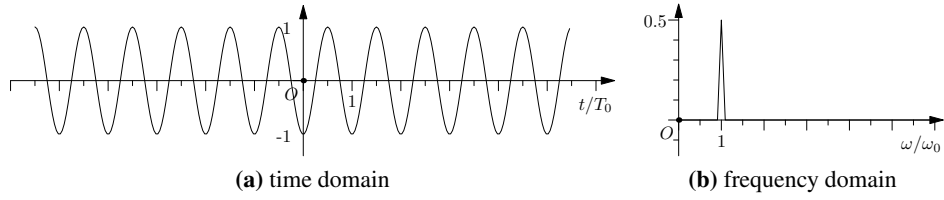


Figure 3.4 – Pure sine wave at frequency ω_0 represented in the time (a) and frequency domain (b) (for $\omega > 0$). In the frequency domain, the signal is a Dirac delta function of magnitude 0.5.

Boundary effects

In one dimension, the discretized version of the convolution product $\bar{q} = w * q$ is

$$\bar{q}_i = \sum_{j=-L}^L w_j q_{i-j}, \quad (3.32)$$

where the filter window is of length $2L + 1$ and the input signal is of length $n \geq 2L + 1$. To compute \bar{q}_i , for $L \leq i < n - L$, the filter window is centered around q_i and the dot product of the two vectors is computed, as illustrated in figure 3.5 for a filter window of length 3. It can be seen that the operation cannot be carried out for the boundary points q_0 and q_1 , because parts of the filter window exits the computational domain.

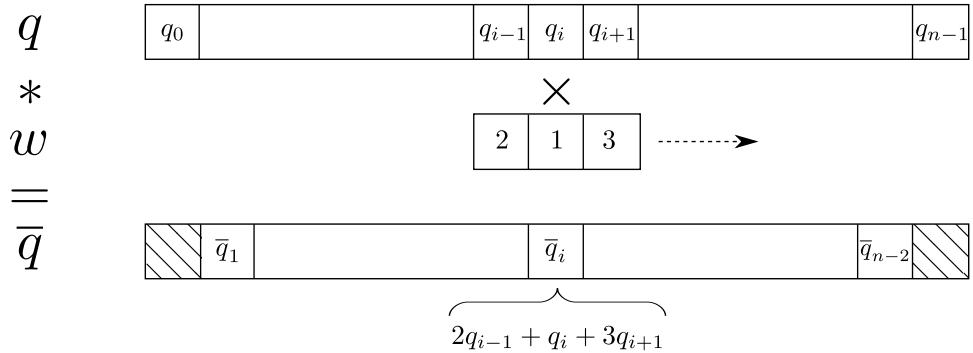


Figure 3.5 – Discretized version of the convolution product $\bar{q} = q * w$ in one dimension for a filter window $w = [2, 1, 3]$. To compute \bar{q}_i for $1 \leq i < n - 1$, the filter window is centered around q_i . The matching values between q and w are multiplied element by element. \bar{q}_i is equal to the sum of these multiplications.

When the convolution is carried out numerically as a product in the spectral domain, the input signal becomes periodic. The boundary values \bar{q}_i , for $0 \leq i < L$ or $n - L \leq i < n$, are computed by wrapping around the input signal. This is illustrated in figure 3.6. This phenomenon can lead to large errors in the computation of boundary values. These boundary effects cannot be suppressed but only mitigated by padding the input signal with more physical

values. In the case of a jet, for example, the flow is expected to be undisturbed upstream and therefore the input signal is padded with zeros: $q_{i-j} = 0$ for $i < j \leq L$ in (3.32). This technique is hence called zero padding. If the filter window is of length $2L + 1$, then the input signal should be padded with at least L zeros.

$$\begin{array}{c}
 q \quad \begin{array}{|c|c|c|}\hline q_{n-1} & q_0 & q_1 & \dots & q_{n-1} & q_0 & \dots \\ \hline\end{array} \\
 * \quad \times \\
 w \quad \begin{array}{|c|c|c|}\hline 2 & 1 & 3 \\ \hline\end{array} \\
 = \\
 \bar{q} \quad \begin{array}{|c|c|c|}\hline \bar{q}_0 & \bar{q}_1 & \dots & \bar{q}_{n-1} \\ \hline\end{array} \\
 \underbrace{\phantom{\bar{q}_0}}_{2q_{n-1} + q_0 + 3q_1}
 \end{array}$$

Figure 3.6 – Discretized version of the convolution product $\bar{q} = q * w$ in one dimension for a filter window $w = [2, 1, 3]$. To compute \bar{q}_i for boundary points ($i = 0$ or 1), the input signal q is wrapped around. This happens implicitly when computing the convolution by using a product of Fourier transforms in the spectral domain.

In this thesis, convolutions will be carried out in the spectral domain and the input signal will be two dimensional. If the computational domain is of size $N \times M$, then the flow variable q will be zero padded so that its Fourier transform will be of size $2N \times 2M$.

Note that boundary effects can also be understood as an aliasing problem in the spectral problem. From the convolution theorem, $w*q$ equals WQ in the spectral domain: this product leads to the appearance of sum and difference frequencies. However, if q and w are of length n , then the Nyquist frequency corresponds to sample $n/2$ in the spectral domain [45]. The peak frequency in WQ therefore corresponds to sample n in the spectral domain, which is superior to the Nyquist frequency. Such high frequency is therefore aliased and appears as a low frequency, unless the length of the signals q and w is first increased to at least $2n$ by using for example zero padding.

3.4.3 Filtering strategies

Filter window design

The first step is to compute and analyze the Fourier transform of the flow variable to be filtered. Two strategies can be used to design the filter window. The first focuses on capturing the radiating components. The second focuses on capturing the non-radiating components. These two techniques are illus-

trated in figure 3.7. The figure shows a two-dimensional flow variable Q at a particular frequency in the wavenumber domain, where the radiating and non-radiating components are well separated. The flow variable is filtered in two different ways. In the first one (a), the filter window W masks the radiating components and focuses on the non-radiating ones. In the second one (b), the filter window captures instead the radiating components. In certain cases one approach is preferable. If the non-radiating components are clearly identified, it might be easier to focus on them since their magnitude is usually much larger than that of the radiating components. When this is not the case, it is easier to focus directly on the radiating component.

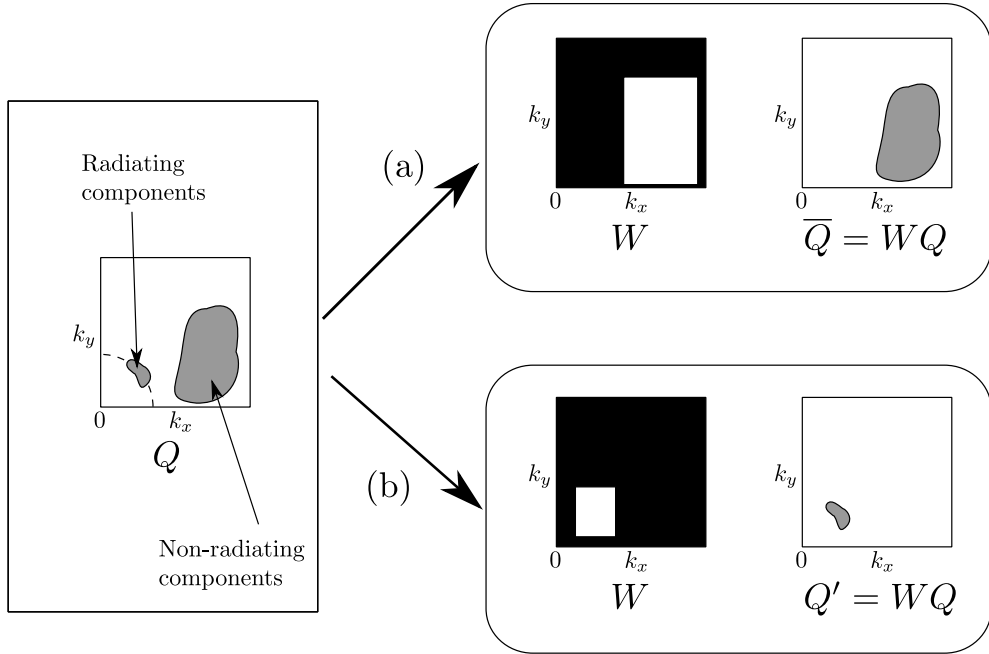


Figure 3.7 – Two possible filtering strategies: (a) focus is on the non-radiating components of the flow, (b) focus is on the radiating components of the flow. In the illustration of the filter window W , black means one and white means zero. Rectangular windows are used in this figure for simplicity. In reality, the filter window would have a smoother shape.

Spatial windowing in the time domain

In certain cases, windowing the flow spatially in the time domain using a tapered window might be needed to obtain a clear separation between radiating and non-radiating components. In such cases, one has to inverse the windowing operation after filtering. Thus, if $h(\mathbf{x})$ denotes the spatial window, then the filtered flow variable \bar{q} would be obtained formally as

$$\bar{q}(\mathbf{x}, t) = h^{-1}(\mathbf{x}) \overline{h(\mathbf{x}) q(\mathbf{x}, t)}, \quad (3.33)$$

where h^{-1} denotes the inverse filter window. However, in general, $h(\mathbf{x})$ becomes small as \mathbf{x} approaches the boundaries of the computational domain, so $h^{-1}(\mathbf{x})$ becomes large close to the boundaries. As a result, $\bar{q}(\mathbf{x}, t)$ can be computed to a reasonable accuracy only when \mathbf{x} is sufficiently far from the boundaries.

3.5 Filtering of a two-dimensional shear layer

3.5.1 Problem description and implementation

The filtering techniques are applied to a benchmark problem (Agarwal, Morris and Mani [37]) of a two-dimensional parallel jet (Mach number = 0.756) that is excited by a time-harmonic spatially-compact gaussian source of frequency $\omega_s = 76\text{rad/s}$ located at the origin. The frequency of excitation is such that it generates both an acoustic wave and a strong instability wave. The solution is obtained by solving the Linearised Euler Equations (LEE) using an explicit finite-difference scheme. Because the problem is linear and the hydrodynamic wave in this problem is represented by a strong instability wave, it is an ideal problem to test the filtering techniques in terms of their ability to separate radiating and non-radiating components.

The total size of the computational domain is $-170 \leq x \leq 600$ and $0 \leq y \leq 150$, with 1380 points along the x-axis and 900 along the y-axis. The grid is uniform in both directions. A symmetric boundary condition is used along $y = 0$ and buffer zones are used on the other sides of the computational domain. The data is post-processed as follows. The symmetric part $y < 0$ is created to avoid boundary effects along $y = 0$. The domain is then cropped to $-76 \leq x \leq 257.5$ and $-50 \leq y \leq 50$. Hereafter, the results are presented only for $-50 \leq x \leq 150$, which is the region used by Agarwal *et al.*[37].

The instantaneous pressure field at time $t_0 = 50T_s$, where $T_s = 2\pi/\omega_s$ is the period of excitation, is plotted in figure 3.8. The figure shows the presence of two kinds of waves radiating from the origin: acoustic waves radiating to the far field, and a hydrodynamic wave growing in the downstream direction along the x -axis.

3.5.2 Differential filter

The d'Alembertian filter of (3.22) is applied at every time step to obtain

$$\bar{p} \equiv \square^2 p. \quad (3.34)$$

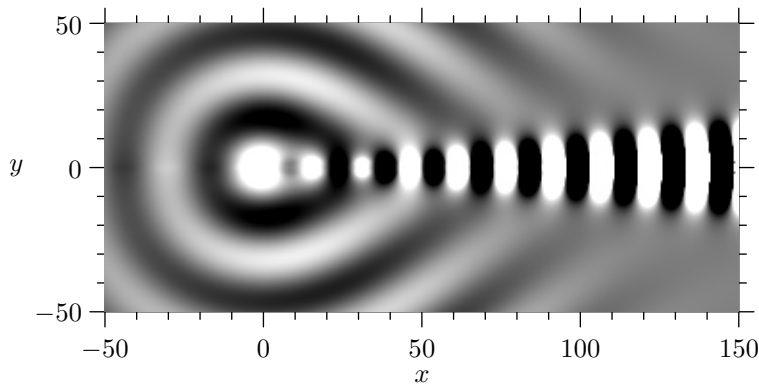


Figure 3.8 – Pressure field $p(x, t_0)$. Linear contour levels are between are between $-2 \cdot 10^{-6}$ (black) and $2 \cdot 10^{-6}$ (white).

The partial derivatives in time are obtained with a second order finite difference scheme, and those in space with a fourth order DRP scheme. The time step used for the partial time derivative is $\Delta t = T_s/20$.

The filtered pressure field is plotted in figure 3.9 at t_0 . To compare \bar{p} with p , which does not have the same physical dimension, \bar{p} has been multiplied by a factor $L^2 = 2.5$. This factor has been computed so as to have $L^2 \cdot \max(\bar{p}) = \max(p)$. Figure 3.9 clearly shows that the d'Alembertian filter renders the pressure field non-radiating: the sound waves present in figure 3.8 have now disappeared from the flow-field. However, the filter changes the structure of the hydrodynamic waves, which is undesirable. This can be explained by observing that (3.27) is not satisfied by the d'Alembertian operator. The filter is not an optimal non-radiating filter and cannot be used, in the present form, to explore the NRBF sources in fluid flows.

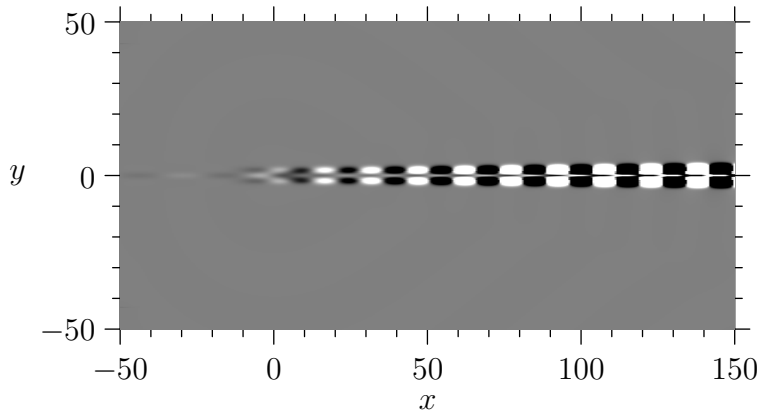


Figure 3.9 – Filtered pressure field $\bar{p} = \square^2 p$ at time t_0 using the d'Alembertian operator. Linear contour levels are between are between $-2 \cdot 10^{-6}$ (black) and $2 \cdot 10^{-6}$ (white).

3.5.3 Convolution filters

Spectral analysis

The instantaneous pressure field of figure 3.8 is Fourier transformed in space to obtain $P(\mathbf{k}, t_0)$. A pseudo colour plot of $|P(\mathbf{k}, t_0)|$ is shown in figures 3.10(a); it can be seen that the instability wave is concentrated around $k_x = \pm k_0$, where $k_0 = 0.41459$. For the present problem, from table 3.1, the radiation circle should be centred at the origin with a radius of 0.219. Figure 3.10(b), in which the range of the colour bar has been reduced from $[0, 10]$ to $[0, 1]$, shows that the radiation circle is overwhelmed by the neighbouring instability wave. This is because a spatial rectangular window is implicitly applied to the time domain pressure field which leads to spectral leakage, as explained in section 3.4.2.

ω_s	c_∞	k_∞
76 rad/s	347.2 m/s	0.219 m^{-1}

Table 3.1 – Flow parameters for the two-dimensional shear layer problem

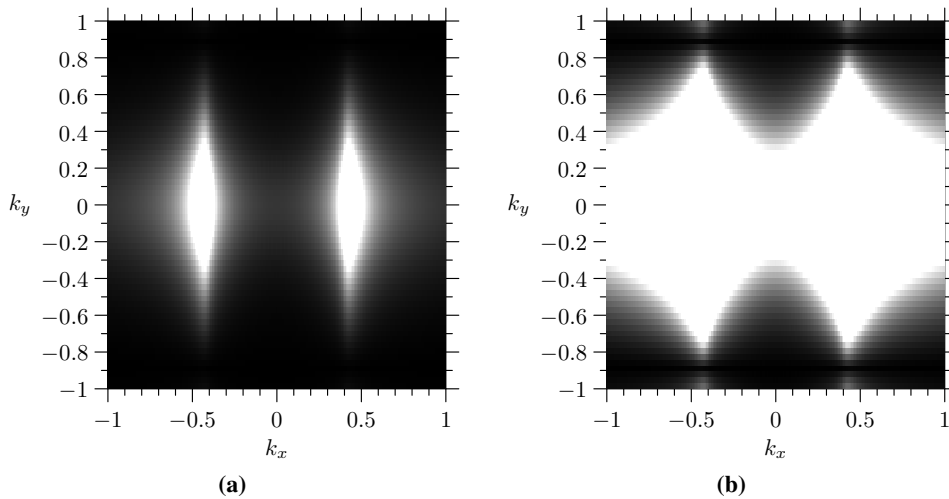


Figure 3.10 – Pressure magnitude $|P(\mathbf{k}, t_0)|$ in the wavenumber domain computed using a rectangular window. Linear contour levels, from black to white, are from 0 to 10 in figures (a), and from 0 to 1 in figure (b). This shows that the radiating circle, defined as $|\mathbf{k}| = 0.219$ is overwhelmed by the non-radiating components.

To reduce spectral leakage, the pressure field is multiplied by a Hann window in the space domain, along the x -axis. The resulting Fourier transform magnitude is shown in figure 3.11. The radiation circle is now clearly visible.

The amount of spectral leakage depends on the properties of the windowing function. A window can be characterised by the width of the main lobe,

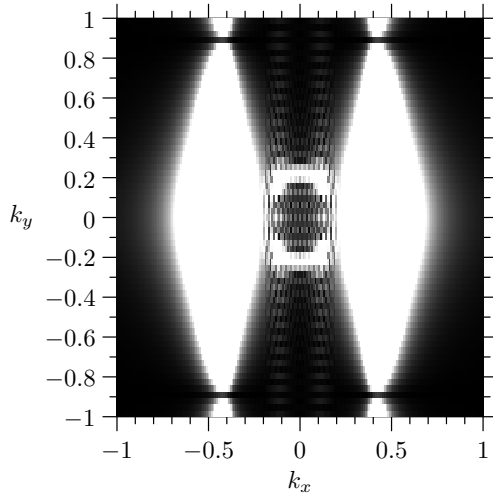


Figure 3.11 – Pressure magnitude $|P(\mathbf{k}, t_0)|$ in the wavenumber domain Fourier computed using a Hann window. Linear contour levels are between 0 (black) and 0.01 (white)

the height of the side lobe and the roll-off rate. The non-zero width of the main lobe smears the flow energy locally. Energy is also leaked further away depending on the height of the side lobe and the roll-off rate. This is illustrated in figure 3.12, in which the properties of a rectangular window are compared to those of a Hann window. The rectangular window has a high side lobe (-13dB) and a slow roll-off (6dB/Octave) which leads to a large amount of spectral leakage (-19dB after one octave). From table 3.1, the main hydrodynamic wavenumber ($k_0 = 0.41459\text{m}^{-1}$) is less than an octave away from the acoustic wavenumbers ($k_\infty = 0.219\text{m}^{-1}$). A leakage of 19dB is hence sufficient to fully contaminate the radiation circle, as shown in figure 3.10(b). On the contrary, a Hann window, has a low side lobe (-32dB) and a fast roll-off (18dB/Octave) which leads to a small amount of spectral leakage (-50dB after one octave). This allows us to uncover the radiation circle, as shown in figure 3.11.

Gaussian filter with rectangular window

As a first attempt, the pressure field is filtered with a rectangular window to avoid distorting the data in the space-time domain. From figure 3.10(b), the radiating components are contaminated by the leakage from the non-radiating ones. The focus is therefore on capturing the main features of the non-radiating components, which corresponds to strategy (a) in figure 3.7. In this problem, the instability wave is concentrated in a band centred around $k_x = \pm k_0$, where $k_0 = 0.41459$, as shown in figure 3.10(a). The filter win-

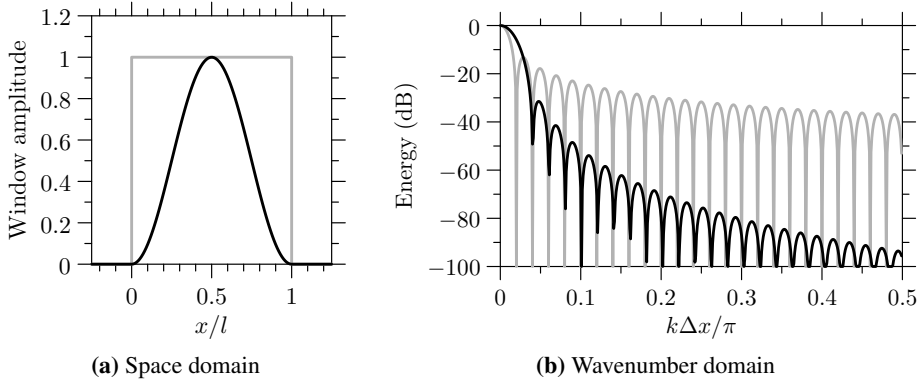


Figure 3.12 – Rectangular window (gray) and Hann window (black) in space and wavenumber domain. In (a), x is normalised by the window length. In (b), only the first half of the wavenumber range is plotted and k is normalised by half the sampling wavenumber.

dow is therefore defined as the sum of two Gaussians centred on k_0 and $-k_0$ respectively, i.e.

$$W(\mathbf{k}) \equiv \exp \left[-\frac{(k_x - k_0)^2}{2\sigma^2} \right] + \exp \left[-\frac{(k_x + k_0)^2}{2\sigma^2} \right], \quad (3.35)$$

where $\sigma = 0.1$. Note that because the source is harmonic, a filter window W that is independent of frequency can be used, which simplifies the filtering operation.

The magnitude of the filtered pressure $\bar{P} = WP$ is plotted in figure 3.13. As shown by comparing with figure 3.10(a), it is in good agreement with the non-radiating components present in $|P(\mathbf{k}, t_0)|$.

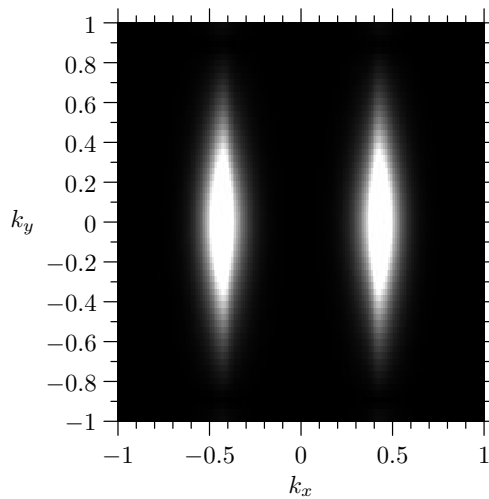


Figure 3.13 – Magnitude of filtered pressure in the wavenumber domain for a gaussian filter, using a rectangular window in the space domain . Linear contour levels are between 0 (black) and 10 (white).

The filtered pressure field \bar{p} is then obtained by taking the inverse Fourier transform in space. For convenience, the result is shown at the end of the chapter in figure 3.16(a). The filtered pressure field is clearly non-radiating and is in very good agreement with the original pressure field of figure 3.8 in the region where the instability wave is dominant. This is confirmed by figure 3.16(b), in which a profile of \bar{p} is compared to an analytical solution of the instability wave along $y = 15$. This analytical solution is from Agarwal et al. [37]. The agreement is very good.

However, the error becomes relatively large compared to the size of the radiating components. This can be seen in figures 3.16(c) and 3.16(d), which present the radiating pressure field $p' = p - \bar{p}$ at time t_0 and a comparison with the analytical solution along $y = 15$.

3.5.4 High pass filter with Hann window

To reduce the error observed on the radiating components when using a rectangular window, a Hann window is applied in the space domain. The windowed pressure $p_h = hp$ is shown in figure 3.14. A high pass filter is used to capture the non-radiating components of the flow. The filter is defined as

$$W(\mathbf{k}) = \frac{1}{2} \left[1 + \tanh \left(\frac{|k_x| - k_{co}}{\sigma} \right) \right], \quad (3.36)$$

where the cut-on wavenumber k_{co} equals 0.23 and where the transition width is controlled by $\sigma = 0.01$. The magnitude of the filtered pressure $\bar{P}_h = WP_h$ in the wavenumber domain is shown in figure 3.15. It is in good agreement with the magnitude of P_h presented in figure 3.11 outside of the radiation circle.

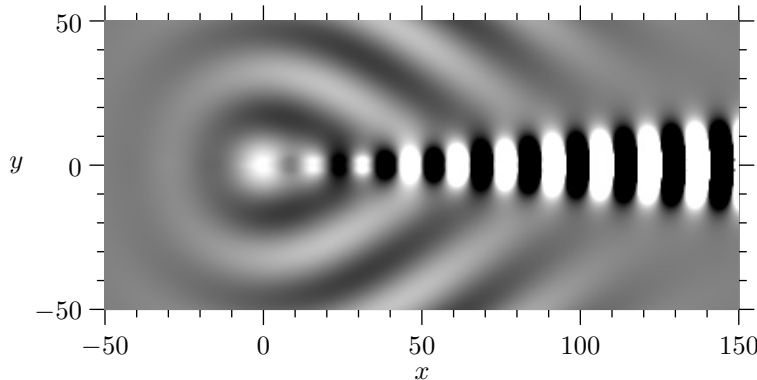


Figure 3.14 – Pressure field $p(\mathbf{x}, t_0)$. Linear contour levels are between $-2 \cdot 10^{-6}$ (black) and $2 \cdot 10^{-6}$ (white).

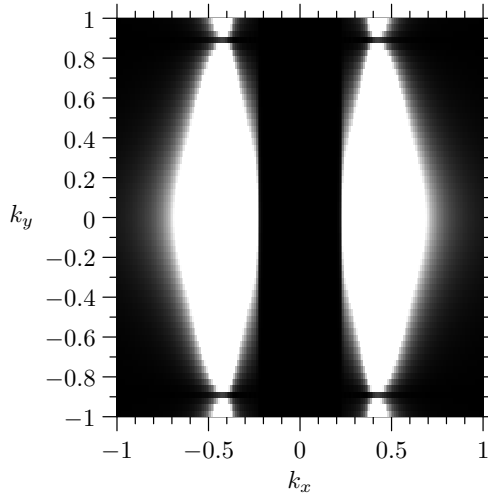


Figure 3.15 – Pressure magnitude $|P(\mathbf{k}, t_0)|$ in the wavenumber domain Fourier computed using a Hann window. Linear contour levels are between 0 (black) and 1 (white)

The corresponding filtered pressure \bar{p}_h and radiating pressure $p'_h = p_h - \bar{p}_h$ are shown in figure 3.17. They are compared with the windowed versions of the analytical solution along $y = 15$. Agreement is excellent for both radiating and non-radiating components.

One drawback of the present approach is that the pressure field is distorted by the Hann window. Signals \bar{p}_h and p'_h must be multiplied by the inverse of the Hann window to correct the distortion. The corrected signals are shown in figure 3.18. The results are satisfactory for $-15 \geq x \leq 150$. Compared to the previous approach using a Gaussian filter (figure 3.16), the error observed on the radiating components for $x \geq 25$ has been reduced.

Hybrid method

As has been shown above, the high pass filter associated with a Hann window performs best for $x \geq 25$, while the Gaussian filter associated with a rectangular window gives good results even for small values of x . It is possible to combine both filters by retaining the results from the best filter in each region. The results are shown in figure 3.19. Agreement with the analytical solution is very good for both \bar{p} and p' .

Conclusion

This numerical study illustrates the flexibility of convolution filters. The filter window can be tailored in the spectral domain to capture the desired flow components. If required, the flow can be windowed in the time domain to reduce spectral leakage.

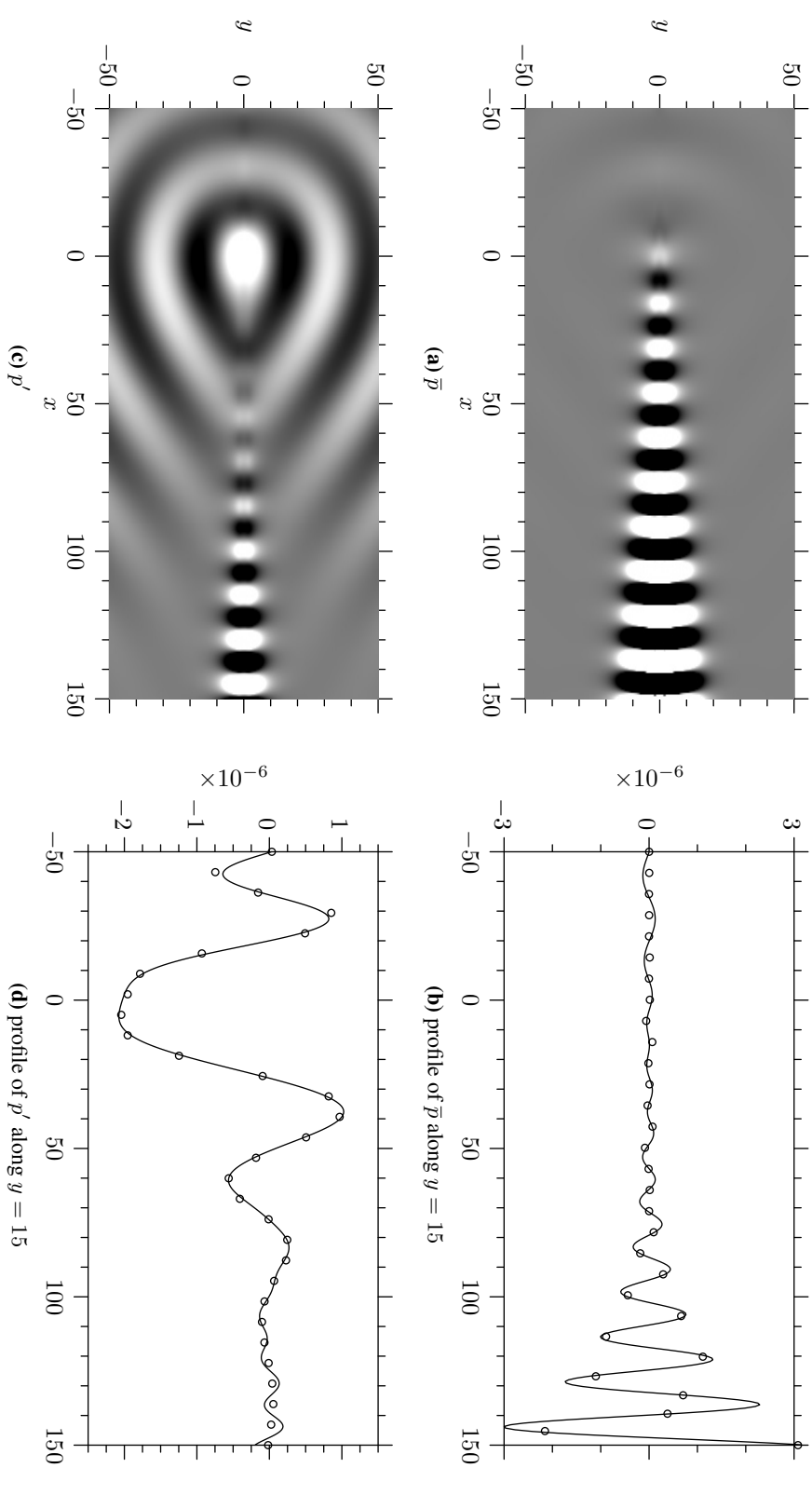


Figure 3.16 – Pressure and filtered pressure using a Gaussian filter. Linear contour levels are between $-2 \cdot 10^{-6}$ (black) and $2 \cdot 10^{-6}$ (white). In (b) and (d), the solid line represents the numerical solution, and the circles the exact analytical solution.

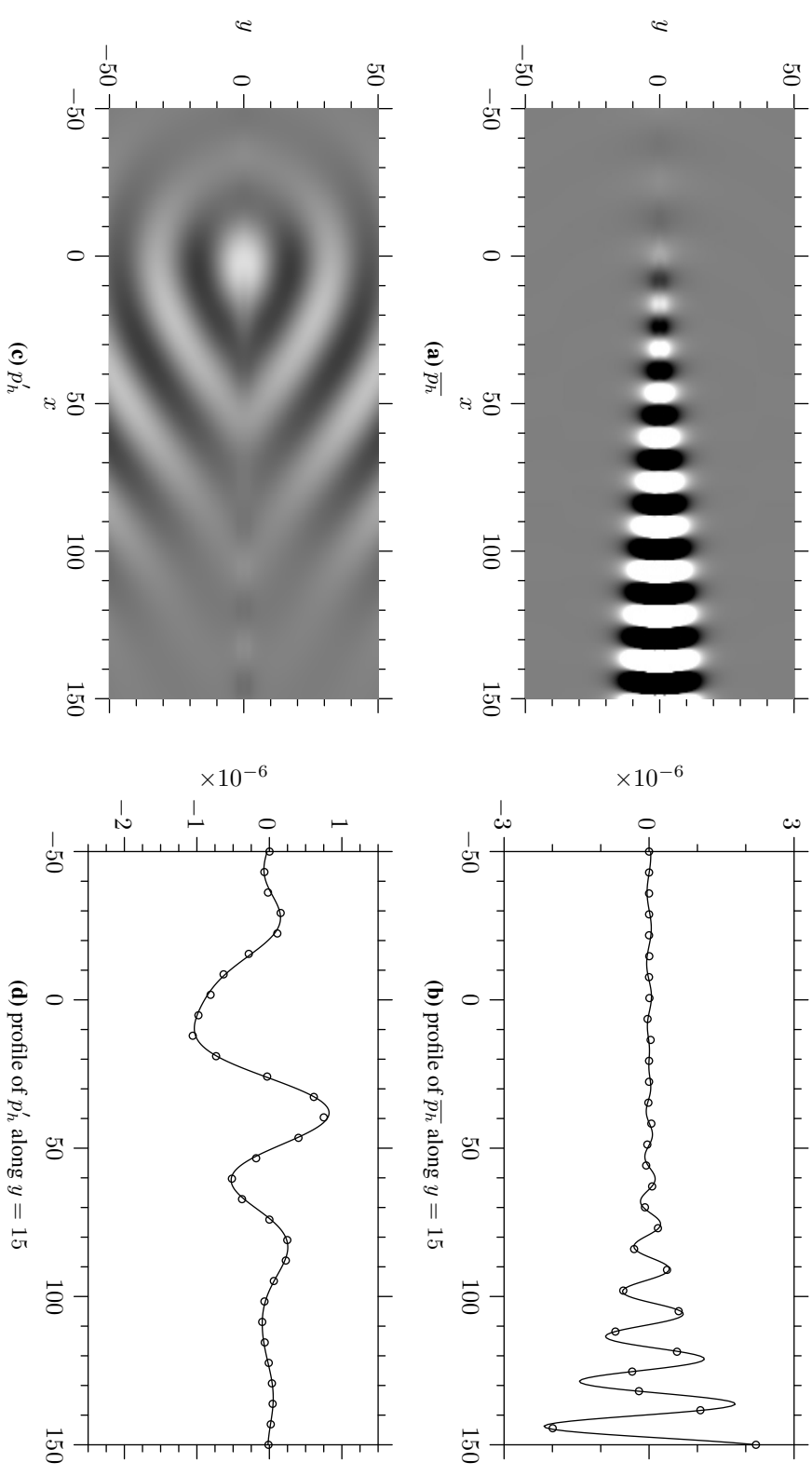


Figure 3.17 – Pressure and filtered pressure \overline{p}_h and \overline{p}' using a high pass filter and a Hann window. Linear contour levels are between $-2 \cdot 10^{-6}$ (black) and $2 \cdot 10^{-6}$ (white). In (b) and (d), the solid line represents the numerical solution, and the circles the exact analytical solution.

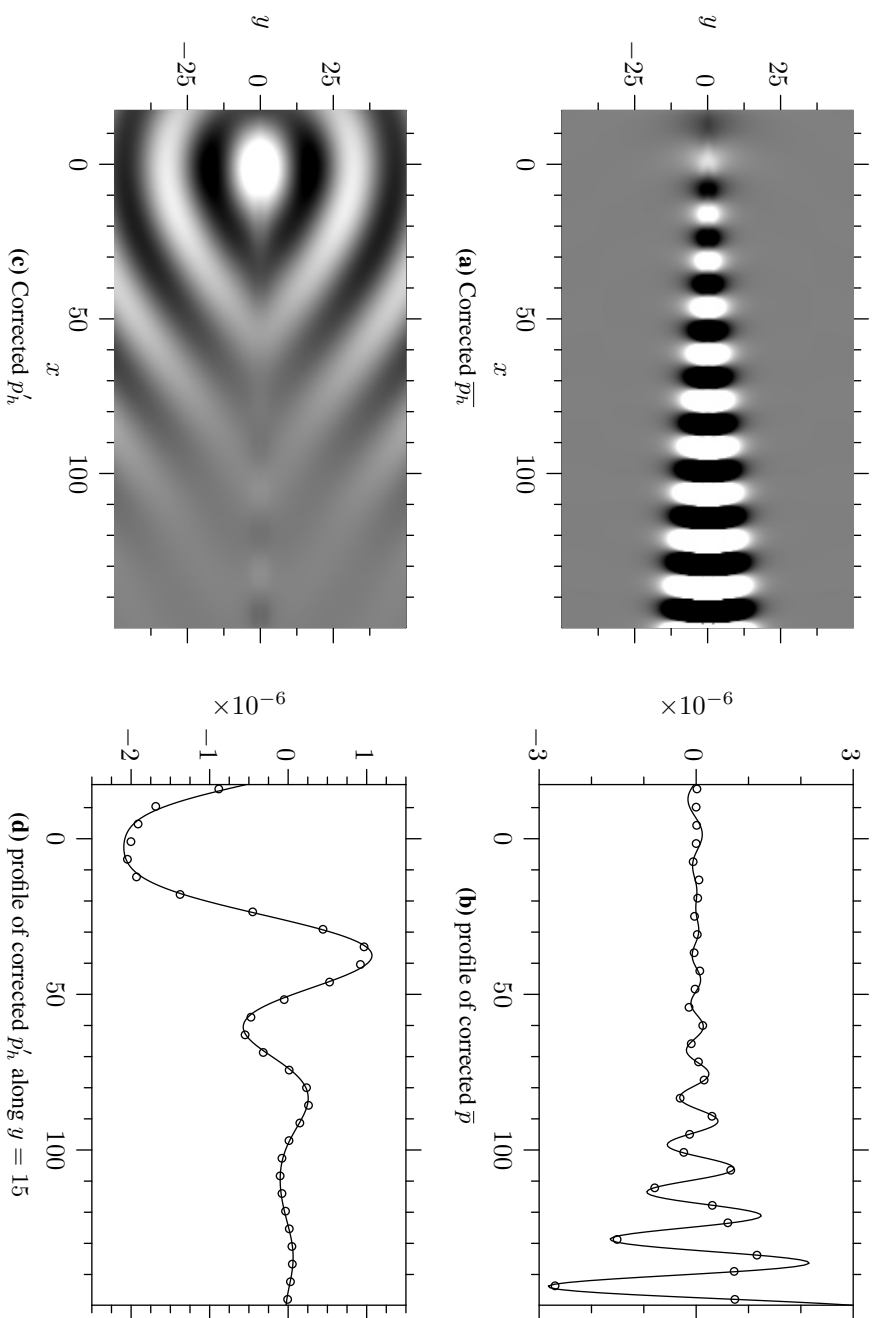


Figure 3.18 – Pressure and filtered pressure using a high pass filter and a Hann window. The distortions introduced by the Hann window are corrected by multiplying \bar{p}_h and p'_h by an inverse window. Linear contour levels are between $-2 \cdot 10^{-6}$ (black) and $2 \cdot 10^{-6}$ (white). In (b) and (d), the solid line represents the numerical solution, and the circles the exact analytical solution.

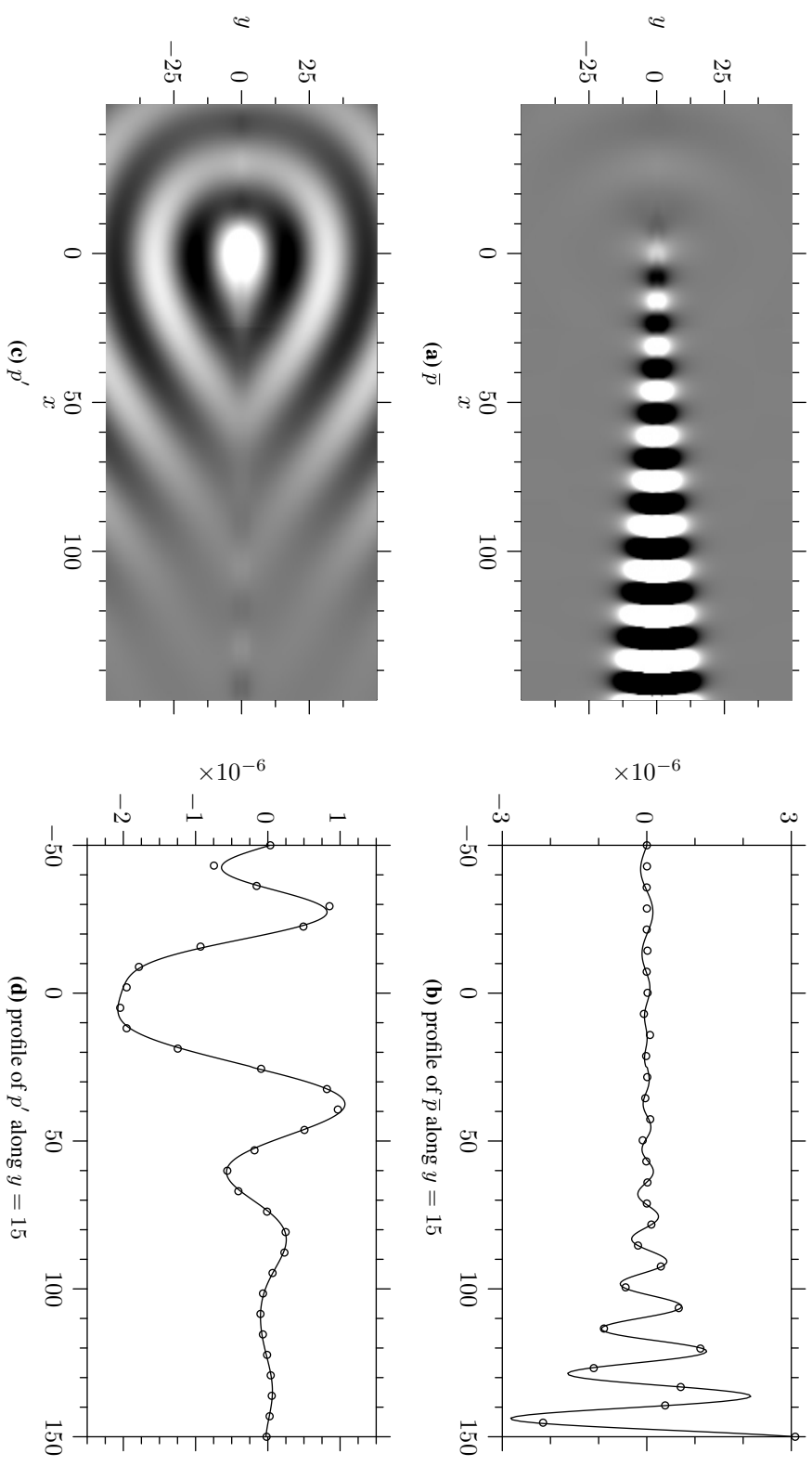


Figure 3.19 – Pressure and filtered pressure using a hybrid filter. The results of employing a Gaussian filter with a rectangular window are used for $x \leq 25$. For $x \geq 25$, the results correspond to a high pass filter associated with a Hann window. Linear contour levels are between $-2 \cdot 10^{-6}$ (black) and $2 \cdot 10^{-6}$ (white). In (b) and (d), the solid line represents the numerical solution, and the circles the exact analytical solution.

3.6 Summary

An unbounded flow surrounded by a quiescent medium can be decomposed into its radiating and non-radiating components using an optimal non-radiating filter. These utilize the fact that radiating components satisfy the dispersion relation $|k| = |\omega|/c_\infty$ in the spectral domain. Two kinds of filters have been investigated: differential filters and convolution filters. No satisfactory differential filter has been found. The d'Alembertian filter is non-radiating but is not optimal.

Convolution filters are more flexible and enable more control in designing the filter. However, they are subject to a number of numerical issues due to the computation of the Fourier transform over a finite domain. These issues include spectral leakage and boundary effects. They can be mitigated by windowing the flow and using zero padding in the time domain. In particular, if the radiating components are at least two orders of magnitude smaller than non-radiating ones, then windowing the flow becomes necessary if the radiating wavenumbers are less than 2 octaves away from the non-radiating wavenumbers. Using convolution filters, it is possible to separate the radiating and non-radiating parts of the pressure field in a two-dimensional shear layer flow satisfying the Linearized Euler Equations.

Chapter 4

Sources of sound in a laminar jet

Contents

4.1	Problem description	48
4.2	Flow analysis	49
4.2.1	Grids	49
4.2.2	Steady flow	49
4.2.3	Unsteady flow	51
4.2.4	Frequency analysis	52
4.2.5	Wavenumber analysis	56
4.3	Flow filtering	58
4.3.1	Algorithm	58
4.3.2	Filter definition	61
4.3.3	Results	61
4.4	NRBF sources	66
4.4.1	Algorithm	66
4.4.2	Results and discussion	67
4.4.3	Amplitude and location of the sound sources	73
4.4.4	Validation	74
4.4.5	Dominant source term	75
4.5	Effect of the size of the computational domain	77
4.5.1	Algorithm	79
4.5.2	Reducing size in the radial direction	80
4.5.3	Reducing size in the axial direction	80
4.5.4	Reducing size in both directions	82
4.6	Source based on a time averaged base flow	82
4.6.1	Algorithm	84
4.6.2	Results	85
4.6.3	Discussion	86
4.7	Source based on a quiescent base flow	90

4.7.1	Algorithm	90
4.7.2	Results and discussion	91
4.8	Conclusion	96

In this chapter, sound sources are computed for an axisymmetric laminar jet. Different expressions are used. Each expression depends on the choice of base flow. These sources are computed based on a non-radiating base flow (NRBF), a time averaged flow (TABF) and a quiescent base flow (QBF), using the expressions derived in chapter 2. The NRBF sources rely on a silent base flow that is computed by using the optimal non-radiating filters described in chapter 3.

4.1 Problem description

The flow is simulated by a DNS of a fixed axisymmetric mean flow excited at the inflow by two frequencies. The frequencies are chosen to trigger some instability waves in the flow. These instability waves grow downstream and interact non-linearly, thereby generating acoustic waves.

The main flow characteristics are as follows. The Mach number is 0.9 and the Reynolds number is 3600. The base mean flow is chosen to match the experimental data of Stromberg *et al.* [23]. The mean flow is axisymmetric and the radial and azimuthal components of the mean velocities are set to zero. The excitation modes at the two unstable frequencies are also axisymmetric. The jet static temperature is identical to the far field temperature (cold jet): sound generation due to entropy fluctuations are likely to be negligible so the theory of chapter 2, which assumes that the flow is homentropic, will be used.

This case corresponds to one of the several Navier–Stokes solutions obtained by Suponitsky *et al.* [46], who ran simulations with different combinations of excitation frequencies and amplitudes. The data used here corresponds to the case with the largest acoustic radiation. The two excitation frequencies are $\omega_1 = 2.2$ and $\omega_2 = 3.4$. The results presented in this section have been normalized by using the jet diameter D , jet exit speed U_j and the ambient density as the length, velocity and density scales, respectively.

4.2 Flow analysis

4.2.1 Grids

Variable z describes the position along jet axis, and r is the position in the radial direction. The full computational domain extends for $0 \leq z \leq 50.3$ in

the axial direction and $-15 \leq r \leq 46.6$ in the radial direction. The negative r values are due to the use of a cartesian grid; the axisymmetric nature of the jet derives from the axisymmetric nature of the excitation. The grid has 1100 points in the z -direction and 451 in the r -direction. Its spacing is shown in figure 4.1. The radial spacing Δr is eight times smaller within the jet and close to the shear layer ($\Delta r \approx 0.026$ for $-2 \leq r \leq 2$) than away from it ($\Delta r \approx 0.211$ for $|r| \geq 5$). The grid is equally spaced in the z -direction ($\Delta z \approx 0.049$).

In order to use convolution filters, the data must be interpolated on a grid that lends itself to computing the Fourier transform of the data. For an axisymmetric flow, a Hankel transform must be used in the radial direction and a Fourier transform in the axial direction (c.f. appendix A). The grid associated with a Hankel transform of order 0 is defined as [47]

$$r_n = \frac{\alpha_n}{\alpha_{N+1}} R, \quad 0 \leq n < N, \quad (4.1)$$

where N is the number of grid points, α_n denotes the n^{th} zero of the Bessel function of the first kind of order 0 (denoted J_0) and R is the maximum value of the grid. The zeros of J_0 [48] are approximately equally spaced (the mean spacing of the first 100 zeros of J_0 is approximately 3.141 with standard deviation 0.003), so the Hankel grid is nearly uniform: the number of points must be increased compared to the initial grid to maintain sufficient resolution within the shear layer. To reduce the computational requirements the computational domain is restricted to $0 \leq z \leq 43.1$ and $0.02 \leq r \leq 27$, with $N = 1040$. From figure 4.1, it can be seen that $\Delta r \approx 0.260$ for the Hankel grid.

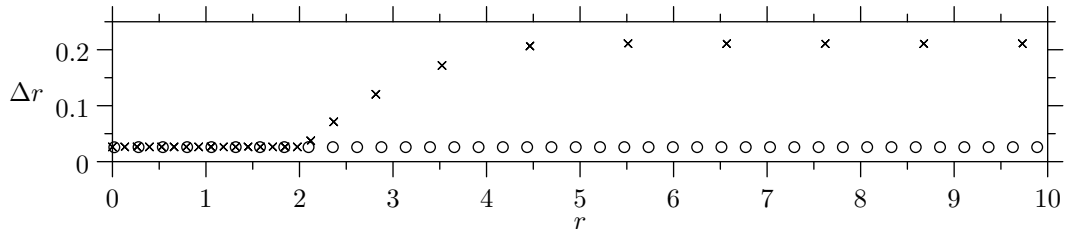


Figure 4.1 – Grid spacing in radial direction. The crosses correspond to every 5th point of the simulation grid. The circles correspond to every 10th point of the modified grid used for Hankel transforms.

4.2.2 Steady flow

The steady flow is calculated by using 300 snapshots in time that are uniformly distributed over a duration $T = 31.4259$. The duration corresponds to $6T_{1,2}$, $11T_{2,2}$ and $17T_{3,4}$, where $T_\omega = 2\pi/\omega$ is the period associated with frequency ω . The time-averaged axial momentum $(\rho u)_0$ is plotted in figure 4.2(a). The velocity profile of figure 4.2(b) shows that the end of the potential core is between 4 to 6 jet diameters.

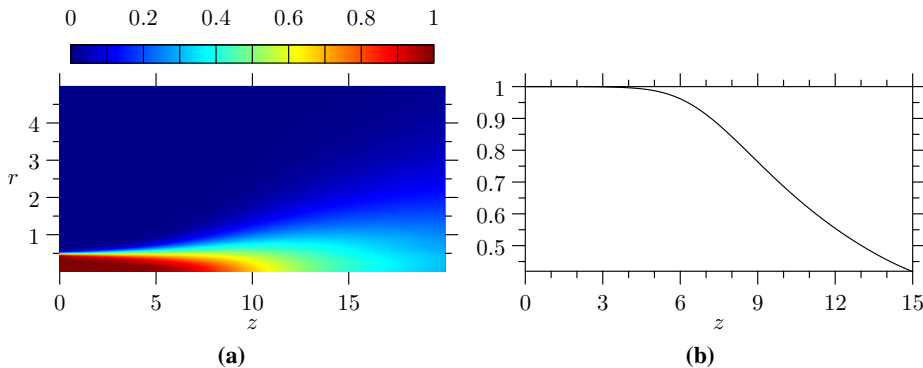


Figure 4.2 – Steady part $(\rho u)_0$ of axial momentum field (left) and corresponding profile along $r = 0$ (right). The end of the potential core is between 5 and 6 jet diameters.

The computed steady flow is slightly different from the prescribed mean flow of Stromberg *et al.* [23] (obtained by a functional fit of experimental data, see e.g. reference [46]). The absolute error between the prescribed mean flow and the computed one is shown in table 4.1 for each flow variable, using the l_∞ norm. The error is found to be always less than 2% i.e. small compared to the amplitude of the computed steady flow (except for $(\rho v)_0$ where the error is of a similar order of magnitude for $z > 10$). The distribution of the error throughout the domain is shown in the appendix, in figure B.2. Since the error is not small compared to the amplitude of acoustic and hydrodynamic fluctuations, the computed steady flow will be used rather than the prescribed steady flow for all of the computations.

	ρ_0	$(\rho u)_0$	$(\rho v)_0$	π_0
error	7.3×10^{-3}	2.1×10^{-2}	3.8×10^{-3}	1.2×10^{-4}

Table 4.1 – Error l_∞ between the mean flow variables computed using time averaging and the ones prescribed in the simulation to match the mean flow of Stromberg.

In the simulations of Suponitsky and Sandham [31], the prescribed mean flow of Stromberg *et al.* [23] is maintained by means of an external source term. When disturbances are introduced in the domain, they interact nonlinearly. Some nonlinear interactions lead to zero frequency components that

alter the mean flow. This alteration can be significant if the amplitudes of the disturbances is large. In figure 4.3 the computed and prescribed mean flow profiles are compared for different axial positions and for $z \leq 10$. It shows that the comparison is very good. Since this is the region where most of the sound is expected to be generated (this assumption will be verified in section 4.4), the variations between prescribed and computed mean flows should have little effect on the physical mechanisms of sound generation.

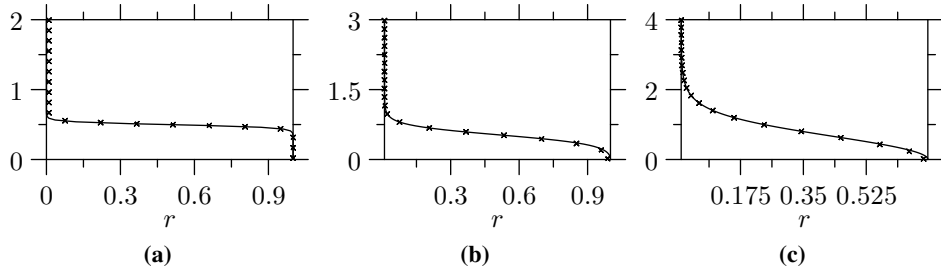


Figure 4.3 – Profiles of mean axial momentum $(\rho u)_0$ for $z = 0$ (a), $z = 5$ (b) and $z = 10$ (c). Crosses represent the computed mean variable; the solid lines represent the prescribed mean flow.

4.2.3 Unsteady flow

Figure 4.4(a) shows a snapshot of the unsteady modified pressure field $\pi - \pi_0$ at time $t = 157.18$. Similar snapshots for the other flow variables are shown in appendix B in figure B.3. They are computed by subtracting the steady flow field described in section 4.2.2 from the instantaneous flow field. Hydrodynamic waves can be seen along the jet axis, for $r \leq 10$, and acoustic waves are radiating to the far field.

The instantaneous directivity $D_q(t, \theta, R)$ of each flow variable q is computed as

$$D_q(t, \theta, R) = 20 \log(|q(t, \theta, R) - q_0| / q_{\text{ref}}), \quad (4.2)$$

where $R = \sqrt{z^2 + r^2}$, $\theta = \arctan(r/z)$ (for $z > 0$) and $q_{\text{ref}} = 5 \times 10^{-7}$. To compute $D_\pi(t, \theta, r)$ 100 points are used for θ between 20° and 85° . Each angle θ is associated with the value of q at the point (z, r) that is such that R is closest to 25 jet diameters. Local fluctuations are smoothed out using a 5 point moving average filter. The instantaneous directivity of the modified pressure field at time $t = 157.18$ is shown in figure 4.4(b). The peak radiation angle is 25° . A side lobe can also be observed towards 78° .

Profiles of the unsteady modified pressure field are plotted in figure 4.5 for $r = 0$ and 25. They illustrate the differences in terms of the structure and amplitude between the near field and the far field. In the far field (right

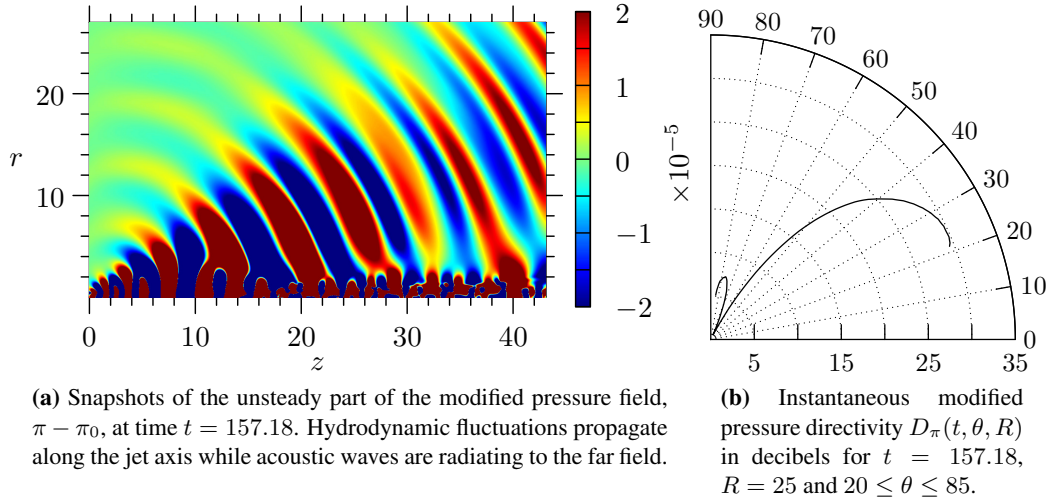


Figure 4.4 – Unsteady modified pressure field $\pi - \pi_0$ in the physical domain at time $t = 157.18$: (a) pseudo-colour plot, (b) directivity.

column), pressure has a low amplitude (10^{-5}) and a low wavenumber content, with regular acoustic oscillations. On the contrary, in the near field (left column), pressure has a higher amplitude (10^{-2}) and a more complex behaviour due to the presence of smaller length scales.

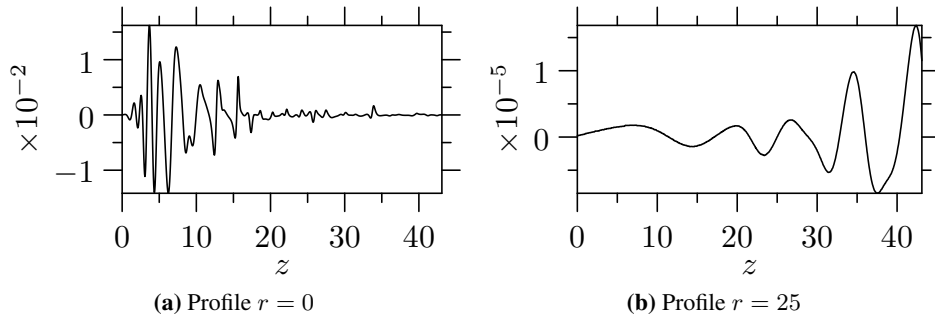


Figure 4.5 – Profiles of the unsteady modified pressure field $\pi - \pi_0$ in the physical domain at time $t = 157.18$, in the hydrodynamic region (left) and in the acoustic region (right)

4.2.4 Frequency analysis

The flow field is now studied to gain an understanding of its frequency content, especially in the far field. This is important as it will allow the effort to be concentrated on the frequencies that dominate the sound field.

The power spectral density (PSD) describes the power distribution in the

pressure field. The raw PSD is computed as

$$\text{PSD}(z, r, \omega) = \frac{|\pi(z, r, \omega)|^2}{M\Delta t} \quad (4.3)$$

where $\pi(z, r, \omega)$ is the Fourier transform in time of the modified pressure field $\pi(z, r, t)$, $M = 300$ is the number of samples and $\Delta t \approx 0.10472$ is the sampling time. The modified pressure field is recorded over all time frames at point $(z, r) = (40, 20)$ which is roughly in the direction of maximum radiation. The record length has been chosen to make $\Delta\omega = 0.2$. The corresponding PSD is computed using (4.3). The result is shown in figure 4.6. One can see that the frequencies 1.0 and 1.2 are dominating the radiating field. Frequency 2.2 is also significant, but is 10dB smaller than the peak frequency (1.2). All other frequencies are at least 17dB smaller than the 2.2 level. Thus, although the excitation frequencies are 2.2 and 3.4, the peak frequency corresponds to the difference frequency 1.2.

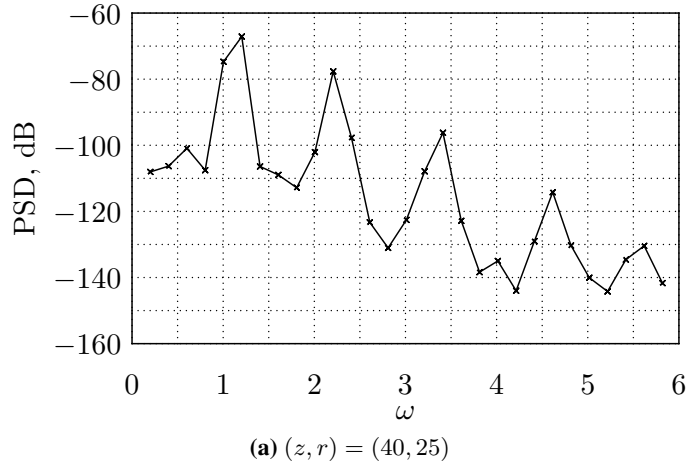


Figure 4.6 – Power spectrum density (PSD) of modified pressure π at point $(z, r) = (40, 20)$ situated in the acoustic region. The excitation frequencies are $\omega_1 = 2.2$ and $\omega_2 = 3.4$ but the radiating field is dominated by the interaction frequency $\Delta\omega = 1.2$.

Figure 4.6 gives the frequency content of the modified pressure field at one particular position. To gain a better understanding of how these frequencies are distributed throughout the domain, $\pi(z, r, t)$ is expressed as a sum of single frequency components using an inverse Fourier transform in time:

$$\pi(z, r, t) = \frac{1}{2\pi} \int_{-\infty}^{+\infty} \pi(z, r, \omega) e^{-j\omega t} d\omega = \int_0^{+\infty} \pi_\omega(z, r, t) d\omega,$$

where

$$\pi_\omega(z, r, t) = \frac{1}{2\pi} [\pi(z, r, \omega)e^{-j\omega t} + \pi(z, r, -\omega)e^{j\omega t}]. \quad (4.4)$$

Equation (4.4) shows that $\pi_\omega(z, r, t)$ is the instantaneous modified pressure field at frequencies ω and $-\omega$. Note that, because $\pi(z, r, t)$ is real, $\pi(z, r, -\omega)$ is the complex conjugate of $\pi(z, r, +\omega)$, so that

$$\pi_\omega(z, r, t) = \frac{1}{\pi} [\mathcal{R}\{\pi(z, r, \omega)\} \cos(\omega t) + \mathcal{I}\{\pi(z, r, \omega)\} \sin(\omega t)], \quad (4.5)$$

where $\mathcal{R}\{\cdot\}$ and $\mathcal{I}\{\cdot\}$ denote the real and imaginary parts of a complex number. Equation (4.5) is important and will be used extensively hereafter. In particular, it allows to examine the instantaneous contribution of frequencies $\pm\omega$ to $\pi(z, r, t)$ (or any other flow variable): $\pi_\omega(z, r, t)$ can now be studied for the radiating frequencies $\omega = 1.0, 1.2$ and 2.2 .

The results are shown in figure 4.7. The dominant frequencies in the radiating field are $\omega = 1.0, 1.2$ and 2.2 . Figure 4.8(a) shows profiles of the unsteady modified pressure $\pi_\omega(z, r, t)$ at time $t = 157.18$ along $r = 25$, for $\omega = 1.0, 1.2$ and 2.2 . The sum of $\pi_\omega(z, r, t)$ for $\omega = 1.0, 1.2$ and 2.2 is compared to $\pi(z, r, t) - \pi_0$ in figure 4.8(b). Agreement is very good. The aim will therefore be to find the sound sources associated with these three frequencies.

Finally one can discover where the non-radiating waves reach their maximum in the near field by examining $|\pi(z, r, \omega)|$ for $r \leq 2$ and $\omega = 1.0, 1.2$ and 2.2 (see figure B.6 in appendix). This is useful to estimate the convection speed of the structures associated with these frequencies. The position (z_0, r_0) , where the amplitude $|\pi(z, r, \omega)|$ of the Fourier transform of the modified pressure field is maximum, is presented for each frequency in table 4.2. In every case, the peak location is within the jet shear layer ($r_0 \approx 0.5$) but it varies in the streamwise direction. For $\omega = 1.2$ and 2.2 , the peak location is within 3 jet diameters from the end of the potential core. For $\omega = 1.0$, the peak location is further downstream. For each frequency, the convection velocity of the non-radiating components is then estimated by measuring the streamwise velocity at the point where $|\pi(z, r, \omega)|$ is maximum. Note that the convection velocity is easily computed from the Fourier transform. The independent estimation of convection velocity presented here will however serve as a simple check for the computation of the Fourier transform. The results are summarized in table 4.2.

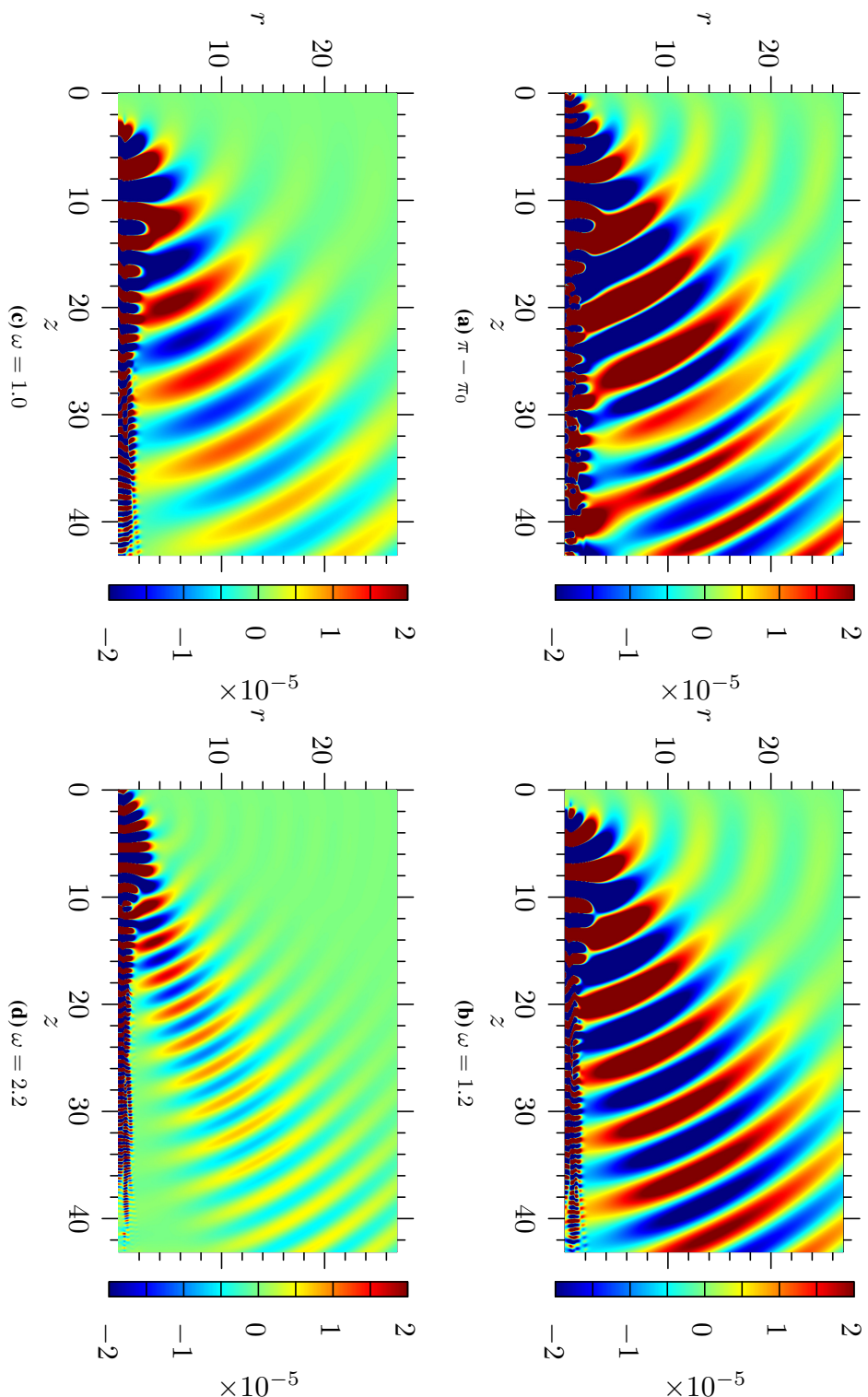


Figure 4.7 – Instantaneous frequency decomposition $\pi_\omega(z, r, t)$ of modified pressure $\pi(z, r, t)$ at $t = 157.18$ for the main radiating frequencies, $\omega = 1.0, 1.2$ and 2.2 . The unsteady modified pressure field $\pi - \pi_0$ is included in figure (a) for comparison. Frequency 1.2 is the dominant frequency, but significant noise is also radiating at $\omega = 1.0$ and 2.2 are also significant.

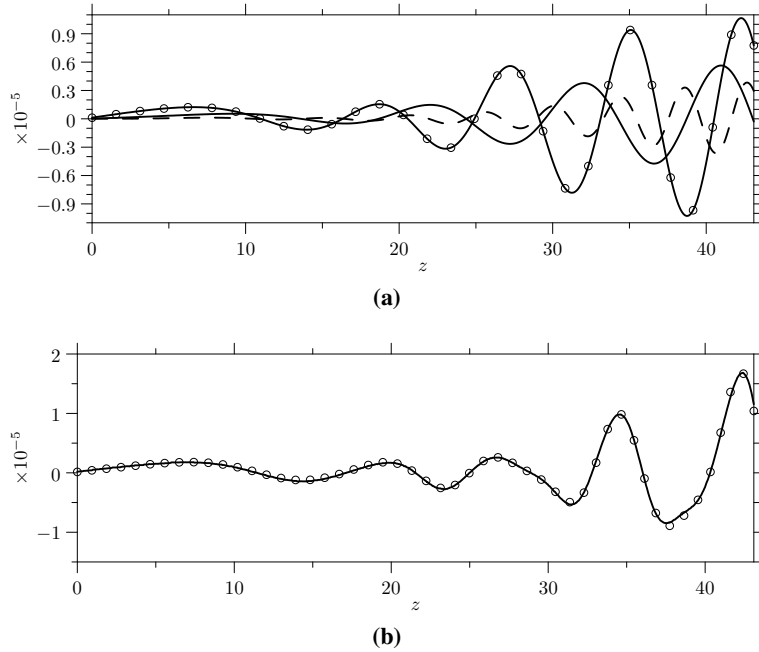


Figure 4.8 – Unsteady modified pressure profiles of $\pi - \pi_0$ along $r = 25$ at time $t = 157.18$. In (a), π is decomposed into frequency components 1.2 (solid line with circles), 1.0 (solid line) and 2.2 (dashed line). In (b), $\pi - \pi_0$ (solid line) is compared to $\pi_{1.0} + \pi_{1.2} + \pi_{2.2}$ (circles).

ω	z_0	r_0	u_{c0}
1.0	10.9	0.59	0.48
1.2	7.6	0.5	0.58
2.2	5.3	0.48	0.62

Table 4.2 – Estimation of the convection velocity u_{c0} , based on the value of the streamwise velocity at the point where $|\pi(z, r, \omega)|$ is maximum, as a function of the radiating frequency ω .

4.2.5 Wavenumber analysis

For each radiating frequency ω_r , such as 1.2, the instantaneous modified pressure field $\pi_{\omega_r}(z, r, t)$ can be Fourier transformed in space to obtain the modified pressure distribution $\Pi_{\omega_r}(k_z, k_r)$ in the wavenumber domain. Note that since the modified pressure field is axisymmetric, the 2D spatial Fourier transform is obtained by using a 1D Fourier transform in the axial direction and a 1D Hankel transform of order 0 in the radial direction (see appendix A).

Figure 4.9 shows the Fourier transform of the modified pressure field at the radiating frequencies. For each frequency, radiating components can be seen around the radiation circle defined as $|\mathbf{k}| = \omega/c_\infty$ (see table 4.3). These radiating components are clearly separated from the non-radiating components, which are centered around $k_{z,nr}$. The convection velocity u_c is related to ω

and $k_{z,nr}$ by $u_c = \omega/k_{z,nr}$. The values of u_c as a function of ω are given in table 4.3. They are in very good agreement with the estimates u_{c0} of table 4.2 except for $\omega = 1.0$ ($u_{c0} = 0.48$ and $u_c = 0.56$). The discrepancy for $\omega = 1.0$ is most likely due to a poor estimation of u_{c0} . Thus, for the most part, the radiating and non-radiating components are where expected in the wavenumber-frequency domain. This validates the computation of the Fourier transform.

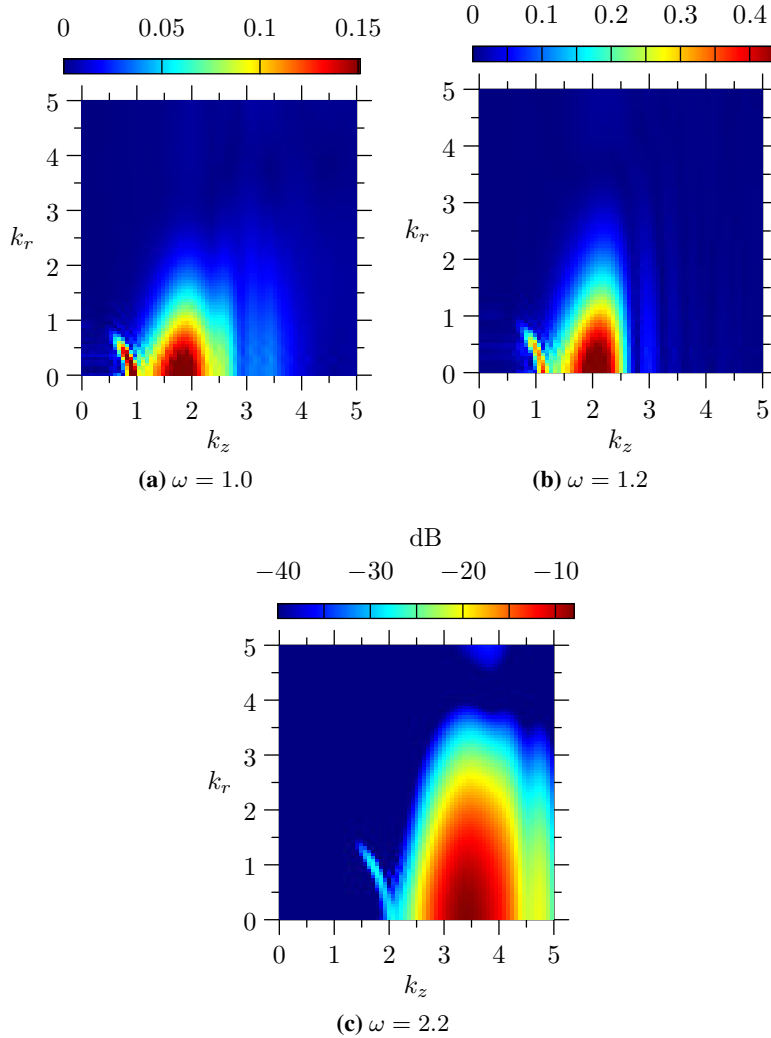


Figure 4.9 – Fourier transform in space of instantaneous modified pressure $\pi_{\omega_r}(t, z, r)$ at $t = 157.18$ for $\omega_r = 1.0, 1.2$ and 2.2 . The radiating components can be seen on the radiation circle defined as $|\mathbf{k}| = \omega/c_\infty$ (see table 4.3).

4.3 Flow filtering

In the previous section, the flow field has been studied in both the physical and spectral domains. In particular the dominant frequencies, at which most

ω	ω/c_∞	$k_{z,nr}$	u_c
1.0	0.9	1.8	0.56
1.2	1.1	2.1	0.57
2.2	2.0	3.5	0.63

Table 4.3 – Ratio ω/c_∞ , axial non-radiating wavenumber $k_{z,nr}$ measured where $\pi_\omega(k_z, k_r, t = 157.18)$ is maximum (from figure 4.9), and convection velocity $u_c = \omega/k_{z,nr}$ for the radiating frequencies $\omega = 1.0, 1.2$ and 2.2 .

of the sound is radiating, have been identified and the locations of the radiating and non-radiating components have been determined in the spectral domain. The clear separation between the two locations allows one to decompose the flow into radiating and non-radiating components using convolution filters. This is the subject of the present section.

4.3.1 Algorithm

Description

The algorithm used to identify the radiating part of a flow variable $q(z, r, t)$ can be decomposed into four successive steps. The steps are presented in figures 4.10, 4.11 and 4.12.

First, $q(z, r, t)$ is decomposed into the single frequency variables $q_{1.0}(z, r, t)$, $q_{1.2}(z, r, t)$ and $q_{2.2}(z, r, t)$ (figure 4.10). These single frequency variables represent the instantaneous part of $q(z, r, t)$ at the radiating frequencies $\omega_r = 1.0, 1.2$ and 2.2 which are those that dominate the acoustic field (see section 4.2.4). This is done for each radiating frequency ω_r by:

- computing the value of the Fourier transform $Q(z, r, \omega_r)$,
- computing $q_{\omega_r}(z, r, t)$ from the real and imaginary parts of $Q(z, r, \omega_r)$, as shown in equation (4.5) in the case of the modified pressure field π .

Second, for a given time t and for each value of ω_r , the radiating part of $q_{\omega_r}(z, r, t)$, denoted $q'_{\omega_r}(z, r, t)$, is computed by applying a convolution filter implemented in the wavenumber domain. Convolution filters have been described in section 3.4. This step is described in figure 4.11 and requires to

- compute the Hankel transform of $q_{\omega_r}(z, r, t)$ in the radial direction (HT),
- compute the Fourier transform in the axial direction (FT_z),
- multiply by the filter window designed to return the radiating components satisfying $|\mathbf{k}| = \omega_r/c_\infty$,
- compute the real part of the inverse Fourier transform in the axial direction (FT_z^{-1})
- compute the inverse Hankel transform in the radial direction (HT^{-1}).

Note that for axisymmetric variables, HT denotes the Hankel transform of order 0 (appendix A). The radial momentum ρv is not axisymmetric but $\rho v \mathbf{e}_r$ is, where \mathbf{e}_r denotes the unit vector in the radial direction. This means that a Hankel transform of order 1 must be used when $q = \rho v$. A detailed proof of this result is presented in appendix A.

Third, the radiating part of $q(z, r, t)$ is obtained by summing the values of $q'_{\omega_r}(z, r, t)$ for all the radiating frequencies ω_r (figure 4.12), i.e.

$$q'(z, r, t) = q'_{1.0}(z, r, t) + q'_{1.2}(z, r, t) + q'_{2.2}(z, r, t). \quad (4.6)$$

Finally, the non-radiating field $\bar{q}(z, r, t)$ is obtained by subtracting $q'(z, r, t)$ from $q(z, r, t)$:

$$\bar{q}(z, r, t) = q(z, r, t) - q'(z, r, t). \quad (4.7)$$

Note that decomposing $q(z, r, t)$ into the instantaneous single frequency variables $q_{\omega_r}(z, r, t)$ is a crucial step of the algorithm. This is because, for a single frequency signal, radiating components ($|\mathbf{k}| = \omega/c_\infty$) are well separated from the non-radiating ones ($k_z \approx \omega/u_c$); on the contrary, for a multiple frequency signal in the wavenumber domain, the non-radiating components at one frequency (e.g. $k_z \approx 2.1$ for $\omega = 1.2$, from figure 4.9(b)) can overlap with the radiating components at another frequency (e.g. $k_z = 2.0$ for $\omega = 2.2$, from figure 4.9(c)).

Besides, q' is computed efficiently since for each radiating frequency ω_r , q'_{ω_r} is obtained for all times by filtering only two signals (the real and imaginary parts of q'_{ω_r}) in the wavenumber domain. Thus, the expensive steps required to compute q' are: (a) the Fourier transform of q over time to obtain q_{ω_r} for ω_r in $\{1.0, 1.2, 2.2\}$, and (b) the Fourier transforms in space of the real and imaginary parts of q_{ω_r} (six transforms in total). This is in contrast with computing the full Fourier transform in space and time as would be required to obtain \bar{q} directly.

Implementation

The Fourier transform is carried out numerically using the Fast Fourier Transform algorithm. The Hankel transform is implemented using the Quasi Discrete Hankel Transform (QDHT) of Guizar-Sicairos *et al.* [47]. The QDHT expects the data to be defined on a special grid that depends on three parameters: the number of points, the maximum value in the radial direction and the order of the Hankel transform. This means that the data must be interpolated in the radial direction, as explained in section 4.2.1. The interpolation

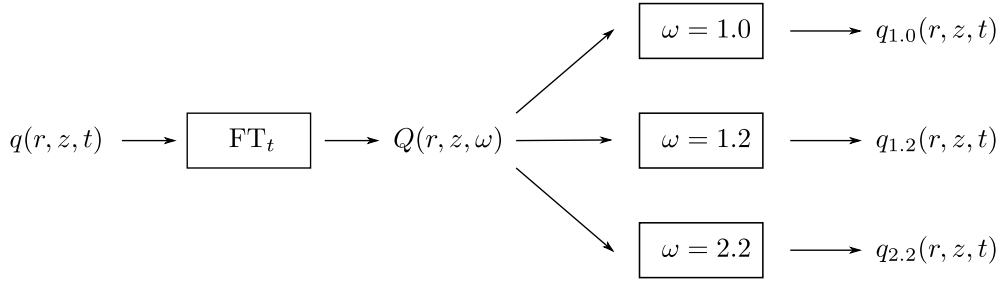


Figure 4.10 – Algorithm, step 1. The flow variable $q(z, r, t)$ is Fourier transformed in time (FT_t) to obtain $Q(z, r, \omega)$. Using equation (4.5), each Fourier component $Q(z, r, \omega)$ can then be inverse transformed into a physical signal $q_\omega(z, r, t)$ which corresponds to the instantaneous contributions of frequencies ω and $-\omega$ to $q(z, r, t)$. This is done only for the frequencies $\omega = 1.0, 1.2$ and 2.2 at which most of the sound is radiating.

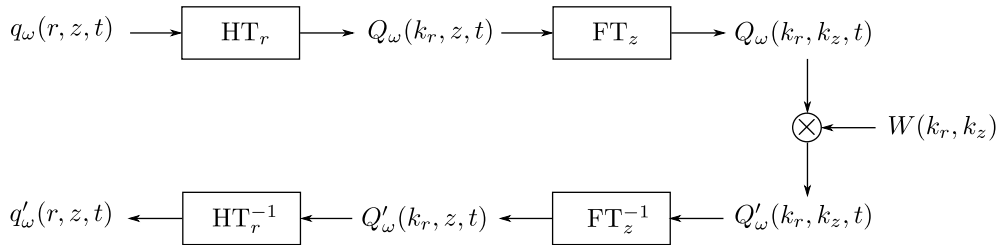


Figure 4.11 – Algorithm, step 2. The single frequency signals $q_{\omega_r}(z, r, t)$ are filtered to obtain $q'_{\omega_r}(z, r, t)$ by using a radiating convolution filter applied in the wavenumber domain. The full Fourier transform is obtained by applying a Hankel transform (HT) in the radial direction and a Fourier transform (FT_z) in the axial direction.

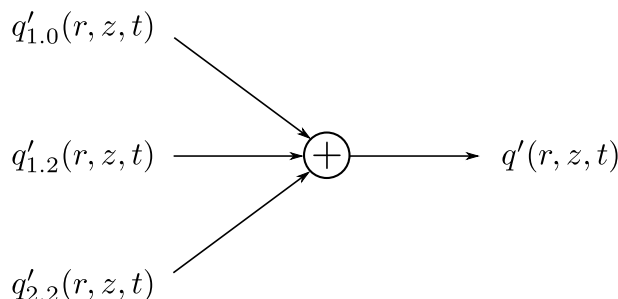


Figure 4.12 – Algorithm, step 3. The radiating part of $q'(z, r, t)$ is obtained by summing $q'_{\omega_r}(z, r, t)$ for the radiating frequencies ω_r which dominate the sound field.

is carried out using a second order bivariate spline algorithm [49]. Finally, if the input data is of size (N_r, N_z) , it is zero-padded to size $(2N_r, 2N_z)$ before applying the transforms to avoid aliasing and mitigate boundary effects (section 3.4.2).

Most of the implementation is written in the Python programming language [50] and relies on the numerical libraries Numpy [51] and Scipy [52]. The Hankel transform is implemented using Fortran 90 [53] and called from Python with F2PY [54].

4.3.2 Filter definition

The filter window $W(\mathbf{k}, \omega)$ should have a value of 1 in a narrow band centered on the radiation circle $|\mathbf{k}| = \omega/c_\infty$ and of 0 everywhere else. This corresponds to strategy (b) in figure 3.7. A Gaussian filter of standard deviation $\sigma = 0.37$ is used to achieve this:

$$W(\mathbf{k}, \omega) = \exp \left[-\frac{(|\mathbf{k}| - |\omega|/c_\infty)^2}{2\sigma^2} \right] \quad (4.8)$$

The filter window is plotted in figure 4.13. The value of σ corresponds to $4\Delta k$, where $\Delta k = \sqrt{\Delta k_r^2 + \Delta k_z^2}$. The amplitude of the filter window is 0.02 for $(k_r, k_z) = (0.0, 2.1)$, i.e. where the non-radiating component is maximum (see figure 4.9(b)), so the filter should remove most of the non-radiating components at frequency 1.2 from the flow.

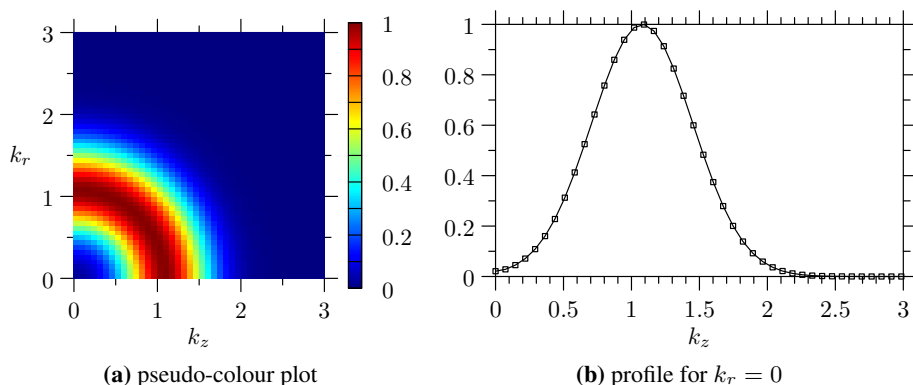


Figure 4.13 – Filter window $W_{1.2}(k_r, k_z)$ for the laminar jet problem for radiating frequency $\omega_r = 1.2$.

4.3.3 Results

Filtered flow in the wavenumber-frequency domain

Figure 4.14 shows pseudo-colour plots of the radiating modified pressure $\Pi'_{1.2}$ and non-radiating modified pressure $\bar{\Pi}_{1.2}$ at frequency 1.2 and time $t = 157.18$, using the Gaussian filter of equation (4.8). The decomposition appears to successfully separate the radiating and non-radiating components without distorting their amplitudes, as can be seen by comparing figures 4.14(a) and 4.14(b) with figure 4.9(b). Similar results are obtained for all the flow variables at all the radiating frequencies (see figure B.8 in appendix).

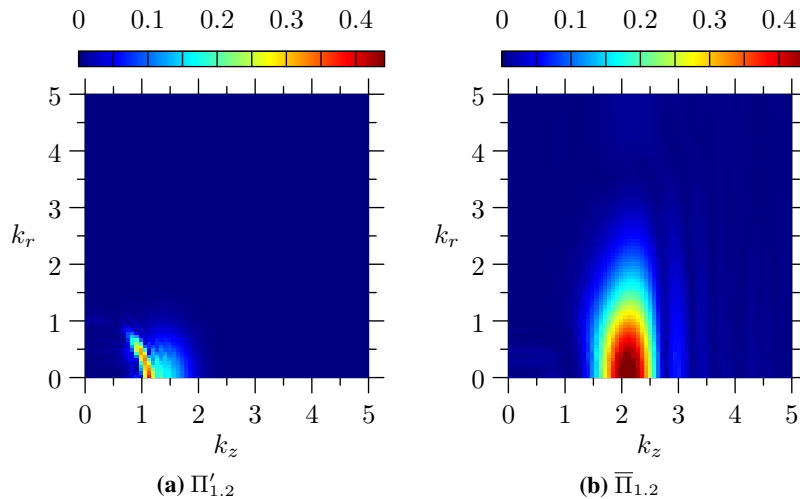


Figure 4.14 – Radiating $\Pi'_{1.2}$ (a) and non-radiating modified pressure $\bar{\Pi}_{1.2}$ (b) at radiating frequency $\omega = 1.2$.

Filtered flow in the space domain

The radiating and non-radiating modified pressure fields $\pi'_{1.2}$ and $\bar{\pi}_{1.2}$ at frequency 1.2 are shown in figure 4.15. Pseudo colour plots of $\bar{\pi}_{1.2}$ and $\pi'_{1.2}$ are shown respectively in figure 4.15(a) and figure 4.15(b). Sound radiation is clearly absent from $\bar{\pi}_{1.2}$ and non-radiating components are absent from $\pi'_{1.2}$: qualitatively the decomposition of the modified pressure field at frequency 1.2 into radiating and non-radiating components is successful. Profiles of $\bar{\pi}_{1.2}$ and $\pi_{1.2}$ along $r = 0$ are shown in figure 4.15(c). Profiles of $\pi'_{1.2}$ and $\pi_{1.2}$ along $r = 25$ are shown in figure 4.15(d). From 4.15(c), one can see that $\bar{\pi}_{1.2}$ is in very good agreement with $\pi_{1.2}$ in the near field. This means that the filter does not distort the non-radiating components. Moreover, from 4.15(d), $\pi'_{1.2}$ and $\pi_{1.2}$ are in good agreement in the far field which shows that most of

the radiating components at frequency 1.2 are captured by the filter. Similar results for the modified pressure field at the two other radiating frequencies $\pi_{1.0}$ and $\pi_{2.2}$ are shown in appendix in figure B.9 and B.10 respectively.

The total radiating modified pressure field is obtained by summing the contributions of all the radiating frequencies. Pseudo colour plots of $\bar{\pi}$ and π' are shown in figures 4.16(a) and 4.16(b). Profiles of $\bar{\pi} - \pi_0$ and $\pi - \pi_0$ along $r = 0$, and of π' and $\pi - \pi_0$ along $r = 25$, are shown respectively in figure 4.16(a) and 4.16(b). These figures show that the conclusions obtained for the decomposition of the single frequency modified pressure field $\pi_{1.2}$ hold for the total modified pressure field π : the decomposition into radiating and non-radiating components is successful. Similar results are obtained for the other flow variables, ρ , ρu and ρv , as demonstrated by figures B.11, B.12 and B.13 presented in the appendix.

An interesting outcome of the flow decomposition presented in the previous paragraph is that the magnitudes of the radiating and non-radiating components can be quantified within the flow. A comparison of the peak values of \bar{q} and $\bar{q} - q_0$ with q' , along $r = 0$ for q in $\{\rho, \rho u, \pi\}$, and along $r = 0.5$ for $q = \rho v$, is given in table 4.4. The results show that $q' \sim 10^{-4}\bar{q}$ for all flow variables, which validates the commonly made assumption of chapter 2 that $q' \ll \bar{q}$. Moreover, q' is two to four orders of magnitude smaller than the unsteady part of \bar{q} , i.e. $\bar{q} - q_0$.

Flow variable q	ρ	ρu	ρv	π
$\max(q')/\max(\bar{q})$	7.0×10^{-4}	3.9×10^{-4}	9.6×10^{-4}	7.6×10^{-4}
$\max(q')/\max(\bar{q} - q_0)$	2.9×10^{-2}	2.3×10^{-3}	9.5×10^{-4}	4.4×10^{-2}

Table 4.4 – Comparison of the peak value of q' with that of \bar{q} and $\bar{q} - q_0$, along $r = 0$ for $q \in \{\rho, \rho u, \pi\}$, and along $r = 0.5$ for $q = \rho v$.

Valuable insights can also be gained by discussing the location of the maximum values of the radiating and non-radiating flow variables. These are summarized in table 4.5. For the non-radiating base flow, the peak value is located close the jet exit, around $z = 4$, except for $\bar{\rho v}$ for which the peak is further downstream ($z = 22$). This indicates that fluctuations in the radial direction become larger downstream of the end of the potential core. Note however that, apart from π , the unsteady part of the non-radiating base flow reaches its maximum between 12 and 22 jet diameters. Most importantly, it is found that the radiating part is maximum between 7 and 8 jet diameters, which is 1 to 4 jet diameters downstream of the end of the potential core. This suggests that the main sound source is also located in that region which, as described in section 1.6, has been associated with sound generation by large scale structures

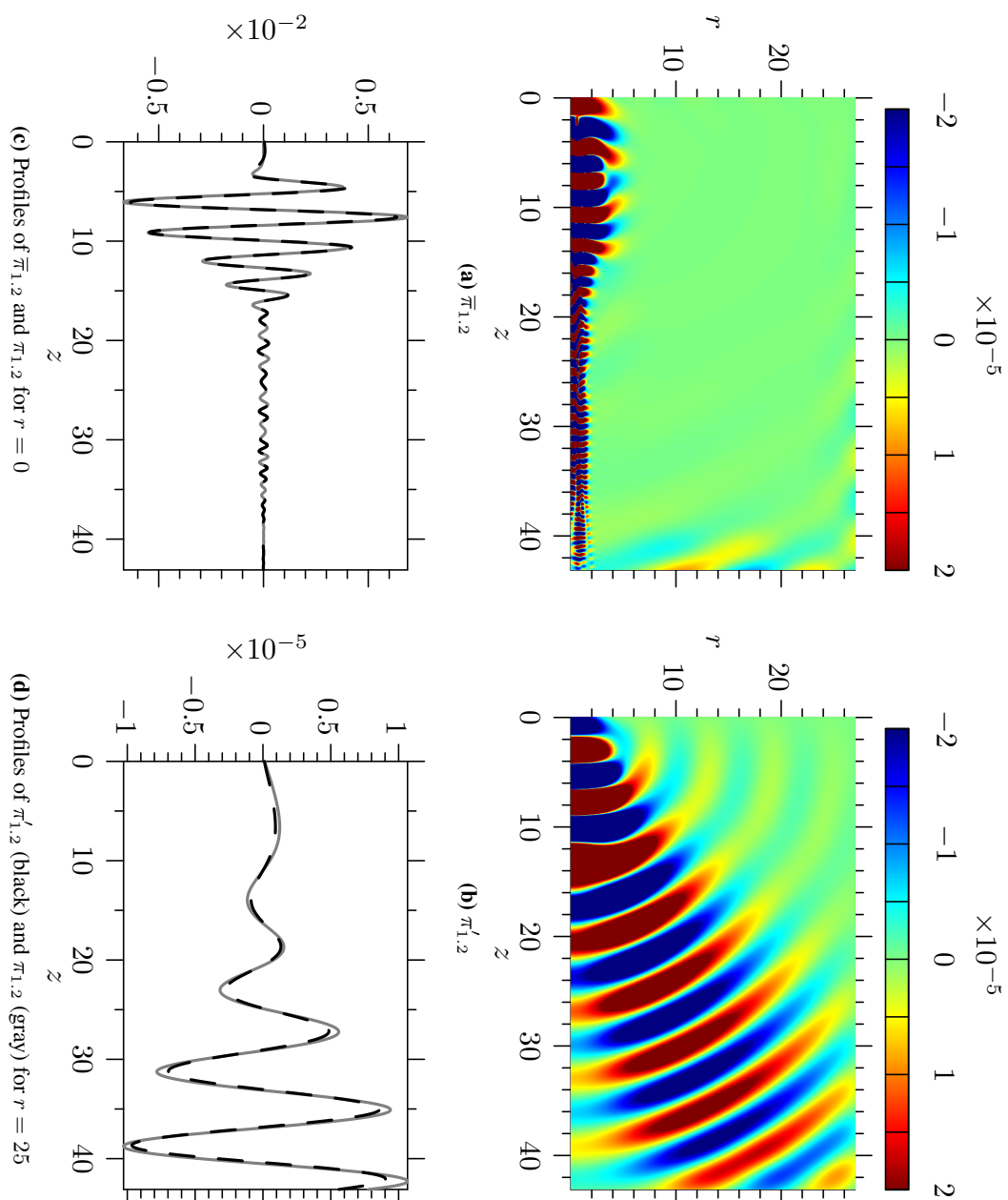


Figure 4.15 – Pseudo colour plots and profiles of non radiating modified pressure $\bar{\pi}_{1,2}$ ((a) and (c)) and radiating modified pressure $\pi'_{1,2}$ ((b) and (d)) at radiating frequency $\omega_r = 1.2$ and time $t = 157.18$. The profiles are taken both in the source region (c) and acoustic region (d), at $r = 0$ and $r = 25$ respectively. In the profiles ((c) and (d)), the gray solid line represents $\pi_{1,2}$. The dashed black line represents $\bar{\pi}_{1,2}$ in (c) and $\pi'_{1,2}$ in (d).

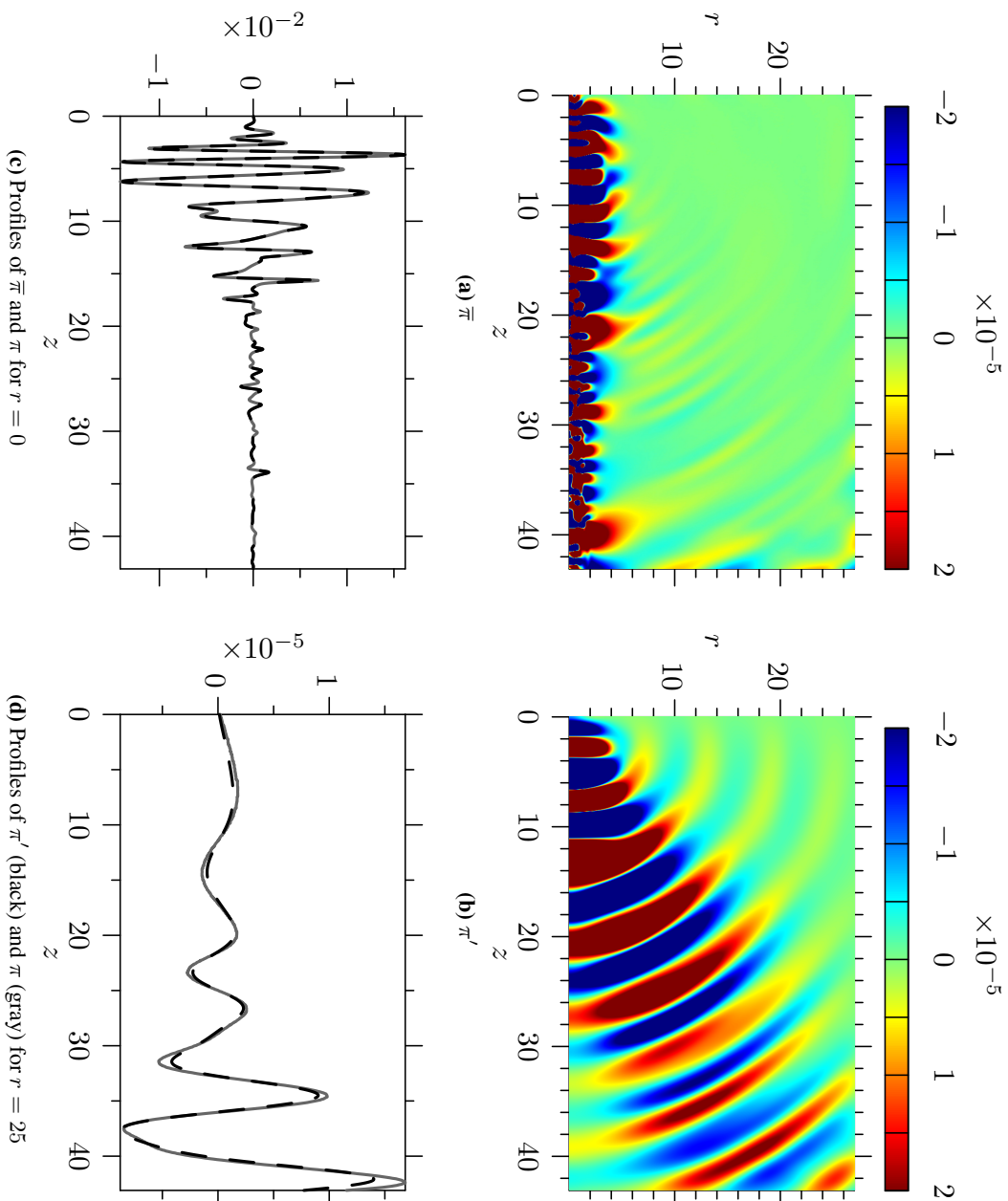


Figure 4.16 – Pseudo colour plots and profiles of non radiating modified pressure $\bar{\pi}$ ((a) and (c)) and radiating modified pressure π' ((b) and (d)) at time $t = 157.18$. The profiles are taken both in the source region (c) and acoustic region (d), at $r = 0$ and $r = 25$ respectively. In the profiles ((c) and (d)), the gray solid line represents $\bar{\pi} - \pi_0$. The dashed black line represents $\bar{\pi}$ in (c) and π' in (d).

by several investigators.

Flow variable q	ρ	ρu	ρv	π
z -location of $\max(\bar{q})$	3.7	4.3	22.2	3.7
z -location of $\max(q')$	7.6	7.8	6.8	7.7
z -location of $\max(\bar{q} - q_0)$	15.7	12.5	22.2	3.7

Table 4.5 – Comparison of the peak location of q' , \bar{q} and $\bar{q} - q_0$, along $r = 0$ for $q \in \{\rho, \rho u, \pi\}$, and along $r = 0.5$ for $q = \rho v$.

4.4 NRBF sources

4.4.1 Algorithm

The algorithm used to compute the NRBF sources is as follows:

- compute $\bar{\rho}$, $\bar{\rho}u$, $\bar{\rho}v$ by substituting q with the relevant variable in the algorithm described in section 4.3.1,
- compute the Favre-averaged quantities $\tilde{u} = \bar{\rho}u/\bar{\rho}$ and $\tilde{v} = \bar{\rho}v/\bar{\rho}$,
- compute the vector \mathbf{e} , defined as

$$\mathbf{e} \equiv \begin{pmatrix} \partial(\bar{\rho}\tilde{u}\tilde{u})/\partial z \\ (1/r)\partial(r\bar{\rho}\tilde{u}\tilde{v})/\partial r \\ \partial(\bar{\rho}\tilde{v}\tilde{u})/\partial z \\ (1/r)\partial(r\bar{\rho}\tilde{v}\tilde{v})/\partial r \end{pmatrix}, \quad (4.9)$$

which contains the terms composing the divergence of vectors $\bar{\rho}\tilde{u}\tilde{v}$ and $\bar{\rho}\tilde{v}\tilde{v}$ in cylindrical coordinates,

- compute the radiating part \mathbf{e}'_{ω_r} of \mathbf{e} for each radiating frequency $\omega_r \in \{1.0, 1.2, 2.2\}$,
- compute the NRBF sources $(f_{1z})_{\omega_r}$ and $(f_{1r})_{\omega_r}$ for each radiating frequency ω_r , defined from (2.26) as

$$(f_{1z})_{\omega_r} = -(e_1 + e_2)'_{\omega_r} \quad (4.10)$$

$$= - \left(\frac{\partial}{\partial z} (\bar{\rho}\tilde{u}\tilde{u}) \right)'_{\omega_r} - \left(\frac{1}{r} \frac{\partial}{\partial r} (r\bar{\rho}\tilde{u}\tilde{v}) \right)'_{\omega_r}, \quad (4.11)$$

$$(f_{1r})_{\omega_r} = -(e_3 + e_4)'_{\omega_r} \quad (4.12)$$

$$= - \left(\frac{\partial}{\partial z} (\bar{\rho}\tilde{v}\tilde{u}) \right)'_{\omega_r} - \left(\frac{1}{r} \frac{\partial}{\partial r} (r\bar{\rho}\tilde{v}\tilde{v}) \right)'_{\omega_r}. \quad (4.13)$$

4.4.2 Results and discussion

Source decomposition

The four components of the vector \mathbf{e} of equation (4.9) are decomposed at the radiating frequencies 1.0, 1.2 and 2.2. This is done by computing the Fourier transform of \mathbf{e} in time and by using equation (4.5). Figure 4.17 shows the result of such a decomposition for frequency 1.2, in both the space domain (left column) and the wavenumber domain (right column). In figure 4.17, each row corresponds to one of the components of $(\mathbf{e})_{1.2}$. In the space domain, the two dominant terms in $\mathbf{s}_{1.2}$ are $(e_1)_{1.2}$ and $(e_2)_{1.2}$. These terms are distributed along the jet axis and reach their maximum around $z = 10$. The remaining terms, $(e_3)_{1.2}$ and $(e_4)_{1.2}$, are distributed along the shear layer ($r = 0.5$) and are smaller by an order of magnitude.

The wavenumber plots in the right column of figure 4.17 show the absence of any clear components along the radiation circle $|\mathbf{k}| = 1.08$. This is in contrast, for example, with the results of figure 4.9. However, if the maximum colour level was decreased by two orders of magnitude, one would see that the tail of the large non-radiating components actually intersects the radiation circle. This means that, although they are invisible in figure 4.17, $(\mathbf{e})_{1.2}$ does contain some radiating components. This will become clear when the radiating part of $(\mathbf{e})_{1.2}$ is plotted (in figure 4.19). The present observation implies that only a very small portion of \mathbf{e} radiates noise.

Filter definition

A Gaussian radiating filter, as defined in equation (4.8), is used to extract the radiating components from $(\mathbf{e})_{\omega_r}$. The filter depends only on the value of the standard deviation σ . The value of σ is defined in terms of the radius of the radiation circle by

$$\sigma(\omega_r) = \frac{1}{7.5} \frac{\omega_r}{c_\infty}, \quad (4.14)$$

so σ increases linearly with ω_r .

The above formula has been determined empirically by trial and error: different values of σ have been used for each frequency and the radiating sound field has been compared to the original sound field; the values of σ that give satisfactory results for the radiating frequencies $\omega_r = 1.0, 1.2$ and 3.4 follow equation (4.14). Whether that formula holds for a wider range of frequencies or in other flows is unknown.

Note that the amplitude of the computed sound sources depends on the fil-

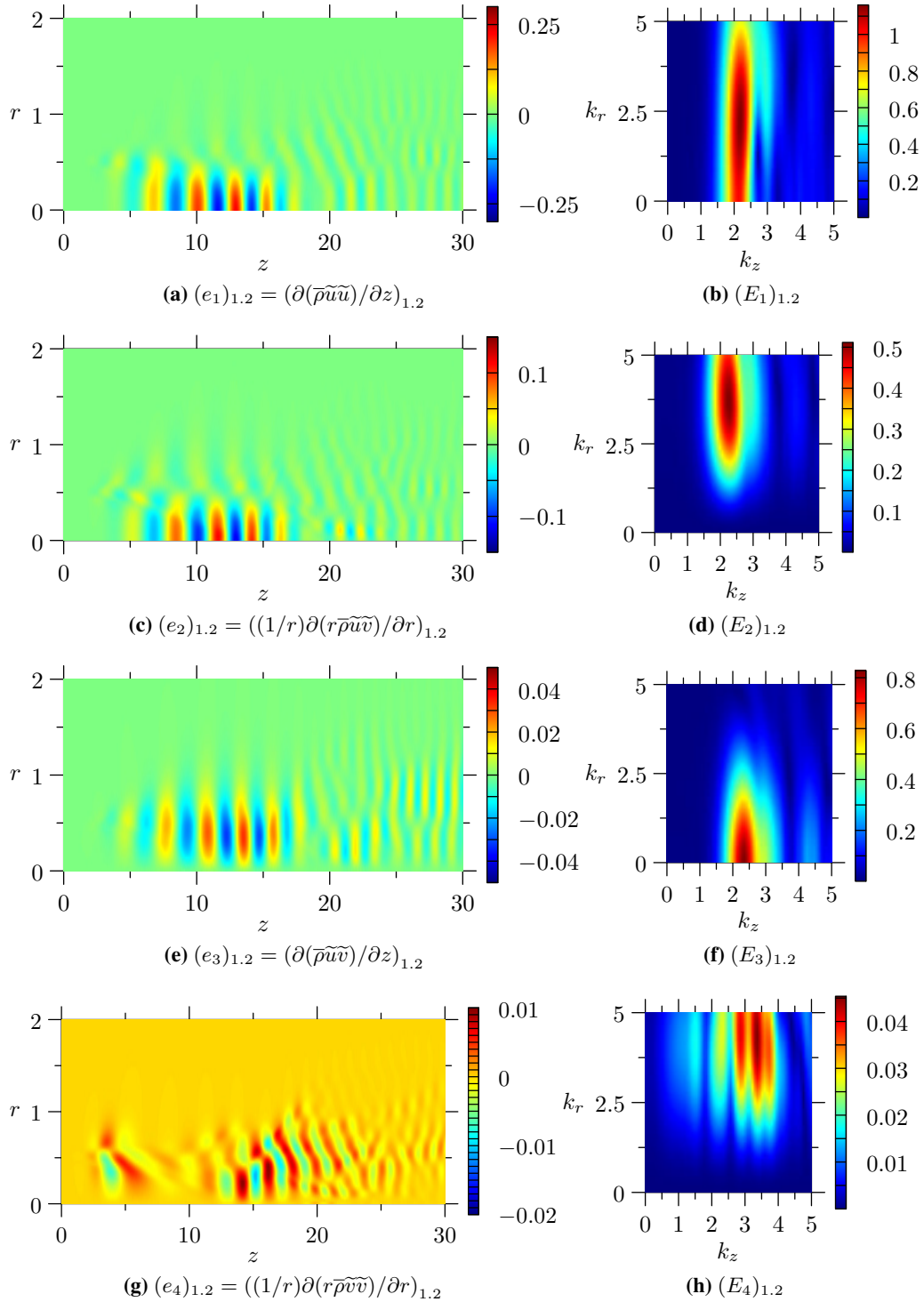


Figure 4.17 – Components of source vector $(e)_{1.2}$ at frequency 1.2 and time $t = 157.18$, in the space domain (left column) and wavenumber domain (right column).

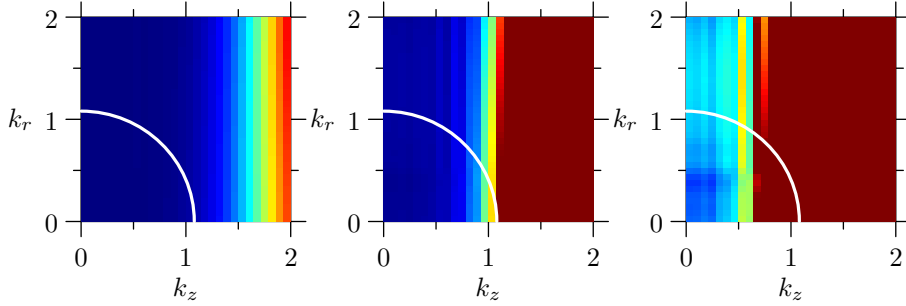


Figure 4.18 – Components of source vector $(\mathbf{e})_{1,2}$ at frequency 1.2 and time $t = 157.18$, in the wavenumber domain (right column) for decreasing contour levels: from left to right, the maximum contour levels are 1.15, 0.055 and 0.0055. In all cases, the minimum contour levels is 0.

ter width σ . Figure 4.18 displays the first component of source vector $(\mathbf{e})_{1,2}$ in the Fourier domain, with decreasing contour levels. There is no obvious separation between the radiating and non-radiating components: the amplitude decreases gradually with k_z . Therefore, the energy of the radiating components of $(\mathbf{e})_{1,2}$ in the wavenumber domain is a function of the filter width σ . From Parseval's theorem, the energy of the radiating components in the space–time domain is also a function of the filter width σ . This is a drawback of the present methodology. Nevertheless, the structure of these radiating components in the space–time domain appears not to be sensitive to the filter width: the width mostly affects the amplitude of the sound sources.

Radiating term \mathbf{e}' in the wavenumber domain

Let \mathbf{E} denote the spatial Fourier transform of \mathbf{e} . The components of $(\mathbf{E})'_{1,2}$ in the wavenumber domain are shown in the right column of figure 4.19. The dominant radiating term is found to be $(E_1)'_{1,2}$, followed by $(E_3)'_{1,2}$ (peak is 3 times smaller). The remaining terms, $(E_2)'_{1,2}$ and $(E_4)'_{1,2}$ are weaker by two orders of magnitude. Moreover, it can be seen from 4.19(b) and 4.19(f) that $(E_1)'_{1,2}$ and $(E_3)'_{1,2}$ contain radiating components that are directed at angles close to the jet axis (less than 45 deg). On the contrary, from 4.19(d) and 4.19(h), $(E_2)'_{1,2}$ ($E_4)'_{1,2}$ contain radiating components directed away from the jet axis (more than 20 deg for $(E_2)'_{1,2}$ and more than 45 deg for $(E_4)'_{1,2}$). This might explain the presence of a side lobe in the directivity of figure 4.4(b).

Radiating term \mathbf{e}' in the space domain

The components of $(\mathbf{e})'_{1,2}$ in the space domain are shown in the left column of figure 4.19 for $z \leq 30$. Note that spurious sources can appear close to the

outflow boundary ($z \geq 35$). These spurious sources can be removed by means of a smooth windowing function. Once again, the dominant terms are $(e_1)'_{1.2}$ and $(e_3)'_{1.2}$. This explains why most of the acoustic waves present in the jet are radiating at angles close to the jet axis (less than 45 deg), as shown in figure 4.4(a). The structure varies between each component. The term $(e_1)'_{1.2}$ takes the form of a wave packet distributed along the jet axis for $0 \leq z \leq 15$ and $0 \leq r \leq 4$. The term $(e_3)'_{1.2}$ is similar but vanishes as r goes to zero. The remaining fields, $(e_2)'_{1.2}$ and $(e_4)'_{1.2}$ are two orders of magnitude weaker than $(e_1)'_{1.2}$. Both $(e_2)'_{1.2}$ and $(e_4)'_{1.2}$ are centered around the end of the potential core ($r \approx 6$) but $(e_2)'_{1.2}$ is concentrated within the jet for ($r \leq 2$) whereas $(e_4)'_{1.2}$ is maximum outside the jet shear layer for $0.5 \leq r \leq 4$.

NRBF sources

The NRBF sources at frequency 1.2, defined in equations (4.11) and (4.13), are presented in figure 4.20. The first row of the figure shows a pseudo colour plot of the axial source $(f_{1z})_{1.2}$ as well as profiles along $r = 0, 1.5$, and 3 , and along $z = 6.7$, which corresponds to the value of z for which $(f_{1z})_{1.2}$ reaches its maximum. The second row of figure 4.20 shows the radial source $(f_{1r})_{1.2}$ as well as profiles along $r = 1, 2$, and 3 , and along $z = 2.4$, which corresponds to the value of z for which $(f_{1r})_{1.2}$ reaches its maximum.

The axial profiles (figures 4.20(b) and 4.20(c)) suggest that the NRBF sources take the form of wave packets. For $(f_{1z})_{1.2}$, the wave packet reaches its maximum amplitude at the end of the potential core. For $(f_{1r})_{1.2}$, the peak is situated upstream of the potential core, close to the inlet, and outside of the jet shear layer around $r = 2$.

The evolution of $(f_{1z})_{1.2}$ is as follows. The envelope of the wave packet remains fixed (see figure 4.21(a)) while the waves are travelling at the phase velocity $u_z = 1.06$. This velocity has been estimated by following the peak lobe between for $6 \leq z \leq 12$ over an entire period (see profiles in figure 4.21(b)). The position of the peak lobe for 5 successive time frames equally distributed over a period $T_{1.2} = 50\Delta t$ is shown in table 4.6. A linear regression based on these values indicates that $u_z = 1.06$. This value is subsonic but is greater than the jet exit velocity.

Results at frequencies 1.0 and 2.2

Similar results have been obtained at the two other radiating frequencies $\omega_r = 1.0$ and 2.2 . The figures representing $(\mathbf{e}')_{\omega_r}$ in the space and wavenumber domains, as well as the NRBF sources $(f_{1z})_{\omega_r}$ and $(f_{1r})_{\omega_r}$, are presented

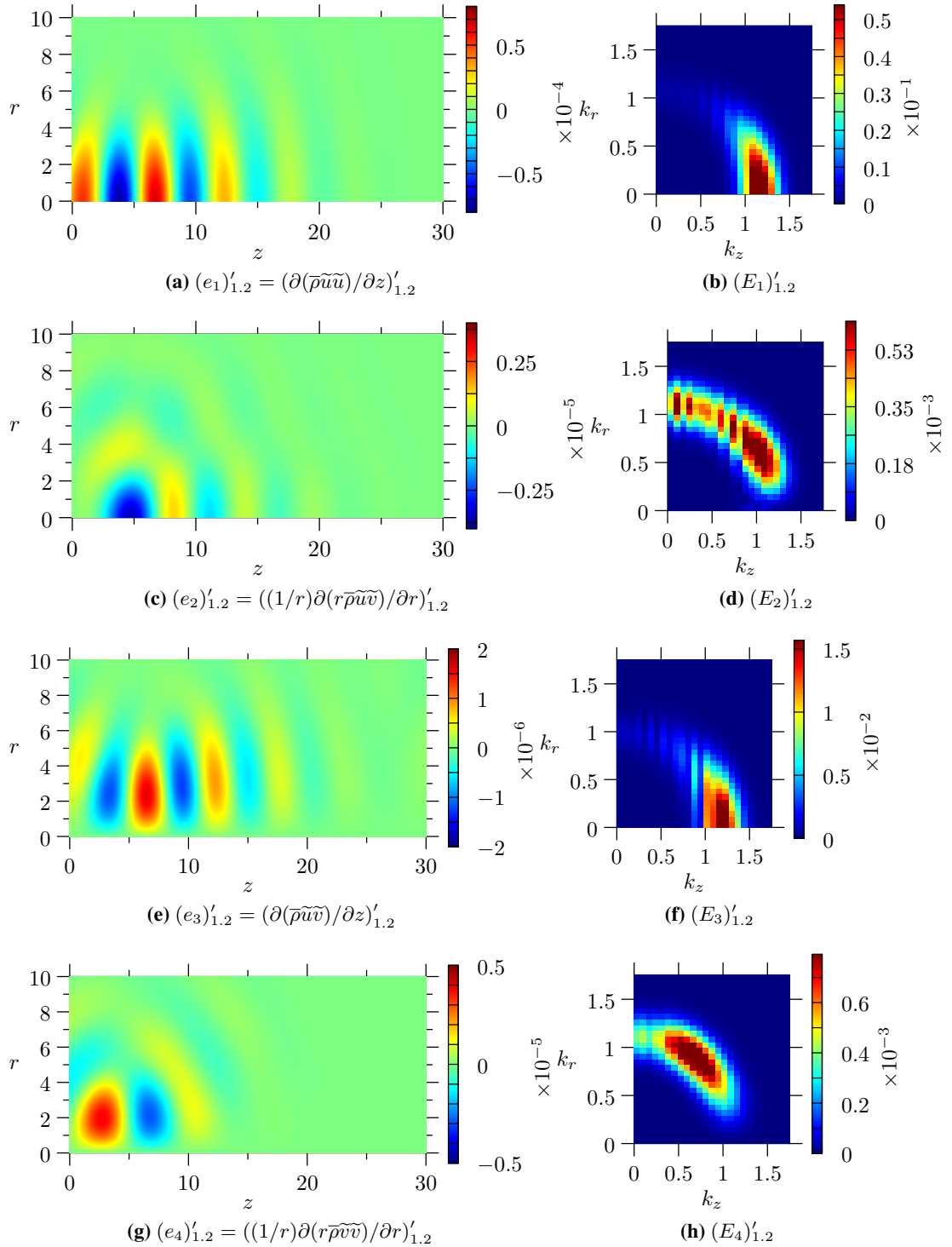


Figure 4.19 – Components of radiating source vector $(\mathbf{e}')_{1.2}$ at frequency 1.2 and time $t = 157.18$, in the space domain (left column) and wavenumber domain (right column).

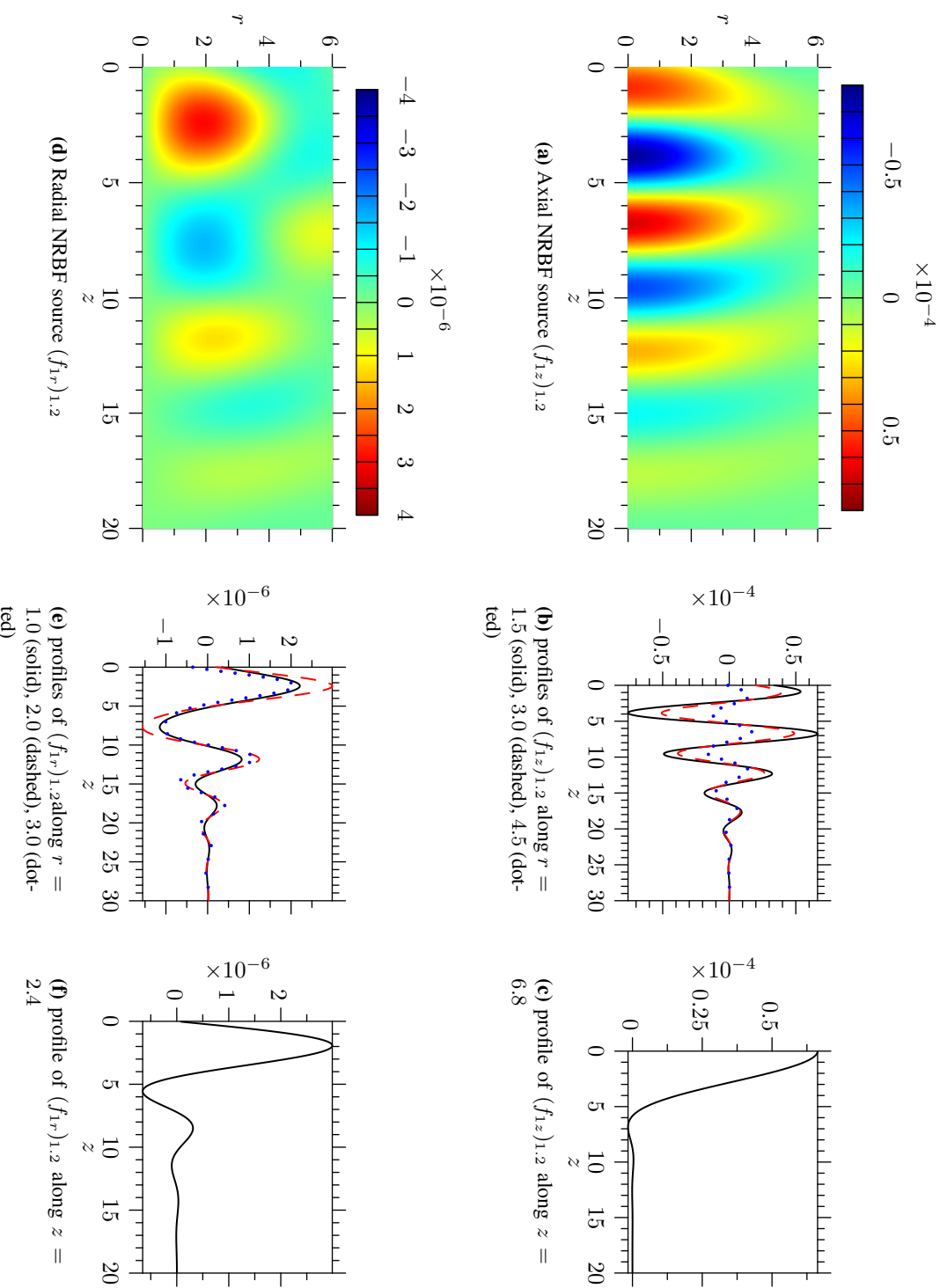


Figure 4.20 – NURBF sources $(f_{1z})_{1,2}$ and $(f_{1r})_{1,2}$ at frequency 1.2 and time $t = 157.18$.

$t/\Delta t$	z_{peak}
0	6.77
10	7.91
20	9.01
30	10.11
40	11.1

Table 4.6 – Successive positions of the peak lobe of $(f_{1z})_{1.2}$, along the z -axis, for $6 \leq z \leq 12$.

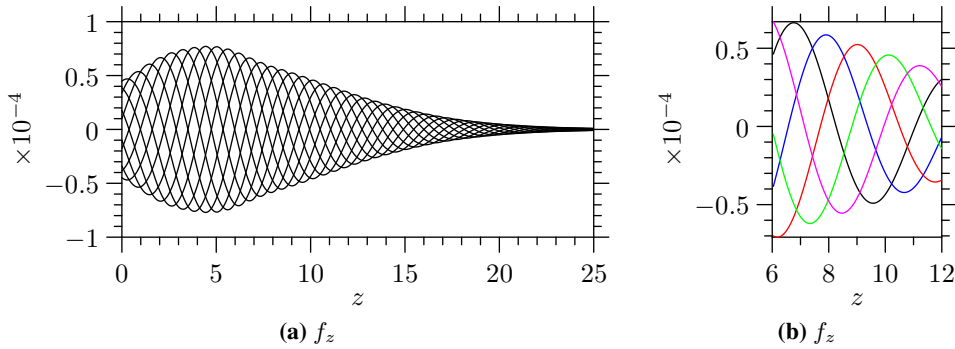


Figure 4.21 – Evolution of the NRBF source $(f_{1z})_{1.2}$ with time along $r = 0$. In (a), $(f_{1z})_{1.2}$ is plotted every $5\Delta t$. In (b), $(f_{1z})_{1.2}$ is plotted every $10\Delta t$.

in appendix in figures B.14 to B.17.

4.4.3 Amplitude and location of the sound sources

From the momentum equation (2.24), the magnitude of the NRBF source $(f_{1z})_{1.2}$ should be similar to that of $(\rho u)'_{1.2}$. It can be seen that this is indeed the case since the peak value of $(\rho u)'_{1.2}$ along $r = 0$ at $t = 157.18$ is equal to 4×10^{-4} , whereas the corresponding value is 0.7×10^{-4} for $(f_{1z})_{1.2}$ (from figure 4.20(b)).

Most importantly, the NRBF sources f_{1z} and f_{1r} are very different from the terms in e . They have much smaller amplitude and their peak locations are different. Comparing figure 4.17(a) with figure 4.20(a), for example, $(e_1)_{1.2}$ is maximum for $z > 10$, whereas $(f_{1z})'_{1.2}$ is maximum for $z \approx 5$ and vanishes for $z \geq 10$. This illustrates the danger in trying to localize the sound sources by examining non-radiating variables.

4.4.4 Validation

Governing equations and implementation

Validating the NRBF sources requires to compute the sound they generate and let it propagate to the far field within the non-radiating base flow. This

requires to solve equations (2.23), (2.24) and (2.25). These equations are difficult to solve as they require to filter out the non-radiating components generated by the propagation terms. However, as a first approximation and as shown in section 2.1.4, the governing equations can be approximated by the Euler equations linearized about the time-averaged base flow. The full system of equations is given below:

$$\frac{\partial \rho'}{\partial t} + \frac{\partial}{\partial x_j} (\rho v_j)' = 0, \quad (4.15)$$

$$\frac{\partial}{\partial t} (\rho v_i)' + \frac{\partial}{\partial x_j} (\widehat{v}_j(\rho v_i)' + \widehat{v}_i(\rho v_j)' - \widehat{v}_i \widehat{v}_j \rho' + \gamma \delta_{ij} \pi_0^{\gamma-1} \pi') = f_{1i}, \quad (4.16)$$

$$\frac{\partial \pi'}{\partial t} + \frac{\partial}{\partial x_j} \left[\frac{\pi_0}{\rho_0} ((\rho v_j)' - \widehat{v}_j \rho') + \widehat{v}_j \pi' \right] = 0, \quad (4.17)$$

where the terms of the form \widehat{v}_i represent Favre averaged mean velocities and δ_{ij} denotes the Kronecker delta, which is equal to 1 if i is equal to j and 0 otherwise.

An explicit time marching Linearized Euler Equations (LEE) solver is used to propagate the NRBF sources to the far field. This is done separately for each frequency. The sound sources are constructed at every time step, from the value of the real and imaginary parts of the source Fourier transform at the frequency of interest, by using equation (4.5).

The solver is axisymmetric and utilizes the conservation form of the linearized Euler equations. The partial derivatives are carried out using the Dispersion Relation Preserving scheme of Tam and Webb [55]. A filter is used to smooth out grid to grid oscillations. The solution is marched in time using an optimized 2-storage 6-stage Runge-Kutta scheme by Bogey and Bailly [56].

Results and discussion

The modified pressure $\pi - \pi_0$ radiated from the NRBF sources $(f_{1z})_{1.2}$ and $(f_{1r})_{1.2}$ using the LEE solver is compared in figure 4.22 to the DNS solution $\pi_{1.2}$. Figures 4.22(a) and 4.22(b) show pseudo colour plots of $\pi - \pi_0$ (from LEE) and $\pi_{1.2}$ (from DNS) respectively. These figures show qualitatively that the sound radiating from the NRBF sources at frequency 1.2 is in good agreement with the original sound field from the DNS at that frequency. In figures 4.22(c) and 4.22(d) profiles of $\pi - \pi_0$ (gray) and $\pi_{1.2}$ (black) are shown along $r = 10$ and $r = 20$. In each case, the two profiles are in good agreement. Similar results are presented for the modified pressure field at the radiating frequencies 1.0 and 2.2, as shown in appendix in figures B.18

and B.19. Similar plots are presented for the other flow variables at frequency 1.2, 1.0 and 2.2 in figures B.20, B.21 and B.22.

Most importantly, the radiating modified pressure field is free of any hydrodynamic component, as can be seen in figure 4.22(b). This suggests that sources $(f_{1z})_{1.2}$ and $(f_{1r})_{1.2}$ are true sources of sound. Note however that some (small) hydrodynamic components are visible on the radiating momentum and density variables $\rho u - (\rho u)_0$, $\rho v - (\rho v)_0$, and $\rho - \rho_0$ of figure B.20. This is because of the introduction, on the left hand side of the LEE equations, of some non-radiating wavenumbers which should normally be filtered out. For example, in the exact formulation of (2.24), the term $(\tilde{u}(\rho u)')'$ is free of non-radiating components, whereas it is approximated in the present implementation by $\hat{u}(\rho u)'$, which does contain some non-radiating components. Interestingly, these small hydrodynamic components do not contaminate the modified pressure field.

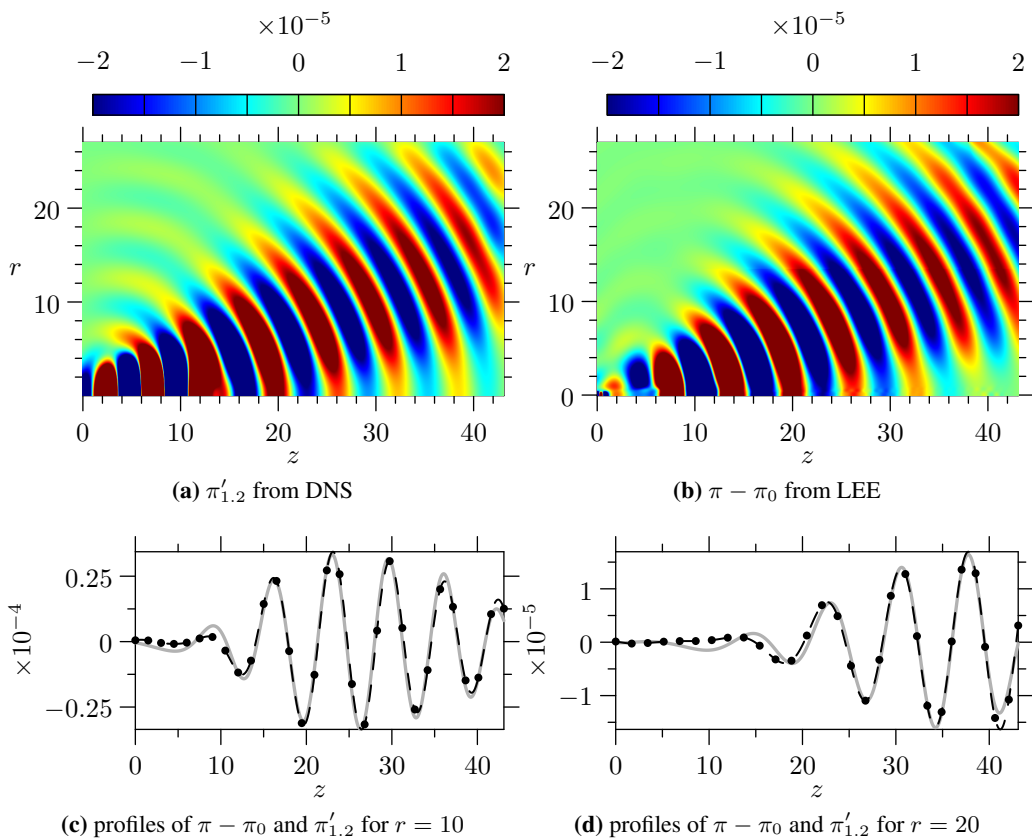


Figure 4.22 – Comparison of the modified pressure field $\pi - \pi_0$, obtained by driving the LEE with the NRBF sources $(f_{1z})_{1.2}$ and $(f_{1r})_{1.2}$, with the radiating modified pressure field $\pi'_{1.2}$ at frequency 1.2. The bottom figures give profiles along $r = 10$ and $r = 20$: the gray line represents the DNS solution ($\pi_{1.2}$) and the dashed black line with black circles the LEE solution ($\pi - \pi_0$).

4.4.5 Dominant source term

For each radiating frequency ω_r , the NRBF sources are composed of two terms, $(f_{1z})_{\omega_r}$ and $(f_{1z})_{\omega_r}$, each of which takes the form of the divergence of a vector. The NRBF sources are therefore made of multiple terms. In this section, the dominant terms are determined by computing the amount of sound generated by each term individually.

The modified pressure field radiating from each of the terms that compose $(f_{1z})_{1.2}$ and $(f_{1z})_{1.2}$ is obtained by using the LEE solver described in section 4.4.4. The results are shown in figure 4.23. Clearly, the axial term $e_1 = \partial(\bar{\rho}\tilde{u}\tilde{u})'_{1.2}/\partial z$ is responsible for most of the sound generation. The contribution of the cross terms, $e_2 = (1/r)\partial(r\bar{\rho}\tilde{u}\tilde{v})'_{1.2}/\partial r$ and $e_3 = \partial(\bar{\rho}\tilde{v}\tilde{v})'_{1.2}/\partial z$, to $\pi_{1.2}$ is negligible. Finally, the radial term $e_4 = (1/r)\partial(r\bar{\rho}\tilde{v}\tilde{v})'_{1.2}/\partial r$ is a significant sound radiator away from the jet axis.

The directivity of the sound radiating from the two dominant source terms is presented in figure 4.24. It is based on the power of the modified pressure field $\pi_{1.2}$ at a distance $R = 20$, using 90 time snapshots over 18 periods. Figure 4.24(a) presents the directivity of the power of the modified pressure field $\pi_{1.2}$ radiating from $(e_1)'_{1.2}$ and $(e_4)'_{1.2}$, where the power has been normalized so that the peak directivity of the DNS solution is 60dB. Figure 4.24 shows that the sound generated by $(e_1)'_{1.2}$ is maximum towards 20° and decays relatively rapidly for larger angles (the magnitude is at least 15dB lower than the peak value for angles larger than 45°). The directivity of the sound radiating from $(e_4)'_{1.2}$ is maximum towards 45° and decays slowly away from that direction (the magnitude decreases by less than 5dB for angles between 30° and 65°). However, as shown in figure 4.24(b), $(e_4)'_{1.2}$ is a much weaker sound source than $(e_1)'_{1.2}$: for angles lower than 40° , the sound radiating from $(e_4)'_{1.2}$ is at least 15dB lower than that radiating from $(e_1)'_{1.2}$. However, the contribution of $(e_4)'_{1.2}$ to the overall modified pressure field increases for larger angles and becomes dominant for angles higher than 60° . Towards 80° , sound radiating from $(e_4)'_{1.2}$ is stronger than sound radiating from $(e_1)'_{1.2}$ by more than 10dB. Note that the directivity based on $(e_1)'_{1.2}$ and $(e_4)'_{1.2}$ is in good agreement with the DNS solution for angles up to 55° but is underestimated for larger angles. This might be due to inaccuracies in the computation of $(e_4)'_{1.2}$, or to errors in the propagation of sound from $(e_4)'_{1.2}$.

In conclusion, the dominant source mechanism in this flow is an axial momentum source term equal to the radiating part of $\partial(\bar{\rho}\tilde{u}\tilde{u})/\partial z$. This term generates significant sound for angles close to the jet axis (less than 45°). In addition, the radiating part of $(1/r)\partial(r\bar{\rho}\tilde{v}\tilde{v})/\partial r$ also generates significant

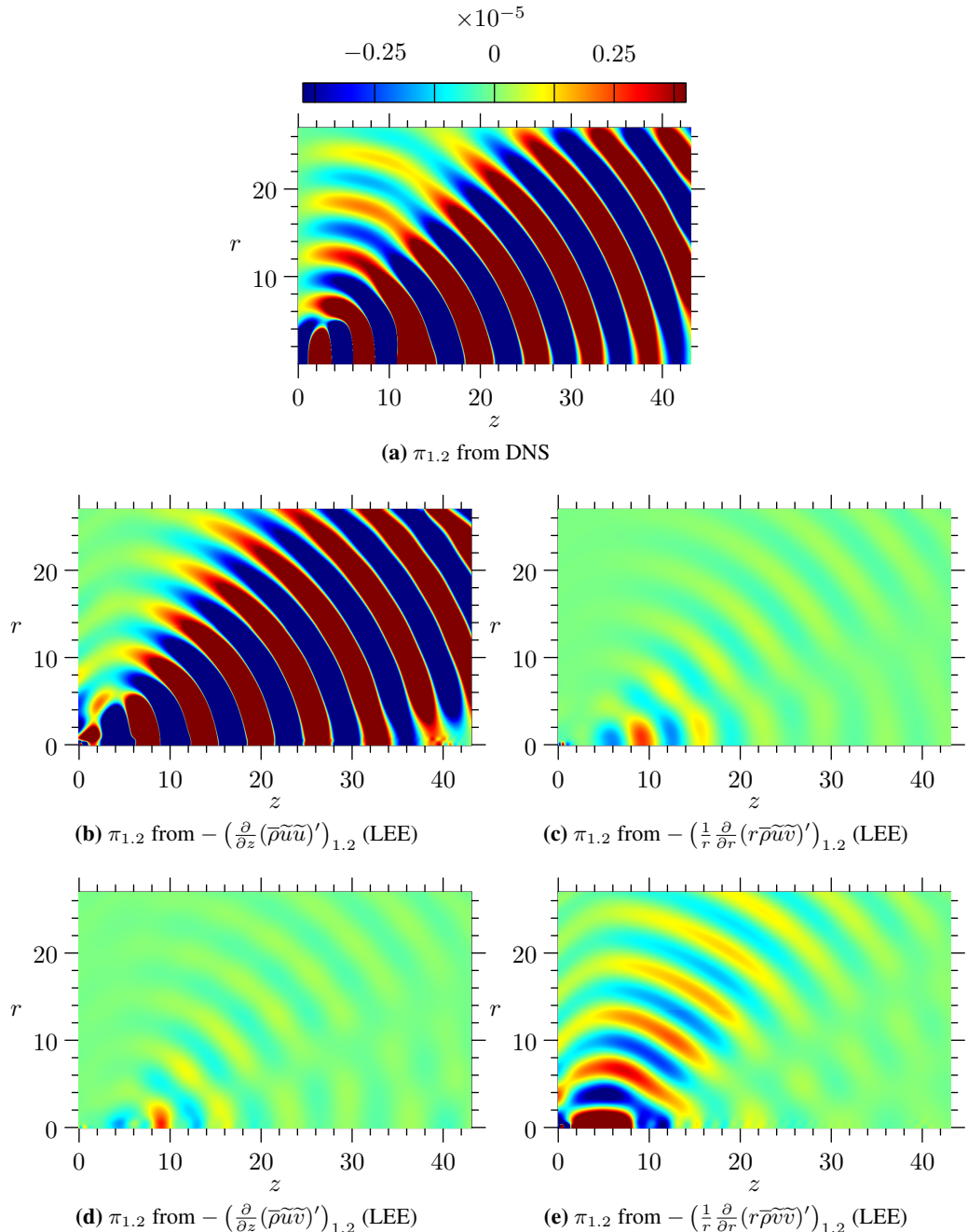
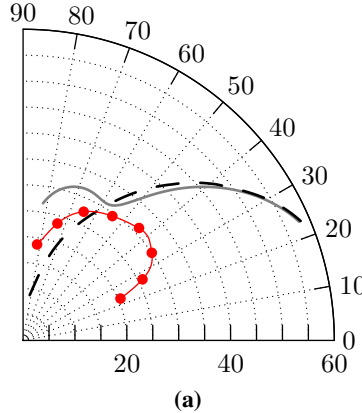


Figure 4.23 – Snapshots of the modified pressure field radiating from the source terms that compose the NRBF sources $(f_{1z})_{1,2}$ and $(f_{1r})_{1,2}$, compared to the DNS solution $\pi_{1,2}$.



(a)

Figure 4.24 – Directivity of the modified pressure field $\pi_{1.2}$ radiating from $(e_1)'_{1.2} = \partial(\bar{p}\bar{u}\bar{u})'_{1.2}/\partial z$ (black dashed line) and $(e_4)'_{1.2} = (1/r)\partial(r\bar{p}\bar{v}\bar{v})'_{1.2}$ (red line with filled circles), compared to the directivity of the DNS solution (gray line). The directivities are normalized by 2.44×10^{-7} .

sound, but mostly for large angles (more than 45°). The other source terms have been found to be negligible.

4.5 Effect of the size of the computational domain

In section 4.4 a large computational domain has been used: $0 \leq z \leq 43.1$ and $0.02 \leq r \leq 27$. This was done to include, in addition to the near field, part of the far field to the computational domain. It helped validate the decomposition of the flow into radiating and non-radiating components. Large domains also lead to an increased resolution of the Fourier and Hankel transforms (see section 3.4.2). However, for three dimensional flows, it becomes very expensive to use large computational domain. This difficulty would be mitigated if the NRBF sources can be computed based on smaller computational domains. There is a need to understand how well the method performs for smaller computational domains. This problem is treated in the following section.

4.5.1 Algorithm

The algorithm defined in section 4.4.1 is implemented to compute the NRBF sources for different sizes of the computational domain by varying the dimensions r_{\max} and z_{\max} of the domain ($r_{\min} = z_{\min} = 0$). The sound sources are found to be unchanged for $r_{\max} \geq 20$ and $z_{\max} \geq 30$. However, the magnitude of the NRBF sources diminishes slightly as r_{\max} and z_{\max} decrease below these values. Equation (4.14) is modified to correct this variation in

amplitude:

$$\sigma(\omega) = \frac{1}{7.5}(1 + \epsilon_r + \epsilon_z)\frac{\omega}{c_\infty}, \quad (4.18)$$

where

$$\epsilon_r = 1.5 \times 10^{-2} \left(\frac{r_\infty}{r_{\max}} \right)^2, \quad \epsilon_z = 1.5 \times 10^{-2} \left(\frac{z_\infty}{z_{\max}} \right)^2, \quad (4.19)$$

$r_\infty = 20$ and $z_\infty = 30$. As r_{\max} and z_{\max} tend to ∞ , σ tends to the expression of equation (4.14). Besides, for $r_{\max} \geq r_\infty$ and $z_{\max} \geq z_\infty$, $\epsilon_r + \epsilon_z \leq 3 \times 10^{-2}$ which corresponds to an increase in σ of less than 3% compared to the value of equation (4.14).

The need for this modification can be explained by the sensitivity of the NRBF sources to the value of σ . Equation (4.14) was obtained empirically, using the full computational domain ($r_{\max} = 27$ and $z_{\max} = 43$), by comparing the amplitude of the sound radiated by the sources with the amplitude of the sound in the DNS solution (section 4.4.4). Similarly, equation (4.18) is defined empirically so that the amplitude of the sound sources based on smaller computational domains matches the amplitude of the sources computed (and validated) for the full domain. The question is to know whether satisfactory results can be obtained for smaller domains.

4.5.2 NRBF sources for smaller domains in the radial direction

The value of z_{\max} is fixed to 43 and the size of the domain is changed by varying r_{\max} . Figure 4.25 shows the NRBF sources at frequency 1.2 for $r_{\max} = 20, 12, 6$ and 3. Each row gives pseudo-colour plots and profiles of the axial and radial sources $(f_{1z})_{1.2}$ and $(f_{1r})_{1.2}$ for one particular value of r_{\max} . The profiles are given along $r = 0$ for $(f_{1z})_{1.2}$ and $r = 2$ for $(f_{1r})_{1.2}$, which correspond to the line where these sources reach their maximum. The profiles are plotted using black dashed lines, against the full domain solution of figure 4.20 (for which $r_{\max} = 27$, $z_{\max} = 43$), which is plotted in gray.

The top two rows of figure 4.25 suggest that the NRBF sources can be computed with great accuracy for $r_{\max} \geq 12$. Agreement between the sources based on the full domain and those based on the smaller domain remains very good even for $r = 6$ (third row), although small changes in the radial part of the source become noticeable. Interestingly, agreement remains reasonable qualitatively even for $r = 3$ (bottom row). These results suggest that in this case, the computation of the NRBF sources is not very sensitive to r_{\max} , and that the sources can be obtained with good accuracy even for $r_{\max} = 6$. That

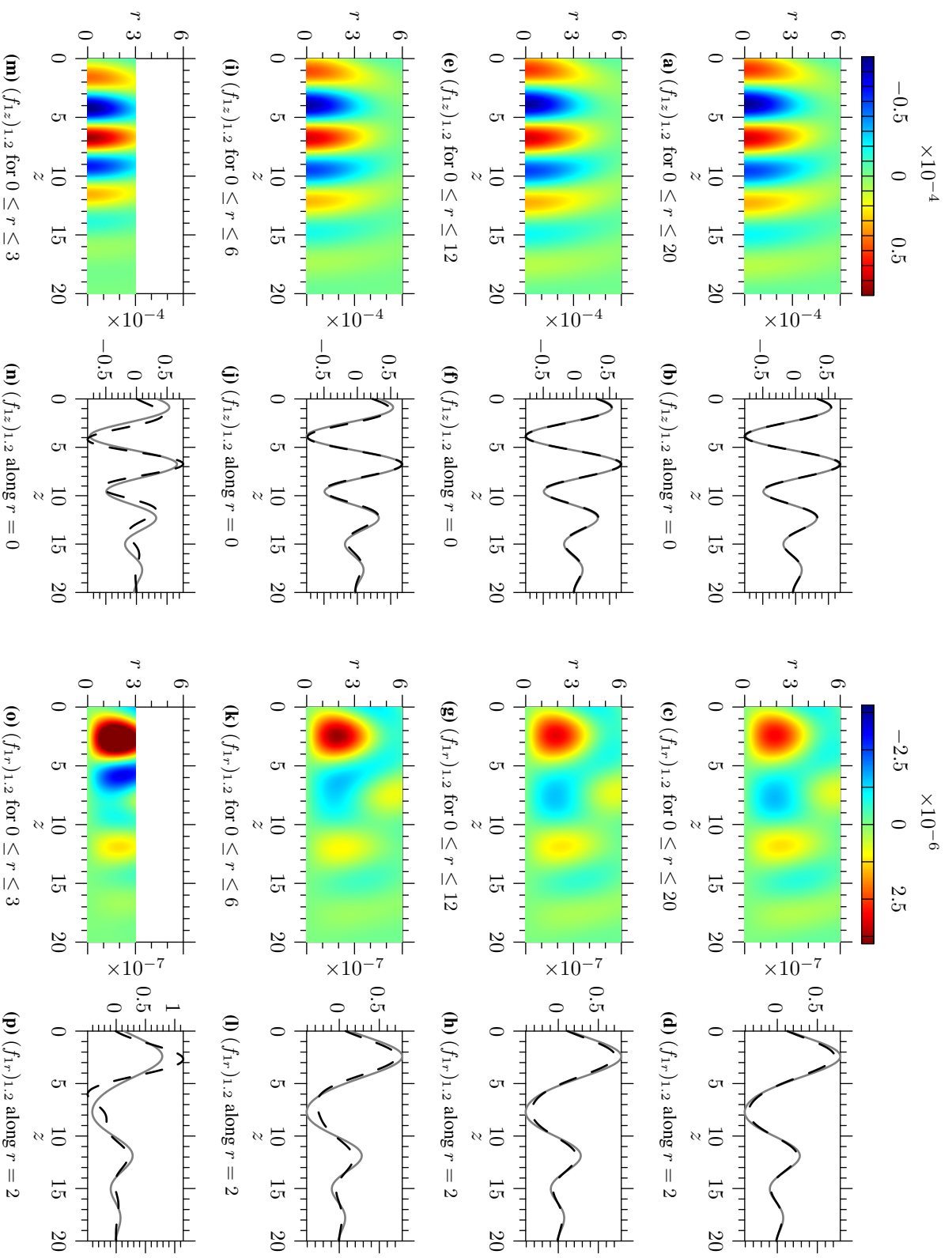


Figure 4.25 – NRBf sources $(f_{1z})_{1,2}$ (columns 1 and 2) and $(f_{1r})_{1,2}$ (columns 3 and 4) at frequency 1.2 and time $t = 157.18$ for different size of the computational domain in the r -direction (from top to bottom, $r_{\max} = 20, 12, 6$ and 3). In all subfigures, the computational domain is fixed in the axial direction to $0 \leq z \leq 43$. The profiles are given along $r = 0$ for $(f_{1z})_{1,2}$ and $r = 2.0$ for $(f_{1r})_{1,2}$: the gray line represents the source obtained for the full domain of section 2.1.2 and the black dashed line represents the source obtained for the smaller domain.

value corresponds approximately to one acoustic wavelength ($\lambda_{1.2} = 5.8$), which leads to a spectral resolution of $\Delta k_r = 2\pi/\lambda_{1.2} = |\mathbf{k}_\infty|$: in this case, it is sufficient to discretize the radiation circle in the wavenumber domain by using only one point in the radial direction.

4.5.3 NRBF sources for smaller domains in the axial direction

The value of r_{\max} is fixed to 27 and the size of the domain is changed by varying z_{\max} . Figure 4.26 shows the NRBF sources at frequency 1.2 for $z_{\max} = 30, 20, 12$ and 8. Each row gives pseudo-colour plots and profiles of the axial and radial sources $(f_{1z})_{1.2}$ and $(f_{1r})_{1.2}$ for one particular value of z_{\max} . The profiles are given along $r = 0$ for $(f_{1z})_{1.2}$ and $r = 2$ for $(f_{1r})_{1.2}$, which correspond to the line where these sources reach their maximum. The profiles are plotted using black dashed lines, against the full domain solution of figure 4.20 (for which $r_{\max} = 27, z_{\max} = 43$), which is plotted in gray.

The top row of figure 4.25 shows that the NRBF sources can be computed with great accuracy for $z_{\max} = 30$. Agreement between the sources based on the full domain and those based on the smaller domain remains very good down to $z_{\max} = 20$ (second row). For $z_{\max} = 12$, the agreement is reasonable qualitatively for the axial source, but not for the radial source. For even smaller values of z_{\max} , such as $z_{\max} = 8$, the agreement becomes very poor. These results suggest that the NRBF sources can be obtained with good accuracy for $z_{\max} \geq 20$. That value corresponds approximately to 3 acoustic wavelength ($\lambda_{1.2} = 5.8$), which leads to a spectral resolution of $\Delta k_z = 2\pi/3\lambda_{1.2} = |\mathbf{k}_\infty|/3$. The value $|\mathbf{k}_\infty|/3$ implies that the convection velocity u_c of the non-radiating components which are closest to the radiation circle is 0.67.

4.5.4 NRBF sources for smaller domains in both directions

Figure 4.27 presents the NRBF sources for $r_{\max} = 6$ and $z_{\max} = 20$. It shows that they are in good agreement with the sources based on the full computational domain ($r_{\max} = 27, z_{\max} = 43$). The domain defined by $r_{\max} = 6$ and $z_{\max} = 20$ captures only part of the near field but is sufficient to compute the NRBF sources.

The results presented in this section indicate that the NRBF sources can be obtained with good accuracy by using only the near flow field. The size of the computational domain corresponds to only one wavelength in the radial direction and 3.5 wavelength in the axial direction. Although these values might be problem dependent, they can be used as guidelines to estimate the minimum

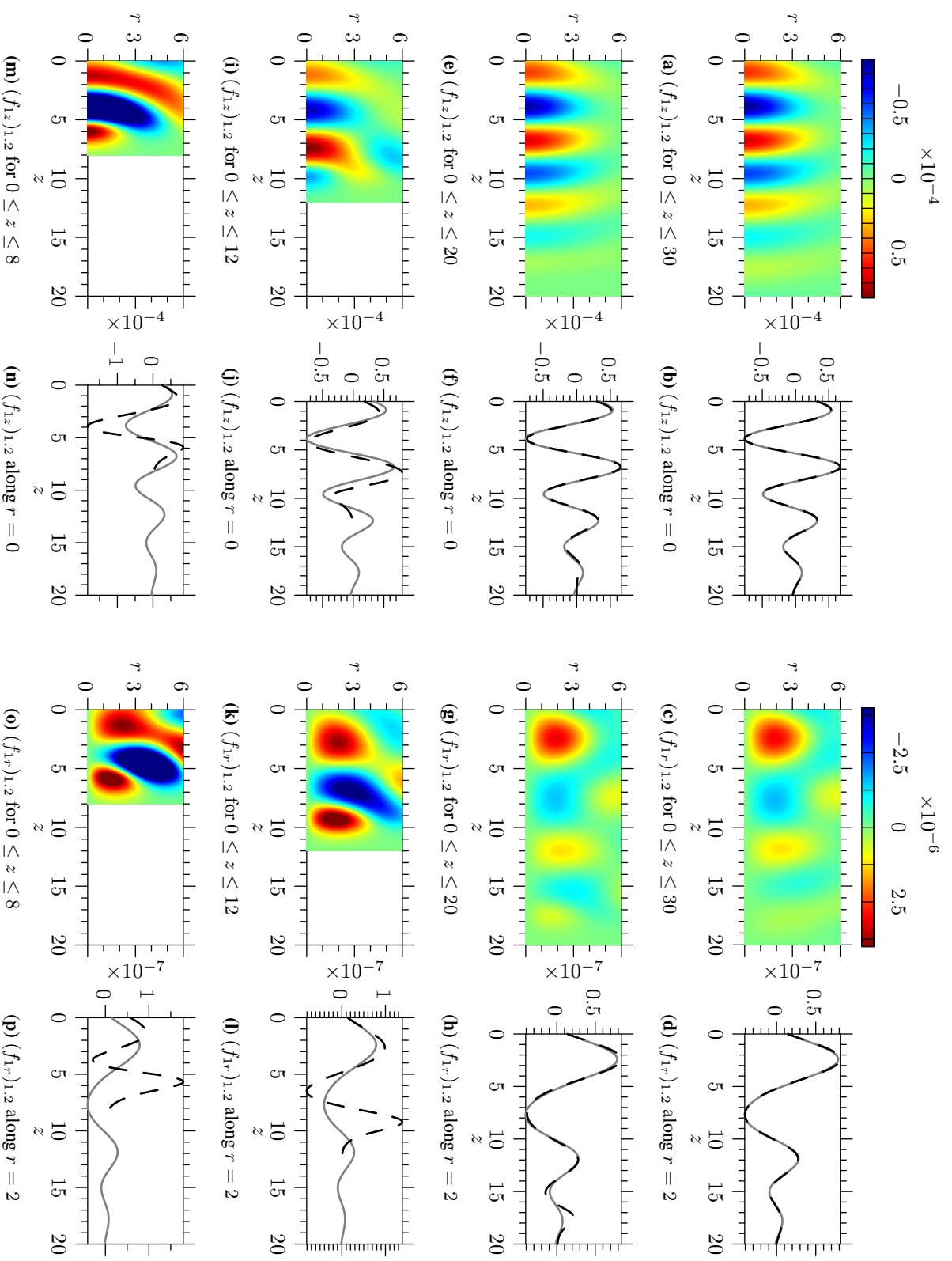


Figure 4.26 – NRBf sources $(f_{1z})_{1,2}$ (columns 1 and 2) and $(f_{1r})_{1,2}$ (columns 3 and 4) at frequency 1.2 and time $t = 157.18$ for different size of the computational domain in the axial direction (from top to bottom, $z_{\max} = 30, 20, 12$ and 8). In all subfigures, the computational domain is fixed in the radial direction to $0 \leq r \leq 27$. The profiles are given along $r = 0$ for $(f_{1z})_{1,2}$ and $r = 2.0$ for $(f_{1r})_{1,2}$; the gray line represents the source obtained for the full domain of section 2.1.2 and the black dashed line represents the source obtained for the smaller domain.

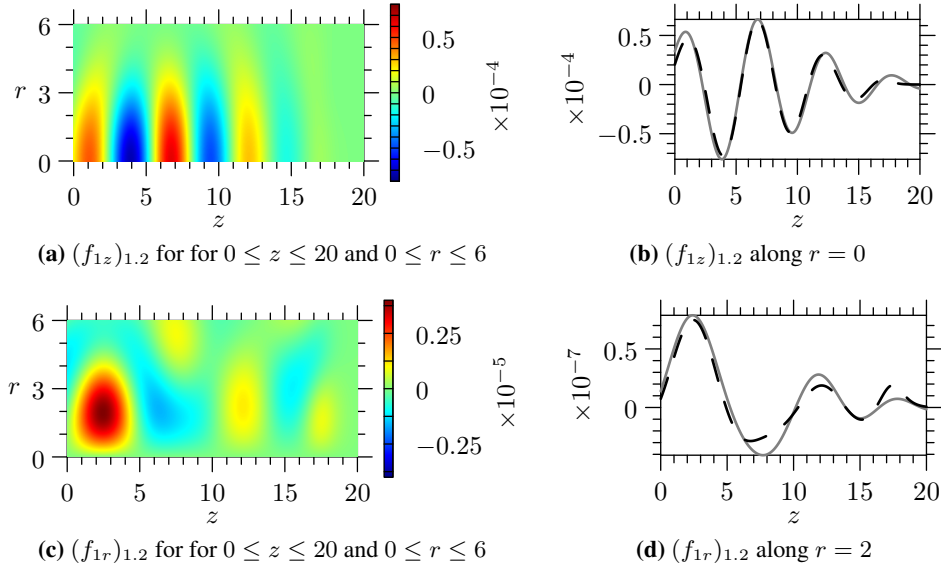


Figure 4.27 – NRBF sources $(f_{1z})_{1.2}$ and $(f_{1r})_{1.2}$ at frequency 1.2 and time $t = 157.18$ using a computational domain such that $0 \leq r \leq 6$ and $0 \leq z \leq 20$. The profiles are given along $r = 0$ for $(f_{1z})_{1.2}$ and $r = 2.0$ for $(f_{1r})_{1.2}$: the gray line represents the source obtained for the full domain of section 2.1.2 and the black dashed line represents the source obtained for the smaller domain.

size of the domain required to compute the NRBF sources. This result greatly reduces the computational requirements of the method. It suggests that the method could be applied to three dimensional flow fields.

4.6 Source based on a time-averaged base flow

In this section, the TABF sources defined in section 2.2 are computed. The TABF sources are based on an acoustic analogy in which the base flow is the time-averaged flow field. Consequently, interactions between the mean flow and the sound field are taken out of the sources, which is an improvement over both Lighthill's [1] and Lilley's analogies [35]. Nevertheless, the TABF still suffers from undesirable physical properties. This section will allow to highlight these and to better understand the advantages of the NRBF sources over classical acoustic analogies.

4.6.1 Algorithm

The algorithm used to compute the time averaged sound sources is as follows:

- compute the steady variables ρ_0 , $(\rho u)_0$, $(\rho v)_0$, π_0 ,
- compute the Favre-averaged quantities $\hat{u} = (\rho u)_0 / \rho_0$ and $\hat{v} = (\rho v)_0 / \rho_0$,

- compute the unsteady variables ρ'', u'', v'' and π'' ,
- compute the terms involved in the expression of the axial momentum source f_{2z} , i.e

$$a = -\frac{\partial}{\partial z}(\rho_0 u'' u'') - \frac{1}{r} \frac{\partial}{\partial r}(r \rho_0 u'' v'') - \frac{1}{2} \gamma(\gamma - 1) \frac{\partial}{\partial z} \pi_0^{\gamma-2} (\pi'')^2, \quad (4.20)$$

- compute the terms involved in the expression of the radial momentum source f_{2r} , i.e

$$b = -\frac{\partial}{\partial z}(\rho_0 u'' v'') - \frac{1}{r} \frac{\partial}{\partial r}(r \rho_0 v'' v'') - \gamma(\gamma - 1) \frac{1}{2r} \frac{\partial}{\partial r}(r \pi_0^{\gamma-2} (\pi'')^2), \quad (4.21)$$

- compute the TABF sources for each radiating frequency ω_r as

$$(f_{2z})_{\omega_r} = (a)_{\omega_r} \quad (4.22)$$

$$(f_{2r})_{\omega_r} = (b)_{\omega_r} \quad (4.23)$$

4.6.2 Results

The axial TABF source f_{2z} is plotted in figure 4.28(a), and $(f_{2z})_{1.2}$ is shown in figure 4.28(b). Profiles of f_{2z} and $(f_{2z})_{1.2}$ along $r = 0$ are shown in figures 4.28(c) and 4.28(d) respectively. Similarly, the radial TABF sources f_{2r} and $(f_{2r})_{1.2}$ are presented in figure 4.29, with profiles along $r = 0.25$.

The TABF sources $(f_{2z})_{1.2}$ and $(f_{2r})_{1.2}$ are used to drive the linearized Euler equations. The radiating sound field is compared to that obtained from the DNS solution in figure 4.30. A similar figure for the other flow variables is given in figure B.23.

4.6.3 Discussion

Analysis of the TABF sources

Figures 4.28(a) and Figures 4.29(a) allow to study the structure of the TABF source terms f_{2z} and f_{2r} . These terms are clearly dominated by hydrodynamic fluctuations, with bursts in amplitude throughout the shear layer and within the jet. This can be explained by examining the terms that make up the TABF sources. Each unsteady flow variable q'' can be expressed as

$$q'' = q - q_0 = \bar{q} + q' - q_0. \quad (4.24)$$

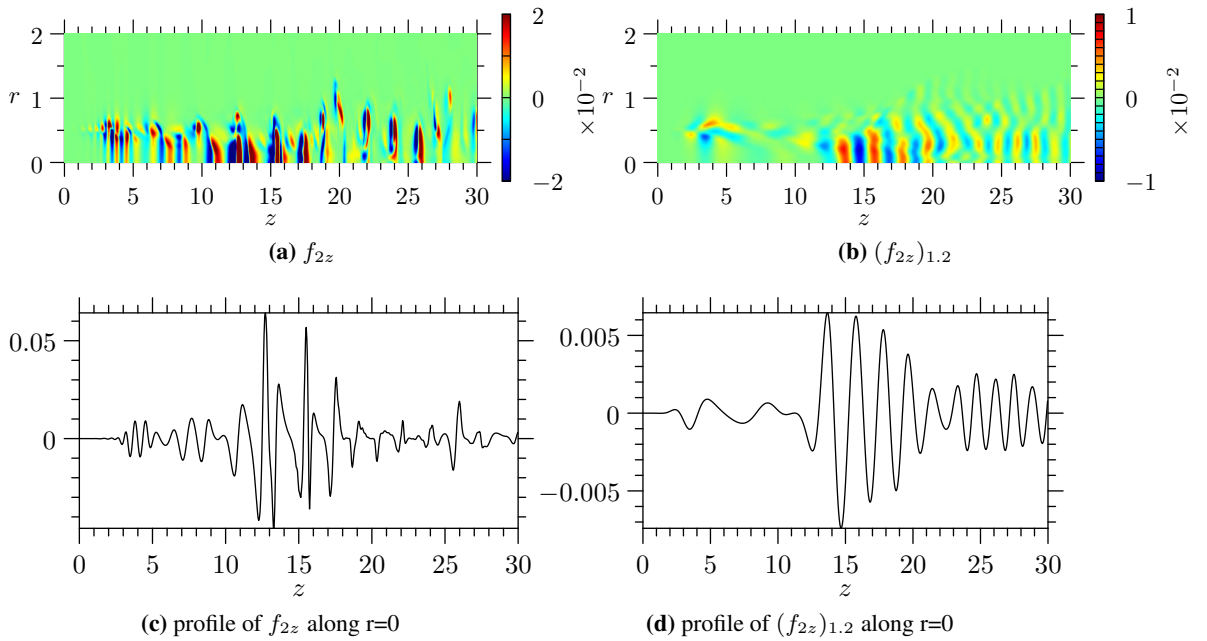


Figure 4.28 – TABF source f_{2z} in the axial direction at time $t = 157.18$, and its components $(f_{2z})_{1.2}$ at frequency 1.2. Figures (c) and (d) give profiles along $r = 0$.

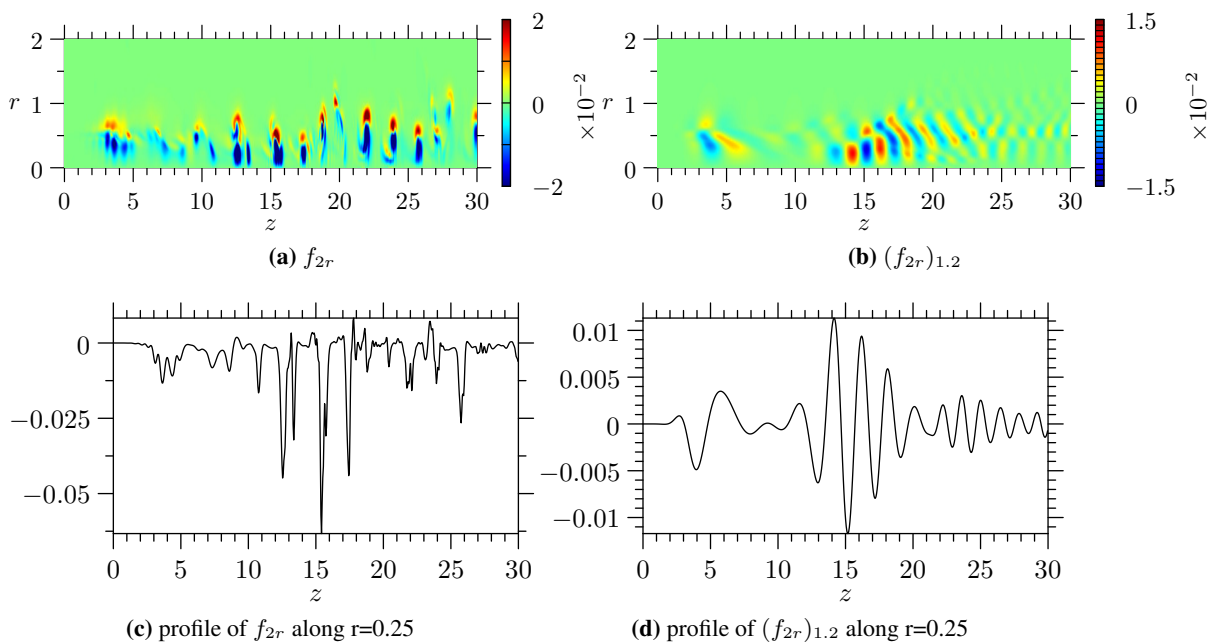


Figure 4.29 – TABF source f_{2r} in the radial direction at time $t = 157.18$, and its components $(f_{2r})_{1.2}$ at frequency 1.2. Figures (c) and (d) give profiles along $r = 0.25$.

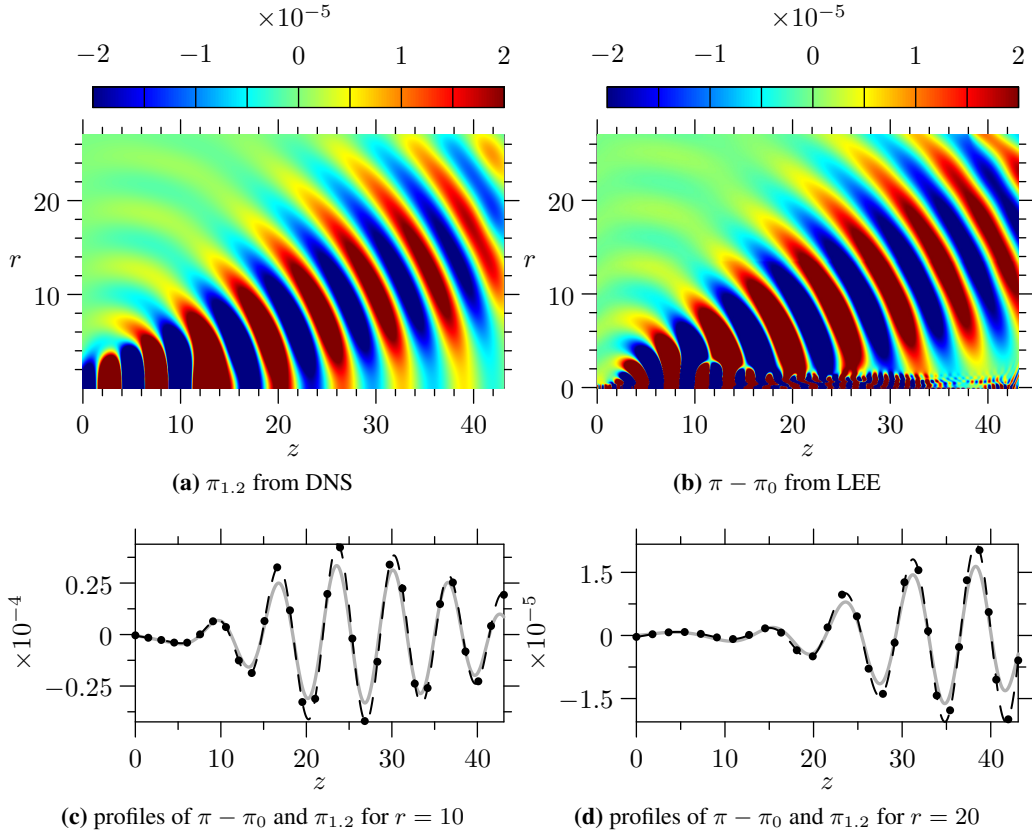


Figure 4.30 – Comparison of the modified pressure field $\pi - \pi_0$, obtained by driving the LEE with the TABF source $(f_{2z})_{1.2}$ and $(f_{2r})_{1.2}$, with the DNS modified pressure field $\pi_{1.2}$ at frequency 1.2. The bottom figures give profiles along $r = 10$ and $r = 20$: the gray line represents the DNS solution ($\pi_{1.2}$) and the dashed black line with black circles the LEE solution ($\pi - \pi_0$).

For all variables but ρv one has, from table 4.4, $q' \ll \bar{q} \ll q_0$ so $q'' \approx \bar{q} - q_0$, which explains why non-radiating components are dominating f_{2z} and $(f_{2z})_{1.2}$. For variable ρv one has $(\rho v)_0 \approx 0$ and $(\rho v)'' \ll \bar{\rho v}$ (see table 4.4) so $(\rho v)'' \approx \rho v \approx \bar{\rho v}$, which explains why f_{2r} and $(f_{2r})_{1.2}$ are also dominated by non-radiating components.

The predominance of non-radiating components in the TABF sources mean that they can be misleading, because their physical properties are likely to reflect that of the non-radiating components rather than that of the radiating components. The apparent location of the sound sources is one example. The axial source reaches its maximum around $z = 12$ but strong peaks can be observed even for $z >= 25$. Figure 4.28(b) shows that $(f_{2z})_{1.2}$ exhibits a wave packet structure centered around 15 jet diameters. Similar observations can be made for the radial source f_{2r} using figure 4.29; in particular, $(f_{2r})_{1.2}$ also reaches its maximum for $z \approx 15$. Thus, the TABF sources are maximum

10 jet diameters downstream of the NRBF sources computed in section 4.4, which is also consistent with the results of table 4.5. Although there is some evidence that the NRBF sources associated with large coherent structures are located close to the end of the potential core (see section 1.6), this property is verified with the NRBF sources but not with the TABF sources.

Another key difference between the TABF source terms and the NRBF sources is their amplitude. From figure 4.28(c), $(f_{2z})_{1.2}$ is of the order of 10^{-3} , compared to 10^{-5} for $(f_{1z})_{1.2}$. Since the sources of sound are expected to be of a similar order of magnitude than the radiating components, i.e. 10^{-5} , $(f_{1z})_{1.2}$ makes more physical sense than $(f_{2z})_{1.2}$ in that respect.

Analysis of the sound generated by the TABF sources

The validation results of figure 4.30 indicates that the radiating field obtained by driving the LEE with the TABF sources is in relatively good agreement with the radiating field of the DNS solution: the directivity is correct but the magnitude is overestimated. This is probably due to the inflow boundary condition. Ideally, the inflow boundary condition of the LEE simulation should match that of the DNS simulation. For simplicity, a buffer zone of thickness $25\Delta z$ has been used at the inflow, whereas the DNS simulation employed an integral boundary condition developed by Sandham and Sandhu [57].

Examining the contribution of each of the term composing the TABF sources leads to results which are different from those based on the NRBF sources. From figure 4.31, the noisiest term is $(1/r)\partial(r\rho_0u''v'')_{1.2}/\partial r$, followed by $\partial(\rho_0u''u'')_{1.2}/\partial z$, $\partial(\rho_0u''v'')_{1.2}/\partial z$ and $(1/r)\partial(r\rho_0v''v'')_{1.2}/\partial r$. The weakest source terms are those involving the unsteady modified pressure π'' . These results are different from those obtained in section 4.4.5 with the NRBF sources, for which the cross terms (involving both the radial velocity and the axial velocity) do not generate significant noise. This can be seen, for example, by comparing figure 4.31(b) with figure 4.23(c).

As shown in figure 4.30(b), the TABF sources generate strong hydrodynamic waves along the jet axis for $r \leq 2$. These hydrodynamic waves are due to the presence of non-radiating components in the TABF sources, which are visible in figures 4.28(a) and 4.29(a). To understand the impact of these hydrodynamic waves on sound radiation, the sound generated from the radiating part of term $S_{zz} = \partial(\rho_0u''u'')_{1.2}/\partial z$ is computed. From figures 4.32(a) and 4.32(b), the sound generated by the radiating part S'_{zz} is much smaller than the sound generated by the full term S_{zz} . This implies that the non-radiating

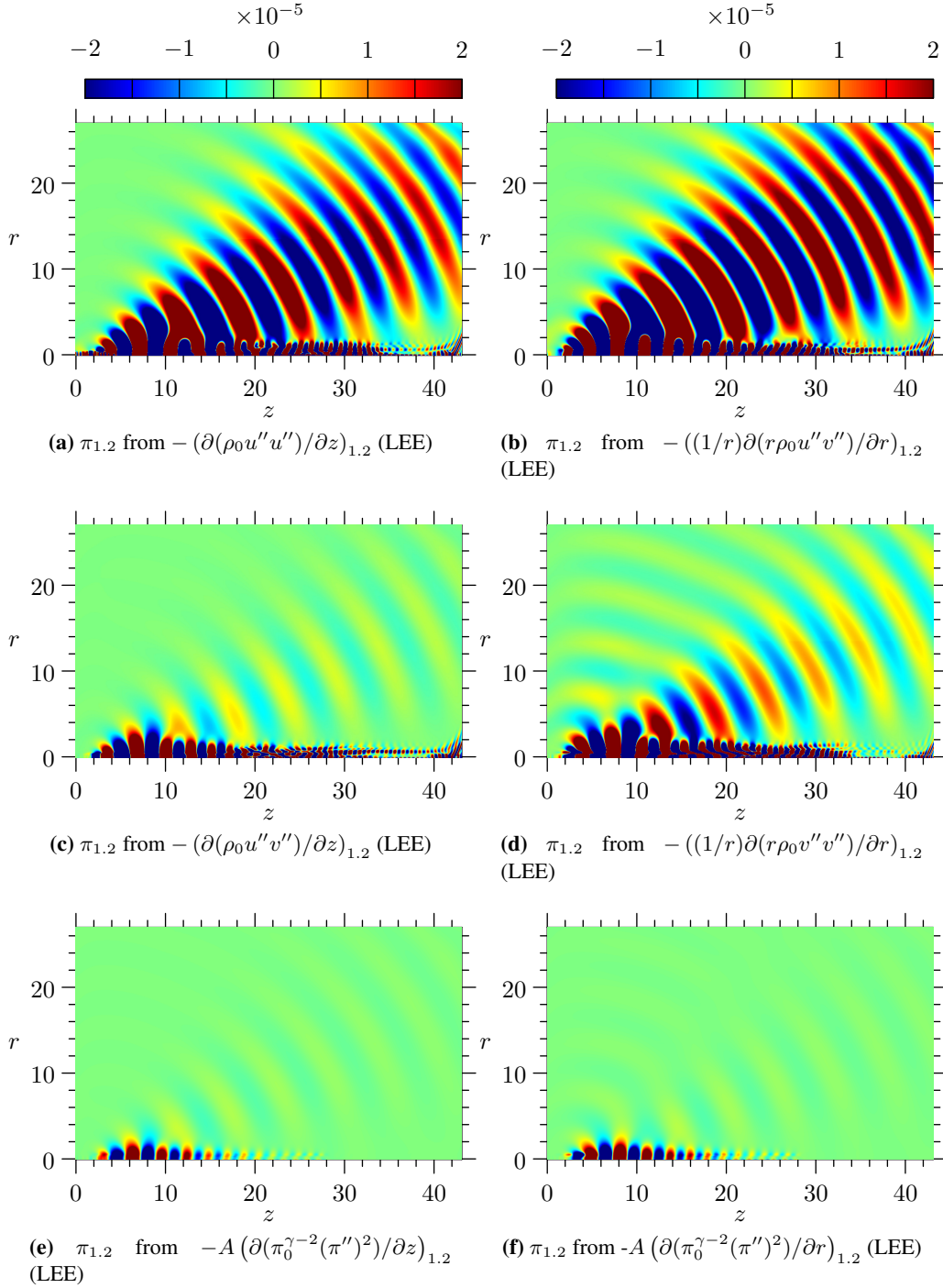


Figure 4.31 – Snapshots of the modified pressure field radiating from the terms that compose the TABF sources $(f_{2z})_{1,2}$ and $(f_{2r})_{1,2}$, compared to the DNS solution $\pi_{1,2}$. In (e) and (f), A represents the constant $0.5\gamma(\gamma - 1)$

part $\overline{S_{zz}}$ is responsible for most of the noise generation. This paradox can be explained by observing that non-radiating components can generate sound indirectly by interacting with a non-uniform mean flow. Part of the vorticity waves generated by $\overline{S_{zz}}$ is converted into acoustic waves because the mean flow is non-uniform. Such conversion between vorticity and acoustics seem negligible when the mean flow is quiescent: for a quiescent base flow, the sound generated by S_{zz} is almost identical to the sound generated by S'_{zz} . This can be seen by comparing figure 4.32(c) with figure 4.32(d). This suggests that, when applying the TABF analogy to this flow field, most of the sound generation occurs on the left hand side of the LEE, within the terms that are linear in the unsteady variables (the so called propagation terms). This shows that it can be misleading to interpret the TABF sources as sound sources.

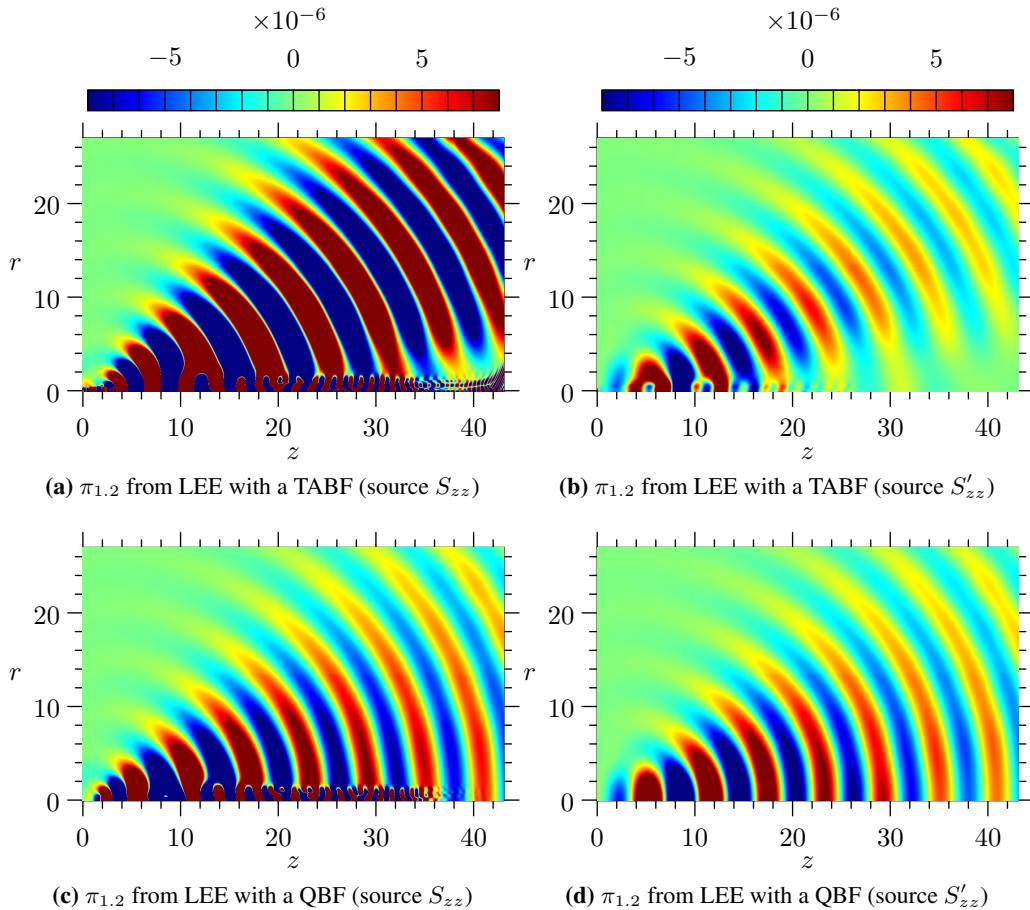


Figure 4.32 – Snapshots of the modified pressure field $\pi_{1,2}$ radiating from the TABF axial momentum source term $S_{zz} = -\partial(\rho_0 u'' u'')_{1,2}/\partial z$ (left column), and from $S'_{zz} = -\partial(\rho_0 u'' u'')'_{1,2}/\partial z$ (right column). In each column, the LEE are solved using the time averaged based flow (top row) or a quiescent base flow (bottom row).

4.7 Source based on a quiescent base flow

In this section, the quiescent base flow (QBF) sources, which have been derived in section 2.3, are computed. The QBF sources are equivalent to Ligthill's sources and include all the propagation effects due to interactions between acoustic waves and the flow field. The aim will be to describe how the physical properties of the QBF sources compare to those of the NRBF and TABF sources.

4.7.1 Algorithm

The algorithm used to compute the QBF sources is as follows:

- compute the dependent variables $\rho, \rho u, \rho v, \pi$, from the DNS data
- compute the axial momentum source f_{3z} as

$$f_{3z} = -\frac{\partial}{\partial z}(\rho_0 uu) - \frac{1}{r} \frac{\partial}{\partial r}(r \rho_0 uv) \quad (4.25)$$

- compute the radial momentum source f_{3r} as

$$f_{3r} = -\frac{\partial}{\partial z}(\rho_0 uv) - \frac{1}{r} \frac{\partial}{\partial r}(r \rho_0 vv) \quad (4.26)$$

- compute $(f_{3z})_{\omega_r}$ and $(f_{3r})_{\omega_r}$ for each radiating frequency ω_r using (4.5).

The above algorithm assumes that the modified pressure terms present in (2.57) are negligible.

4.7.2 Results and discussion

Analysis of the source fields

The axial QBF source f_{3z} is plotted in figure 4.33(a), and $(f_{3z})_{1.2}$ is shown in figure 4.33(b). Profiles of f_{3z} and $(f_{3z})_{1.2}$ along $r = 0$ are shown in figures 4.33(c) and 4.33(d) respectively. Similarly, the radial QBF sources f_{3r} and $(f_{3r})_{1.2}$ are presented in figure 4.34, with profiles along $r = 0.5$. The profiles of figures 4.33(c) and 4.34(c) indicate that sources f_{3z} and f_{3r} are dominated by low frequencies close to inlet ($z \leq 5$) and by high frequency further downstream ($z \geq 10$). This is expected: the jet is excited at the inlet at frequencies 2.2 and 3.4, which generate hydrodynamic waves that interact non-linearly and generate additional frequencies such as 1.2, 4.4 and 5.6. As shown in 4.33(d) and 4.34(d), frequency 1.2 becomes significant around $z = 4$ for f_{3z} and around $z = 2$ for f_{3r} ; in both cases, the source reaches a peak around $z = 13$. These two figures, as well as figures 4.33(b)

and 4.34(b), show that $(f_{3z})_{1.2}$ and $(f_{3r})_{1.2}$ exhibit wavepacket structures that are centered respectively around the jet axis and the jet shear layer, and which extend roughly between 2 and 20 jet diameters in the axial direction.

Compared to the TABF sources shown in figure 4.28 and 4.29, the QBF sources have a higher amplitude (roughly one order of magnitude). Most importantly comparing the profiles of $(f_{2z})_{1.2}$ and $(f_{3z})_{1.2}$, and of $(f_{2r})_{1.2}$ and $(f_{3r})_{1.2}$, show that the wavepacket structure of the TABF sources is truncated compared to that of the QBF sources: its amplitude is almost zero for $z < 13$. Therefore, if most of the sound generation occurs for $z < 13$, as the NRBF sources shown in figure 4.20 suggest, then the QBF sources appear to make more physical sense as sources of sound than the TABF sources. This result is paradoxical, as the TABF sources are often thought to be an improvement over Lighthill's sound sources, in terms of physical understanding, because they remove some propagation effects from the source.

Compared to the NRBF sources shown in figure 4.20, the QBF sources have an amplitude that is at least 3 orders of magnitude larger. This is due to the non-radiating components that are present in the QBF sources. It makes them difficult to interpret directly as sound sources. For example, they are maximum around $z = 13$ whereas the NRBF sources are maximum around $z = 6$.

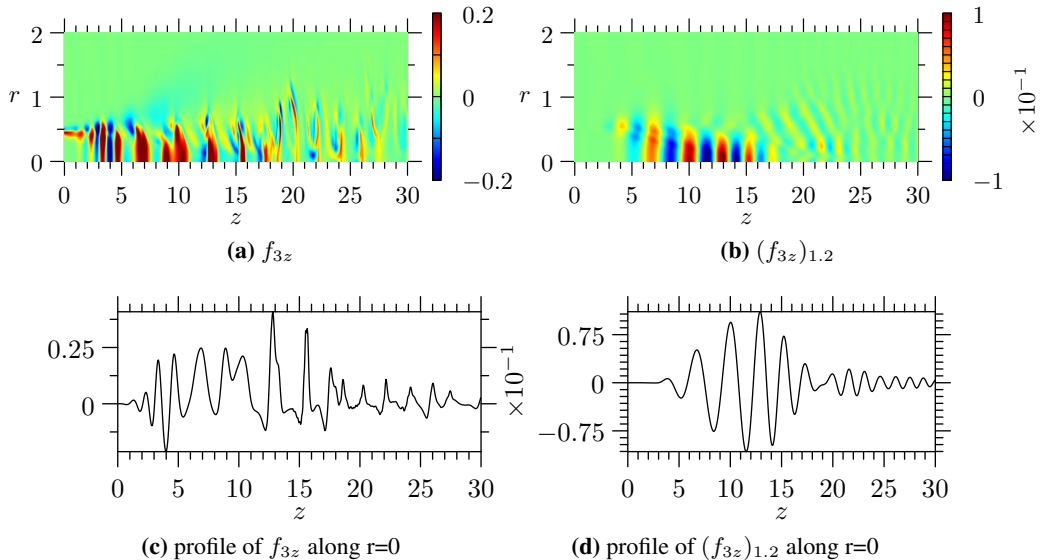


Figure 4.33 – QBF source f_{3z} in the axial direction at time $t = 157.18$, and its components $(f_{3z})_{1.2}$ at frequency 1.2. Figures (c) and (d) give profiles along $r = 0$.

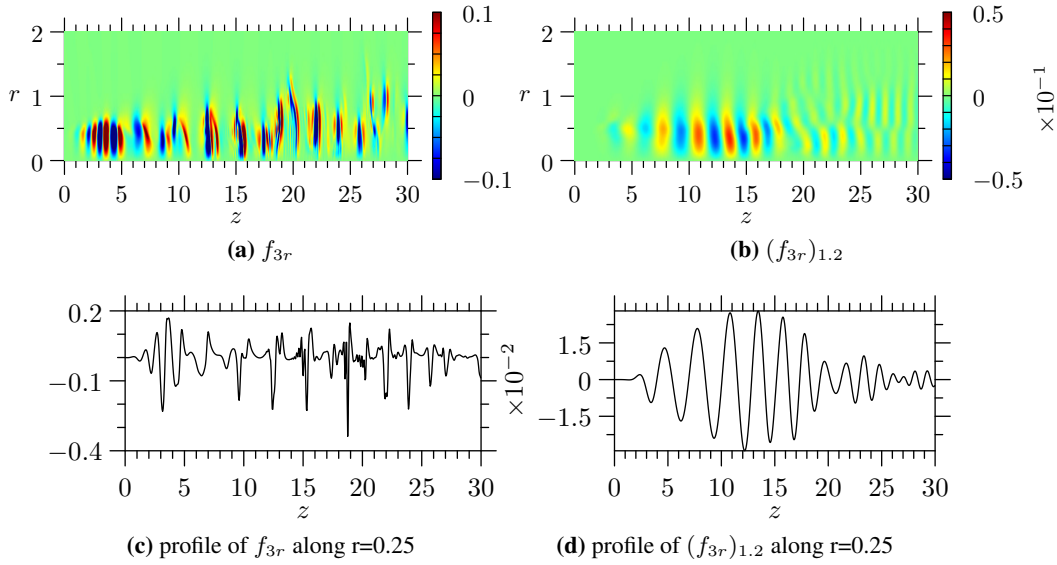


Figure 4.34 – QBF source f_{3r} in the radial direction at time $t = 157.18$, and its components $(f_{3r})_{1.2}$ at frequency 1.2. Figures (c) and (d) give profiles along $r = 0.5$.

Validation

The QBF sources $(f_{3z})_{1.2}$ and $(f_{3r})_{1.2}$ are used to drive the linearized Euler equations. The mean flow is quiescent and is obtained using (2.53). The radiating sound field is compared to the one obtained from the DNS solution in figure 4.35. The sound radiating from the QBF sources is in very good agreement with the DNS solution. Small differences for $z \geq 35$ are due to the 100 points buffer used as a boundary condition. Note also that the QBF sources, like the TABF sources, generate hydrodynamic fluctuations that propagate along the jet axis for $r \leq 2$. However, unlike the TABF sources, these hydrodynamic fluctuations are not converted into acoustics through interactions with the base flow, since the base flow is quiescent. Thus, the QBF sources appear more straightforward to interpret as sources of sound compared to the TABF sources. Nevertheless, comparing figures 4.22(b) and 4.35(b) indicates that the NRBF sources do not excite any hydrodynamic waves: they do seem to be free of the large non-radiating components which hamper the interpretation of the QBF sources.

Dominant terms

The QBF sources comprise four distinct terms:

- $f_{3zz} = -\partial(\rho_\infty uu)/\partial z,$
- $f_{3zr} = -(1/r)\partial(r\rho_\infty uv)/\partial r,$

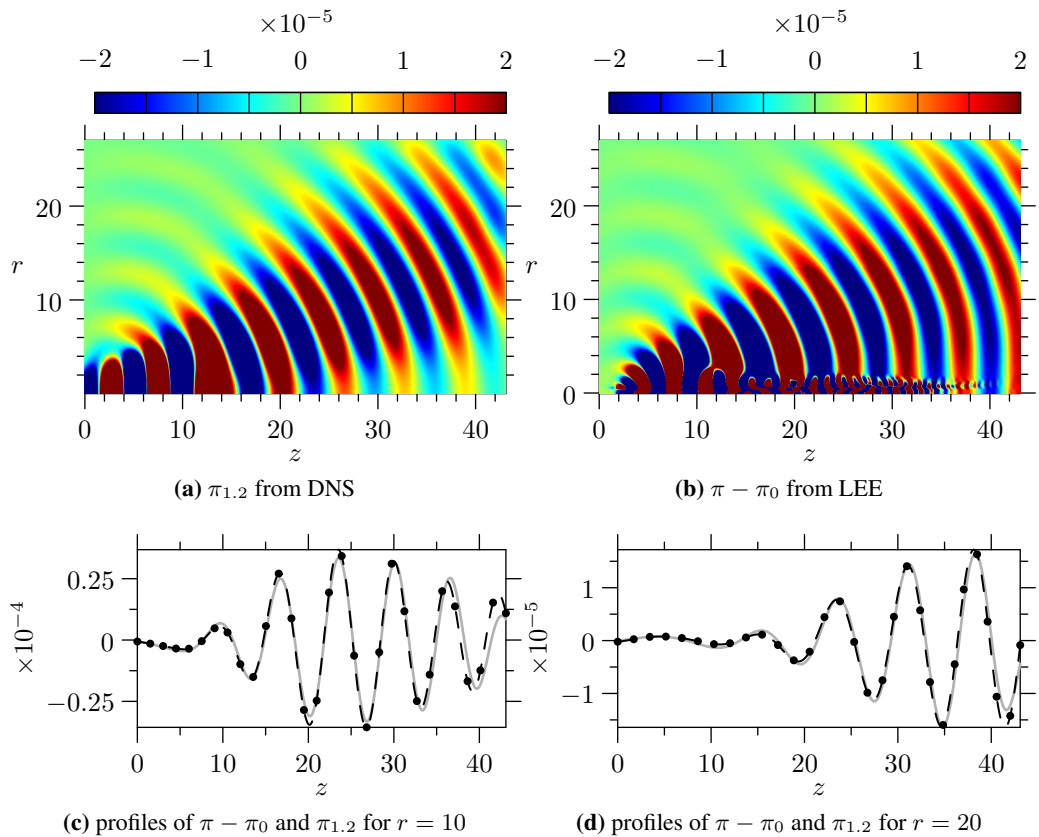


Figure 4.35 – Comparison of the modified pressure field $\pi - \pi_0$, obtained by driving the LEE with the QBF sources $(f_{3z})_{1.2}$ and $(f_{3r})_{1.2}$, with the DNS modified pressure field $\pi_{1.2}$ at frequency 1.2. The bottom figures give profiles along $r = 10$ and $r = 20$: the gray line represents the DNS solution ($\pi_{1.2}$) and the dashed black line with black circles the LEE solution ($\pi - \pi_0$).

- $f_{3rz} = -\partial(\rho_\infty vu)/\partial z$
- $f_{3rr} = -(1/r)\partial(r\rho_\infty vv)/\partial r.$

The sound radiated by each term individually is computed at frequency 1.2. Snapshots of the modified pressure field are presented in figure 4.36, in which the DNS result has been included for convenience. Most of the sound is found to be generated by f_{3zz} , with some small contributions from f_{3rr} at large angles. The cross terms f_{3rz} and f_{3zr} can be neglected in terms of sound generation. These conclusions are identical to those obtained from the NRBF sources (figure 4.23), but not to those obtained from the TABF sources (figure 4.31).

4.8 Conclusion

For a homentropic flow surrounded by a quiescent medium, the NRBF sources can be expressed in terms of the non-radiating parts of the density and momentum density fields. The dominant source term, $\partial(\bar{\rho}\tilde{u}\tilde{u})'/\partial z$ involves the non-radiating density and axial momentum density. In this chapter, the NRBF sources have been computed for a laminar axisymmetric jet, for the three frequencies which dominate the acoustic field. These sources take the form of wavepackets centered around the end of the potential core. They have been validated by comparing the sound generated by the NRBF sources with the DNS solution. As expected from a source of sound, the amplitude of the source fluctuations is similar to that of the radiating field. If these sources are used to drive the linearized Euler equations, they do not generate much hydrodynamic components.

These valuable physical properties are not satisfied by the sources based on a time averaged base flow. For the jet studied in this section, the TABF sources appear to generate sound indirectly: they mostly generate vorticity waves, which are later converted into acoustic waves through interactions with the mean flow. The physical interpretation of the QBF sources appears more straightforward as they do contain the terms directly responsible for sound radiation. Nevertheless, the QBF source term also contain strong non-radiating components which hamper the physical understanding. Using the NRBF sources can help to overcome this difficulty; the NRBF sources contain only the part of the QBF sources that is responsible for sound generation.

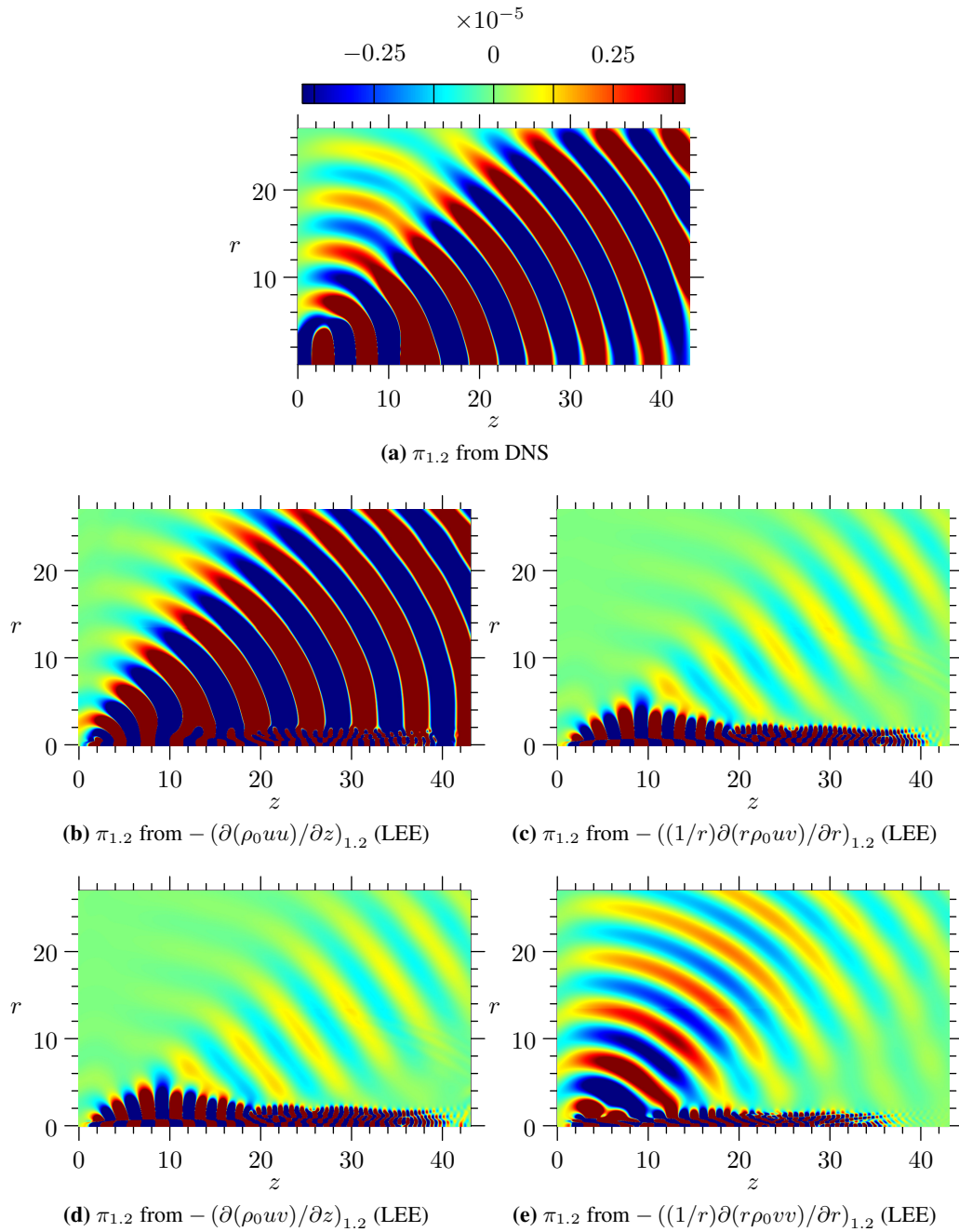


Figure 4.36 – Snapshots of the modified pressure field radiating from the terms that compose the QBF sources $(f_{3z})_{1,2}$ and $(f_{3r})_{1,2}$, compared to the DNS solution $\pi_{1,2}$.

Chapter 5

Conclusion

An analytic expression has been derived for the sound sources based on a non-radiating base flow (NRBF). That expression is valid for a free homentropic flow in a quiescent medium. It could however be extended to accommodate more general flow fields.

The NRBF sources are associated with a propagation operator which allows to propagate the sound to the far field. This propagation operator is based on the Euler operator linearized about the non-radiating flow field. It also requires to retain only the radiating part of the interaction terms between the dependent variables and the non-radiating flow field. However, when most propagation effects are due to interactions with the mean flow, the propagation operator can be approximated by the Euler operator linearized about the mean flow.

It has been shown that the non-radiating base flow can be computed using convolution filters. These filters rely on the radiation criterion $|k| = |\omega|/c_\infty$ and are best applied in the frequency-wavenumber domain. This has been demonstrated for a linear flow field in chapter 3, and for a Mach 0.9 axisymmetric jet in chapter 4.

The NRBF sources have been computed and validated successfully for a Mach 0.9 axisymmetric jet, at three different frequencies. Two interesting properties of the NRBF sources are that they are of a similar order of magnitude as the sound field, and that they are maximum near the end of the potential core. Moreover, the NRBF sources have been found to generate little to no hydrodynamic waves when used as source terms on the right hand side of the linearized Euler equations.

Sources based on a time-averaged base flow (TABF), and on a quiescent base flow (QBF) have also been computed and validated. The amplitude and distribution of the NRBF sources have been found to be more physical than

those of the TABF and QBF sources. This suggests that the NRBF are an improvement over classical acoustic analogies, in terms of understanding the physics of sound generation.

Although the TABF sources are often thought to be closer to the physical sources of sound than the QBF sources, this has been found not to be the case for the axisymmetric jet presented in this thesis. The TABF sources are more misleading in this case as they do not contain the terms responsible for the actual sound generation: these terms are a linear function of the unsteady flow field; by construction, they have been left out of the TABF sources. Paradoxically, the QBF sources can hence be easier to interpret as sources of sound than the TABF sources.

Appendices

Appendix A

Hankel transform

A.1 Definition

The Hankel transform of order ν of a function $f(x)$ is defined as

$$F_\nu(k) = \int_0^{+\infty} f(x) J_\nu(kx) x dx, \quad (\text{A.1})$$

where J_ν denotes the Bessel function of order ν .

The inverse Hankel transform is defined as

$$f(k) = \int_0^{+\infty} F_\nu(k) J_\nu(kx) k dk. \quad (\text{A.2})$$

Note that the forward and inverse Hankel transform are identical.

A.2 Fourier transform of a radially symmetric signal in two-dimensions

A.2.1 Scalar field

Forward transform

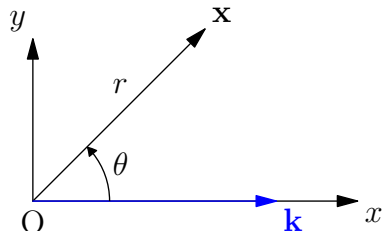


Figure A.1 – cylindrical polar coordinate system in x-domain

Let g be a radially symmetric function of position in the two-dimensional plane \mathcal{S} . For a given wavenumber \mathbf{k} , the cartesian coordinate system of figure A.1 is chosen; it is such that \mathbf{k} is along the x -axis. The value of the Fourier transform in space $G(\mathbf{k})$ is given by

$$G(\mathbf{k}) = \int_{\mathcal{S}} g(\mathbf{x}) e^{i(\omega t - \mathbf{k} \cdot \mathbf{x})} d^2 \mathbf{x} \quad (\text{A.3})$$

$$= \int_0^{+\infty} \int_0^{2\pi} g(r) e^{-ikr \cos \theta} r d\theta dr \quad (\text{A.4})$$

$$= \int_0^{+\infty} g(r) r \int_0^{2\pi} e^{-ikr \cos \theta} d\theta dr. \quad (\text{A.5})$$

From Abramowitz and Stegun [58],

$$J_\nu(z) = \frac{i^{-\nu}}{\pi} \int_0^\pi \cos(\nu\theta) \exp[-iz \cos(\theta)] d\theta. \quad (\text{A.6})$$

Using this relation and the fact that $J_\nu(-z) = (-1)^\nu J_\nu(z)$ (using equation 9.1.10 in reference[58]), it can be shown that

$$\int_0^{2\pi} e^{-ikr \cos \theta} d\theta = 2\pi J_0(kr). \quad (\text{A.7})$$

Substituting (A.7) into (A.5), one can write

$$G(\mathbf{k}) = 2\pi \int_0^{+\infty} g(r) J_0(kr) r dr. \quad (\text{A.8})$$

Comparing equations (A.1) and (A.12) shows that the two-dimensional Fourier transform of a radially symmetric signal $g(r)$ is given by the Hankel transform of $g(r)$ of order 0.

Inverse transform

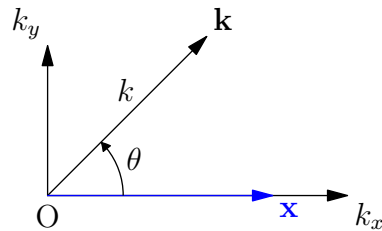


Figure A.2 – cylindrical polar coordinate system in \mathbf{k} -domain

Let G be a radially symmetric function of position in the wavenumber plane \mathcal{S} . For a given position \mathbf{x} , the Cartesian coordinate system of figure A.2

is chosen; it is such that \mathbf{x} is along the k_x -axis. Term $|\mathbf{x}|$ is denoted by r . The value of the inverse Fourier transform in space $g(\mathbf{x})$ is given by

$$g(\mathbf{x}) = \frac{1}{(2\pi)^2} \int_{\mathcal{S}} G(\mathbf{k}) e^{i\mathbf{k}\cdot\mathbf{x}} d^2\mathbf{k} \quad (\text{A.9})$$

$$= \frac{1}{(2\pi)^2} \int_0^{+\infty} \int_0^{2\pi} G(k) e^{ikr \cos \theta} k d\theta dk \quad (\text{A.10})$$

$$= \frac{1}{(2\pi)^2} \int_0^{+\infty} G(k) k \int_0^{2\pi} e^{ikr \cos \theta} d\theta dk \quad (\text{A.11})$$

$$= \frac{1}{2\pi} \int_0^{+\infty} g(k) J_0(kr) k dk. \quad (\text{A.12})$$

Comparing equations (A.2) and (A.12) shows that the two-dimensional Fourier transform of a radially symmetric signal $g(r)$ is given by the inverse Hankel transform of $g(r)$ of order 0.

A.2.2 Vector field

Forward transform

The Fourier transform of signals of the form $\mathbf{g} = g(r)\mathbf{e}_r$, where \mathbf{e}_r is a unit vector in the radial direction, needs to be computed. For example, such signals appear in the radial momentum equation (2.4). If the coordinate system of figure A.1 is used, one has

$$\mathbf{e}_r = \cos(\theta)\mathbf{e}_x + \sin(\theta)\mathbf{e}_y, \quad (\text{A.13})$$

where \mathbf{e}_x and \mathbf{e}_y are the unit vectors in the x - and y -direction respectively. Equation (A.13) shows that e_r is a function of angle θ . The Fourier transform of \mathbf{u} is given by

$$\begin{aligned} \mathbf{G}(\mathbf{k}) &= \int_0^{+\infty} \int_0^{2\pi} g(r) e^{-ikr \cos \theta} \mathbf{e}_r r d\theta dr \\ \mathbf{G}(\mathbf{k}) &= \int_0^{+\infty} rg(r) \left(\int_0^{2\pi} \cos \theta e^{-ikr \cos \theta} d\theta \right) dr \mathbf{e}_x \\ &\quad + \int_0^{+\infty} rg(r) \left(\int_0^{2\pi} \sin \theta e^{-ikr \cos \theta} d\theta \right) dr \mathbf{e}_y. \end{aligned} \quad (\text{A.14})$$

Observing that \sin is the derivative of $(-\cos)$, and that $(-\cos)$ is 2π -periodic, one has

$$\int_0^{2\pi} \sin \theta e^{-ikr \cos \theta} d\theta = 0. \quad (\text{A.15})$$

Using (A.6), it can be shown that

$$\int_0^{2\pi} \cos \theta e^{-ikr \cos \theta} d\theta r = -2\pi i J_1(kr). \quad (\text{A.16})$$

Substituting (A.15) and (A.16) into (A.14), one has

$$G(\mathbf{k}) = -2\pi i \int_0^{+\infty} g(r) J_1(kr) r dr \mathbf{e}_x. \quad (\text{A.17})$$

Comparing equations (A.1) and (A.17) shows that the two-dimensional Fourier transform of a radially symmetric vector field $g(r)$ is given by the Hankel transform of $g(r)$ of order 1.

Inverse transform

From (A.2) and (A.17), the inverse Fourier transform of $G(\mathbf{k})$ is given by the inverse Hankel transform of order 1 of $G(k)$.

A.3 Fourier transform of an axisymmetric signal

A.3.1 Scalar field

If $g(r, z)$ is an axisymmetric signal, it is easy to show using section A.2, that the Fourier transform of $g(r, z)$ is equal to Hankel transform of order 0 of $f(r, z)$ in the radial direction, combined with a Fourier transform in the axial direction. Similarly, the inverse Fourier transform will be given by an inverse Fourier transform over k_z followed by an inverse Hankel transform of order 0 over k_r .

A.3.2 Vector field

Similarly, for an axisymmetric vector field $g(r, z)\mathbf{e}_r$ in the radial direction, the Fourier transform is equal to Hankel transform of order 1 in the radial direction, combined with a Fourier transform in the axial direction. The inverse Fourier transform is given by an inverse Fourier transform over k_z followed by an inverse Hankel transform of order 1 over k_r .

Appendix B

Sources of sound in a laminar jet: additional results

B.1 Flow analysis

- The steady part of the density, radial momentum and modified pressure are shown in figure B.1.
- The error between the computed mean flow of figure B.1 and the prescribed mean flow of Stromberg is shown in figure B.2.
- Instantaneous flow directivity at time $t = 0$: figure B.4.
- Instantaneous flow flow profiles at time $t = 0$, in both near field and far field: figure B.5.
- Snapshot of modified pressure π at frequencies $\omega = 1.0, 1.2$ and 2.2 , for $r \leq 2$ and $t = 0$: figure B.6.
- Fourier transform in space of the ρ_{ω_r} , $(\rho u)_{\omega_r}$ and $(\rho v)_{\omega_r}$ for $\omega_r = 1.0, 1.2$ and 2.2 : figure B.7

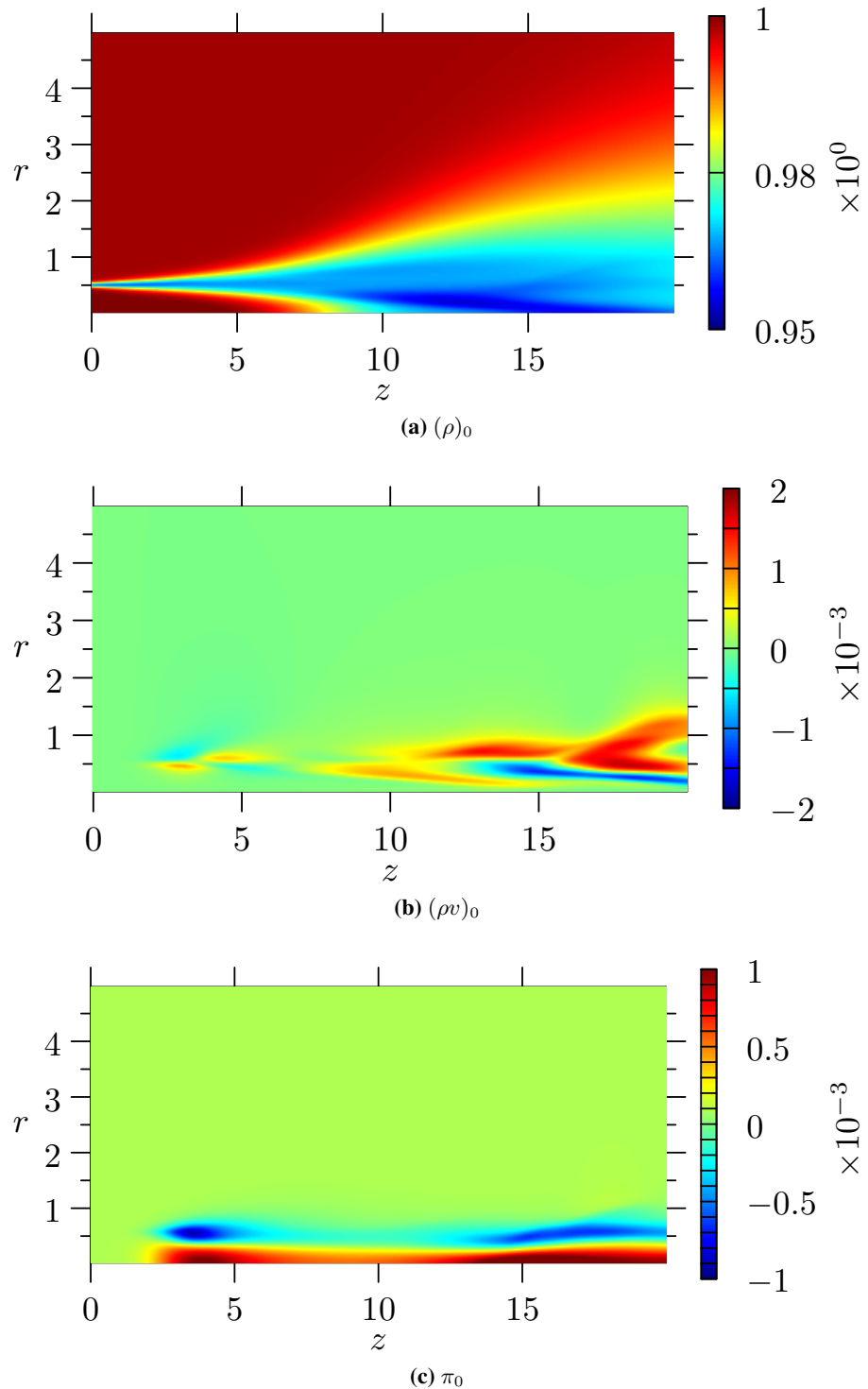


Figure B.1 – Time averaged density, radial momentum and pressure fields for the laminar jet problem.

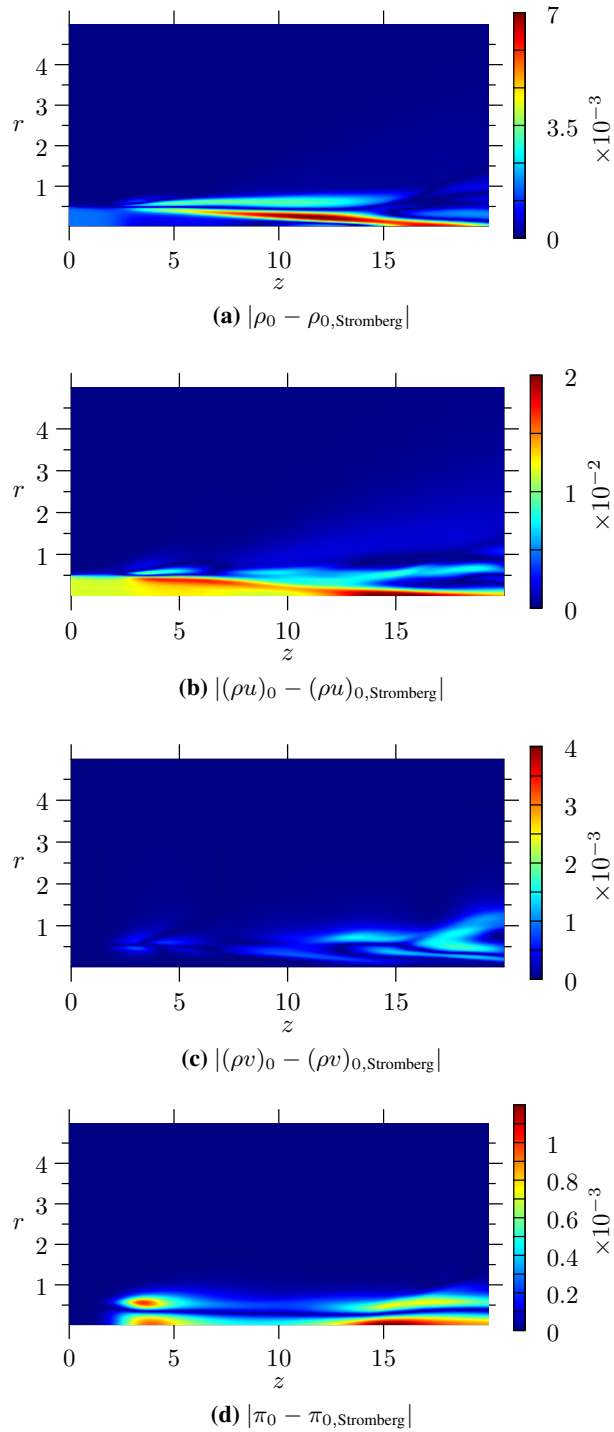


Figure B.2 – Comparison of computed steady flow (subscript 0) and Stromberg’s steady flow (subscript 0, Stromberg) using norm l_1 .

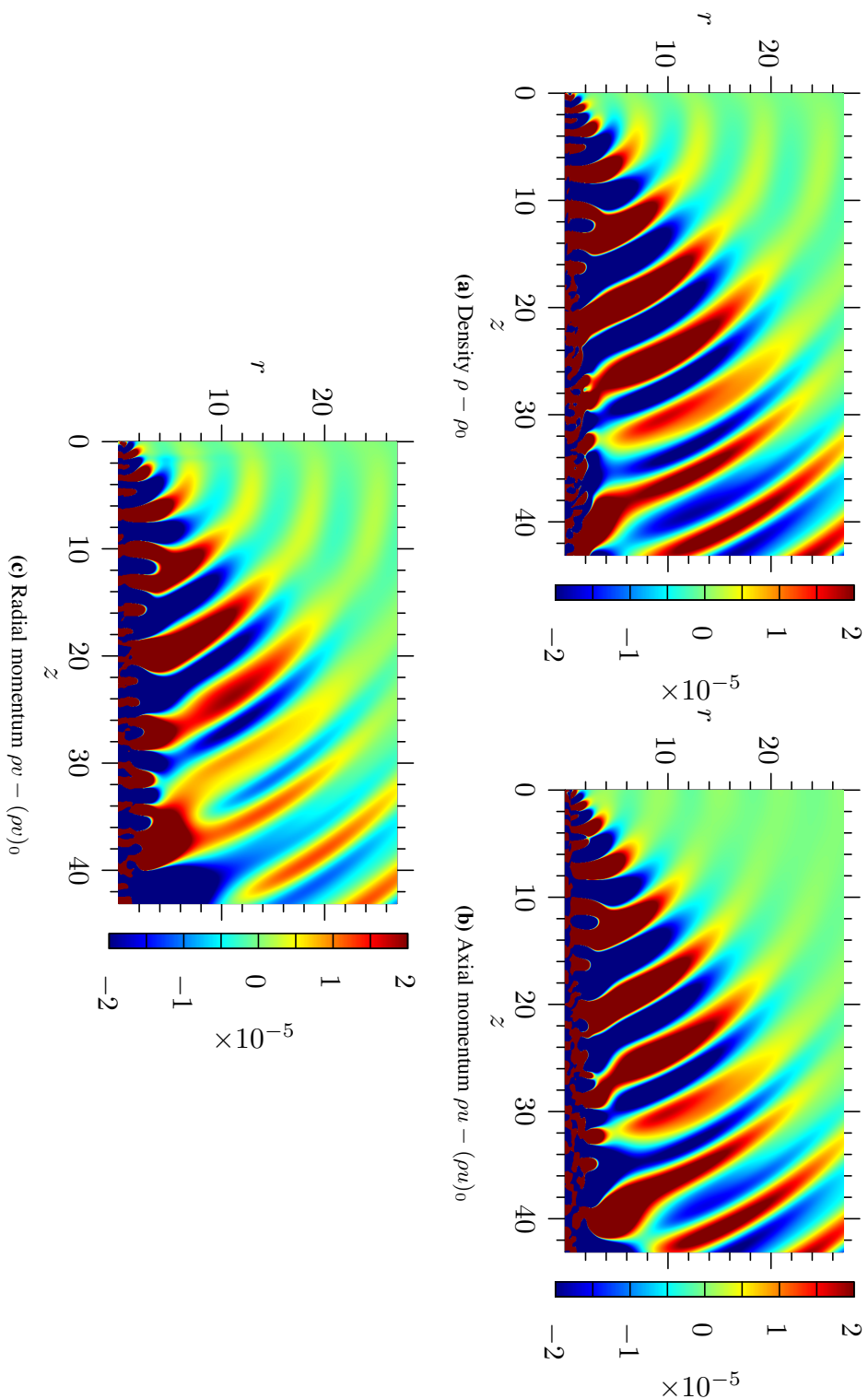


Figure B.3 – Snapshots of the unsteady part of the flow field for time $t = 0$. Hydrodynamic fluctuations propagate along the jet axis while acoustic waves are radiating to the far field.

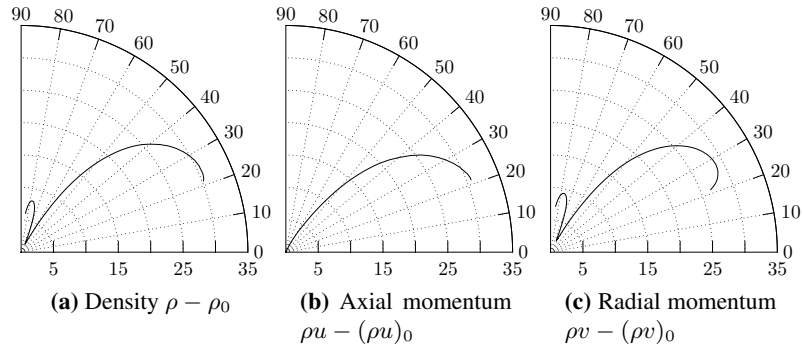


Figure B.4 – Instantaneous flow directivity $D_q(t, \theta, R)$ in decibels for θ between 20 and 85 degrees for all the flow variables $\rho - \rho_0$, $\rho u - (\rho u)_0$ and $\rho v - (\rho v)_0$. The peak radiation angle is 25° . A side lobe be observed at 78° .

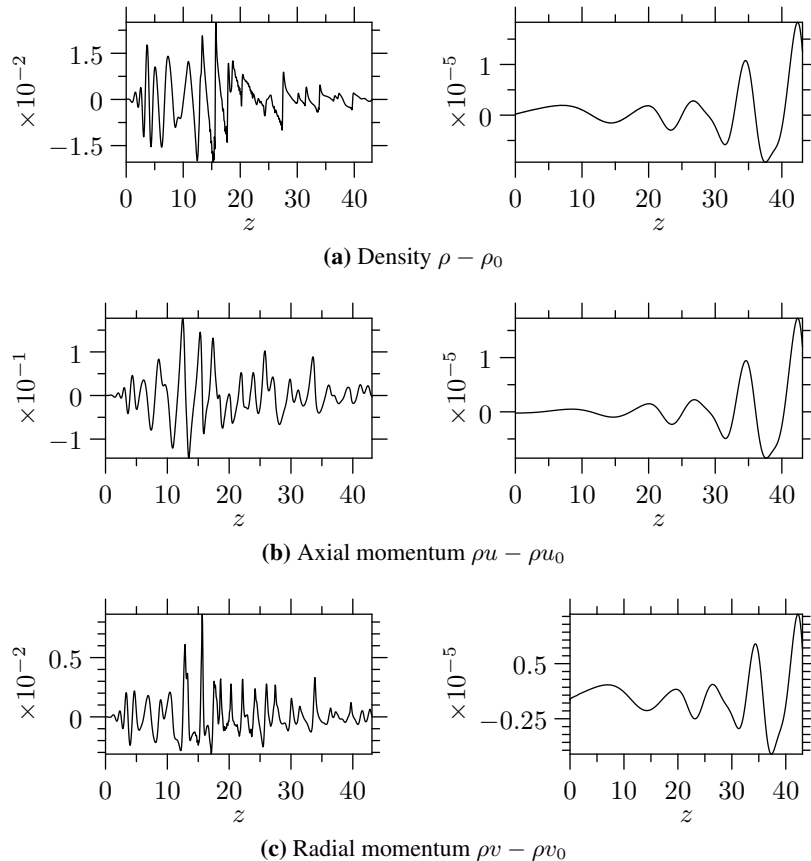


Figure B.5 – Instantaneous flow profiles in the near-field ($y = 0$, left column) and far field ($y = 25$, right column).

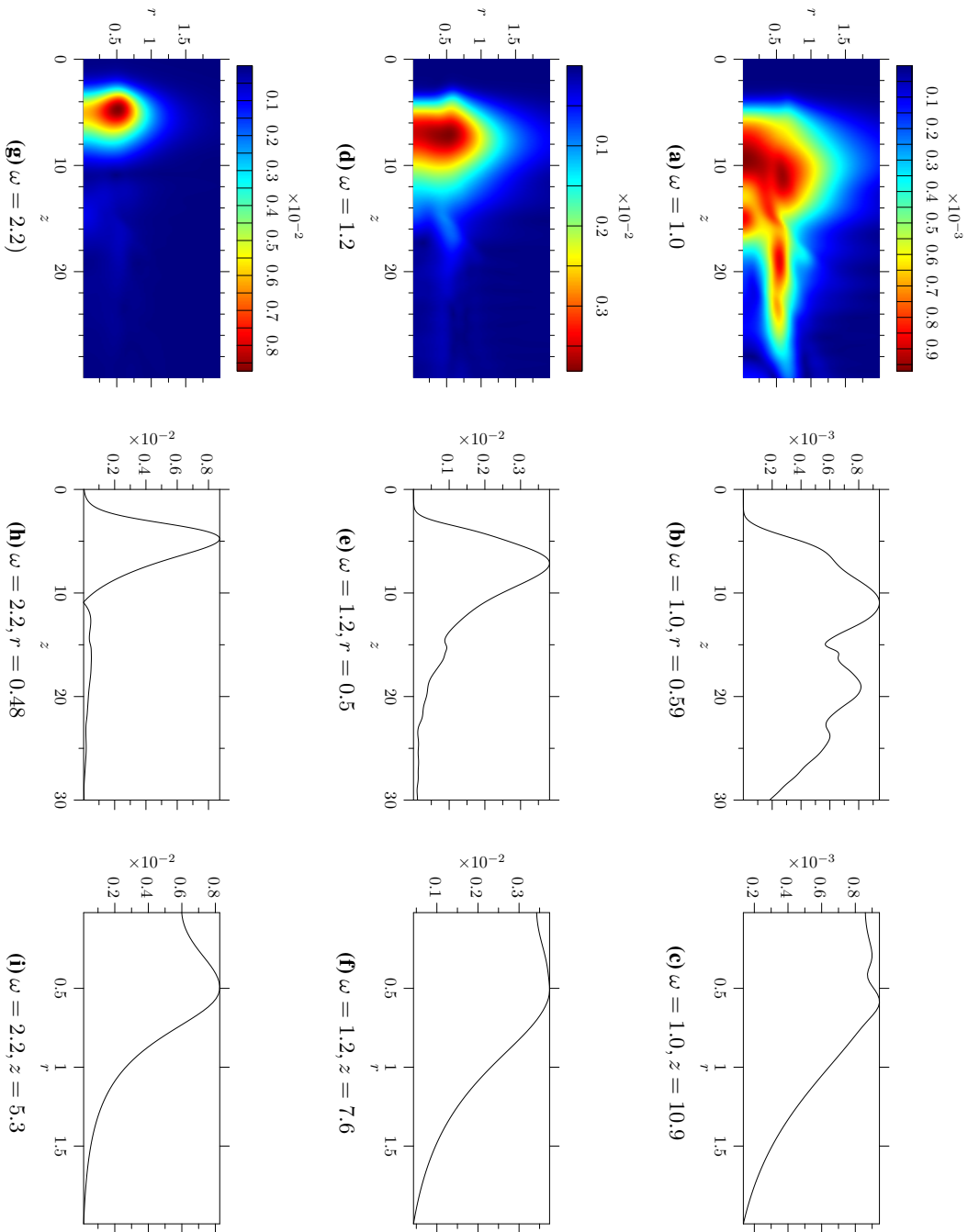


Figure B.6 – Magnitude of the modified pressure field $|\pi(z, r, \omega)|$ for $\omega = 1.0$ (top row), 1.2 (middle row) and 2.2 (bottom row). The first column shows $|\pi(z, r, \omega)|$ for $r \leq 2$. For each frequency, the position of the maximum (r_0, z_0) is calculated and the profiles $|\pi(r = r_0, z, \omega)|$ (middle column) and $|\pi(r, z = z_0, \omega)|$ (right column) are plotted.

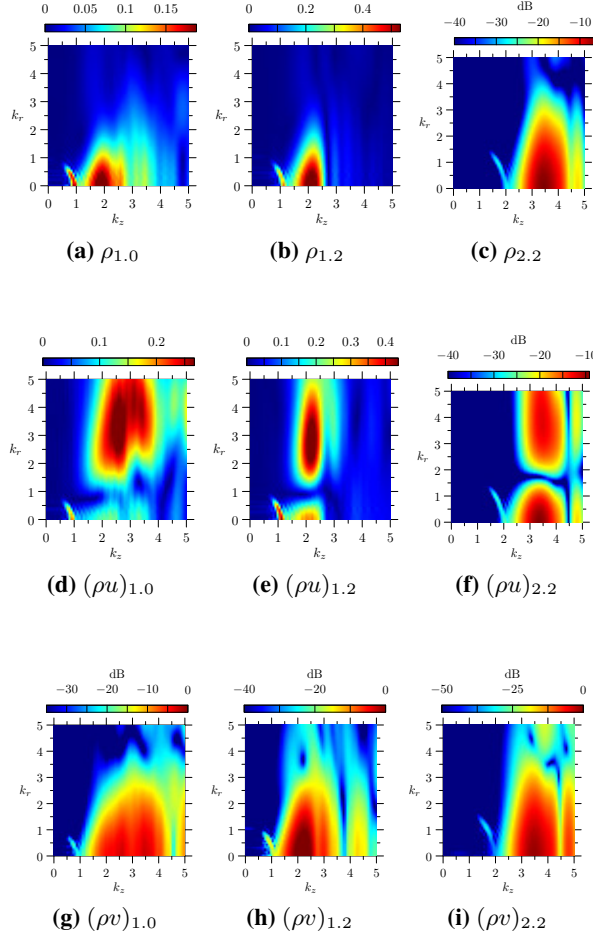


Figure B.7 – Fourier transform in space of instantaneous flow variables $q_\omega(t, z, r)$ at $t = 0$ for $\omega = 1.0$ (left column), 1.2 (middle column) and 2.2 (right column), where $q = \rho$ (top row), ρu (middle row) and ρv (bottom row). The radiating components can be seen on the radiation circle defined as $|\mathbf{k}| = \omega/c_\infty$ ($c_\infty = 1/M \approx 1.1$).

B.2 Flow filtering

- Radiating and non-radiating components of ρ_{ω_r} , $(\rho u)_{\omega_r}$ and $(\rho v)_{\omega_r}$ in the wavenumber domain: figure B.8.
- Radiating and non-radiating components of $(\pi)_{1.0}$ and $(\pi)_{2.2}$ in the time domain: figures B.9 and B.10.
- Radiating and non-radiating components of $(\pi)_{1.0}$ and $(\pi)_{2.2}$ in the time domain: figures B.9 and B.10.
- Radiating and non-radiating components of ρ , ρu and ρv in the time domain: figures B.11, B.12 and B.13.

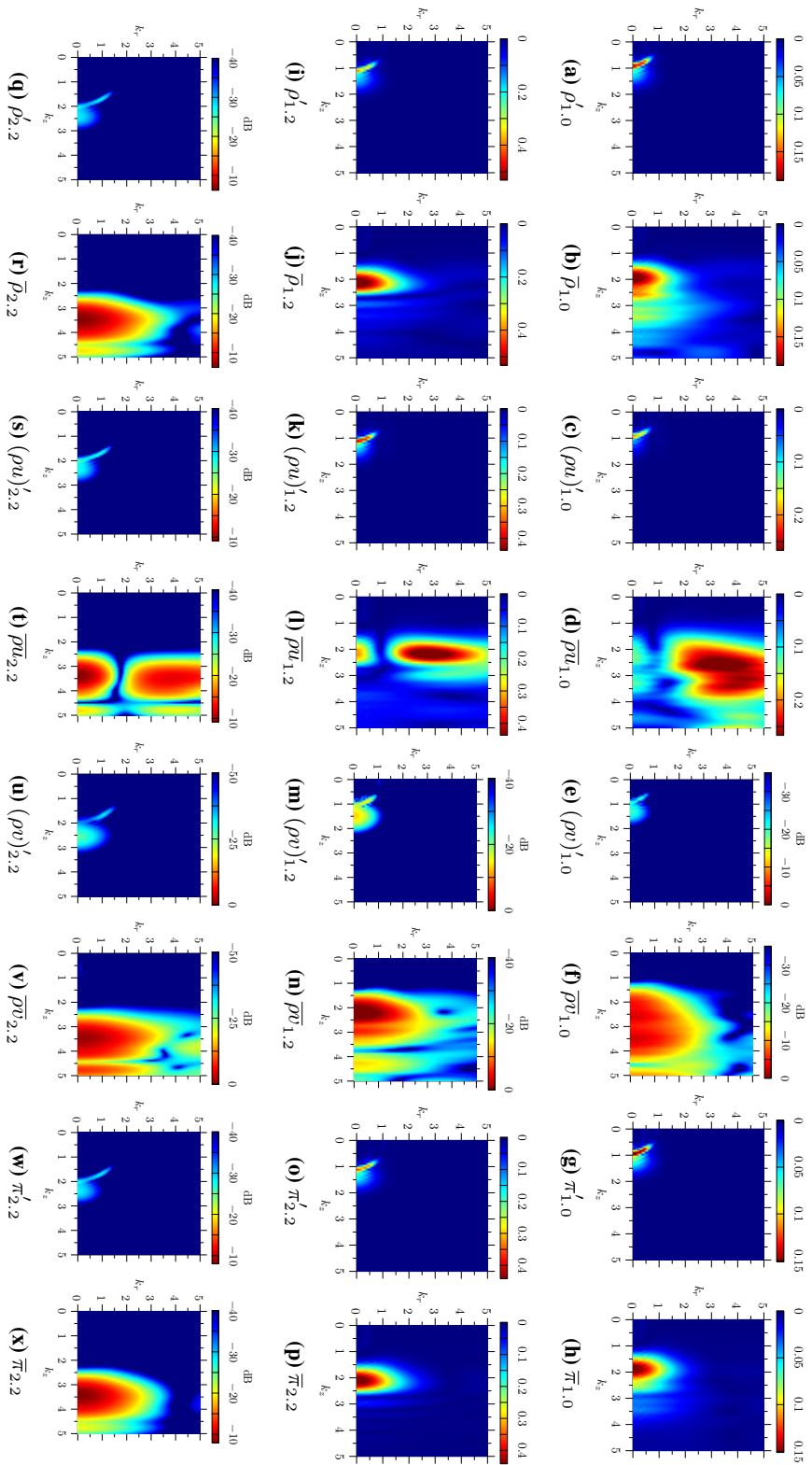


Figure B.8 – Radiating and non-radiating components of the instantaneous flow variables ρ_ω , $(\rho u)_\omega$, $(\rho v)_\omega$ and π_ω , at frequencies $\omega = 1.0$ (top row), 1.2 (middle row) and 2.2 (bottom row), in the wavenumber domain using a Gaussian radiating filter.

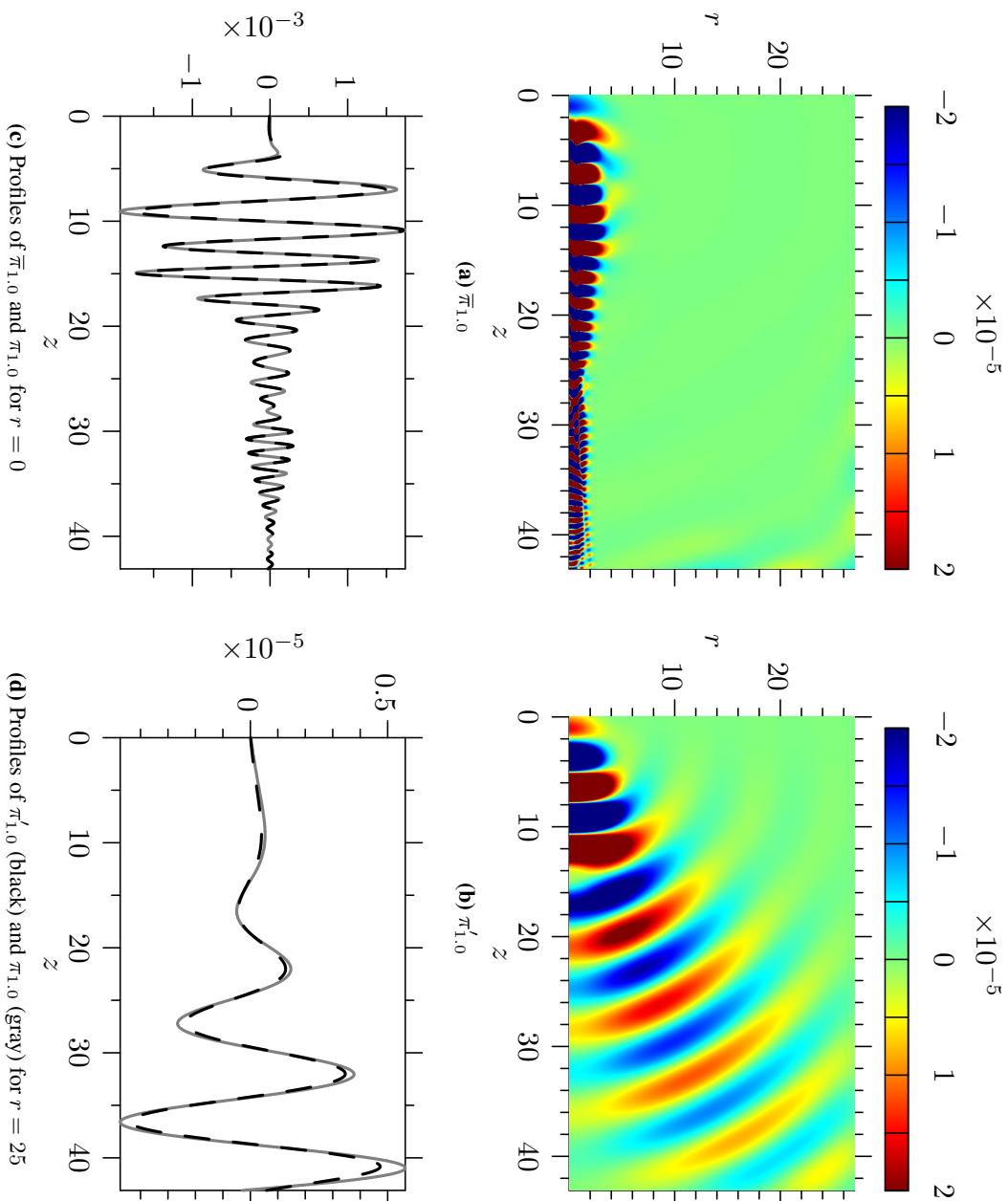


Figure B.9 – Pseudo colour plots and profiles of non radiating pressure $\bar{\pi}_{1,0}$ ((a) and (c)) and radiating pressure $\pi'_{1,0}$ ((b) and (d)) at radiating frequency $\omega_r = 1.0$ and time $t = 0$. The profiles are taken both in the source region (c) and acoustic region (d), at $r = 0$ and $r = 25$ respectively. In the profiles ((c) and (d)), the gray solid line represents $\pi_{1,0}$. The dashed black line represents $\bar{\pi}_{1,0}$ in (c) and $\pi'_{1,0}$ in (d).

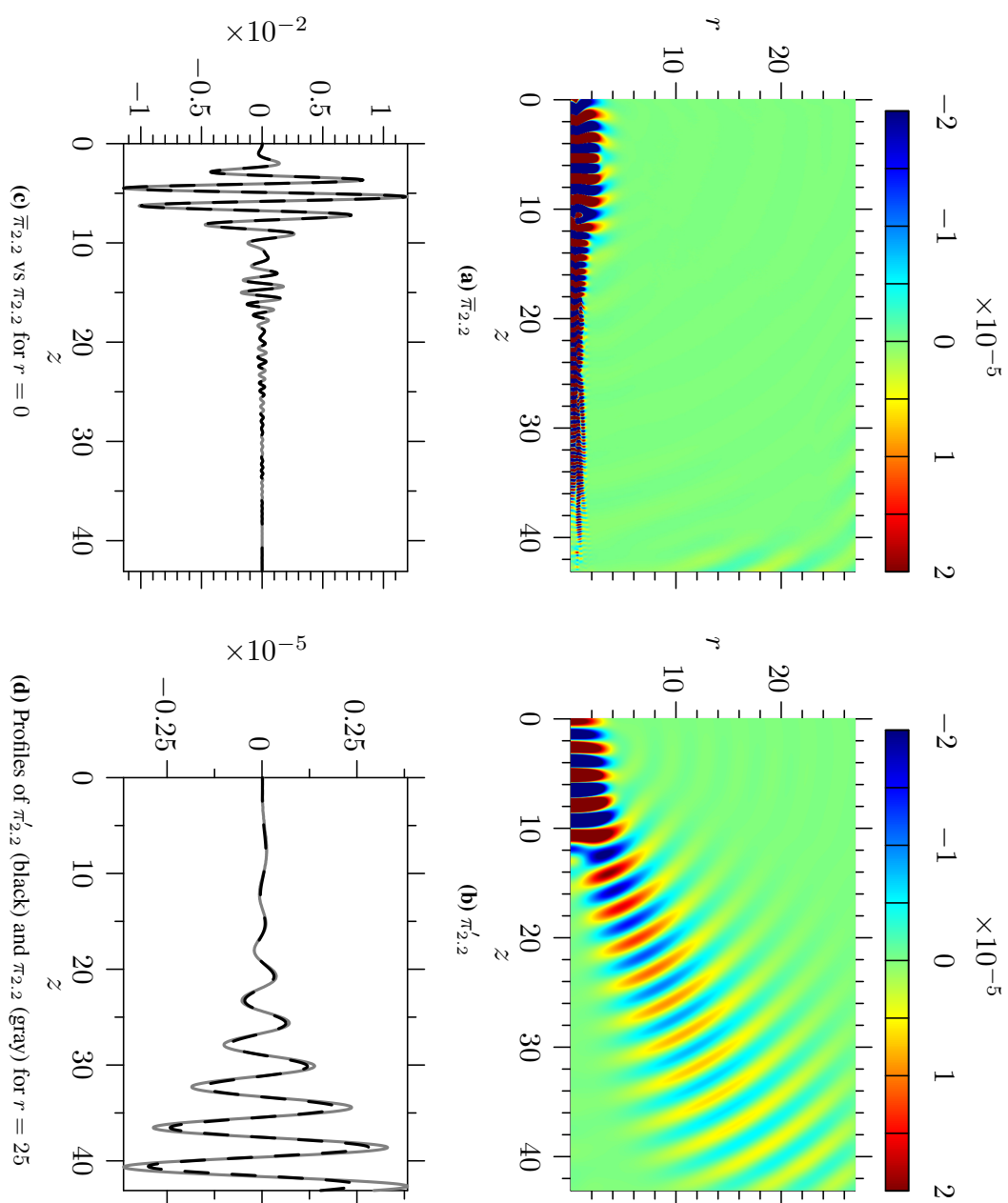


Figure B.10 – Pseudo colour plots and profiles of non radiating pressure $\bar{\pi}_{2,2}$ ((a) and (c)) and radiating pressure $\pi'_{2,2}$ ((b) and (d)) at radiating frequency $\omega_r = 2.2$ and time $t = 0$. The profiles are taken both in the source region (c) and acoustic region (d), at $r = 0$ and $r = 25$ respectively. In the profiles ((c) and (d)), the gray solid line represents $\pi'_{2,2}$. The dashed black line represents $\bar{\pi}_{2,2}$ in (c) and $\bar{\pi}'_{2,2}$ in (d).

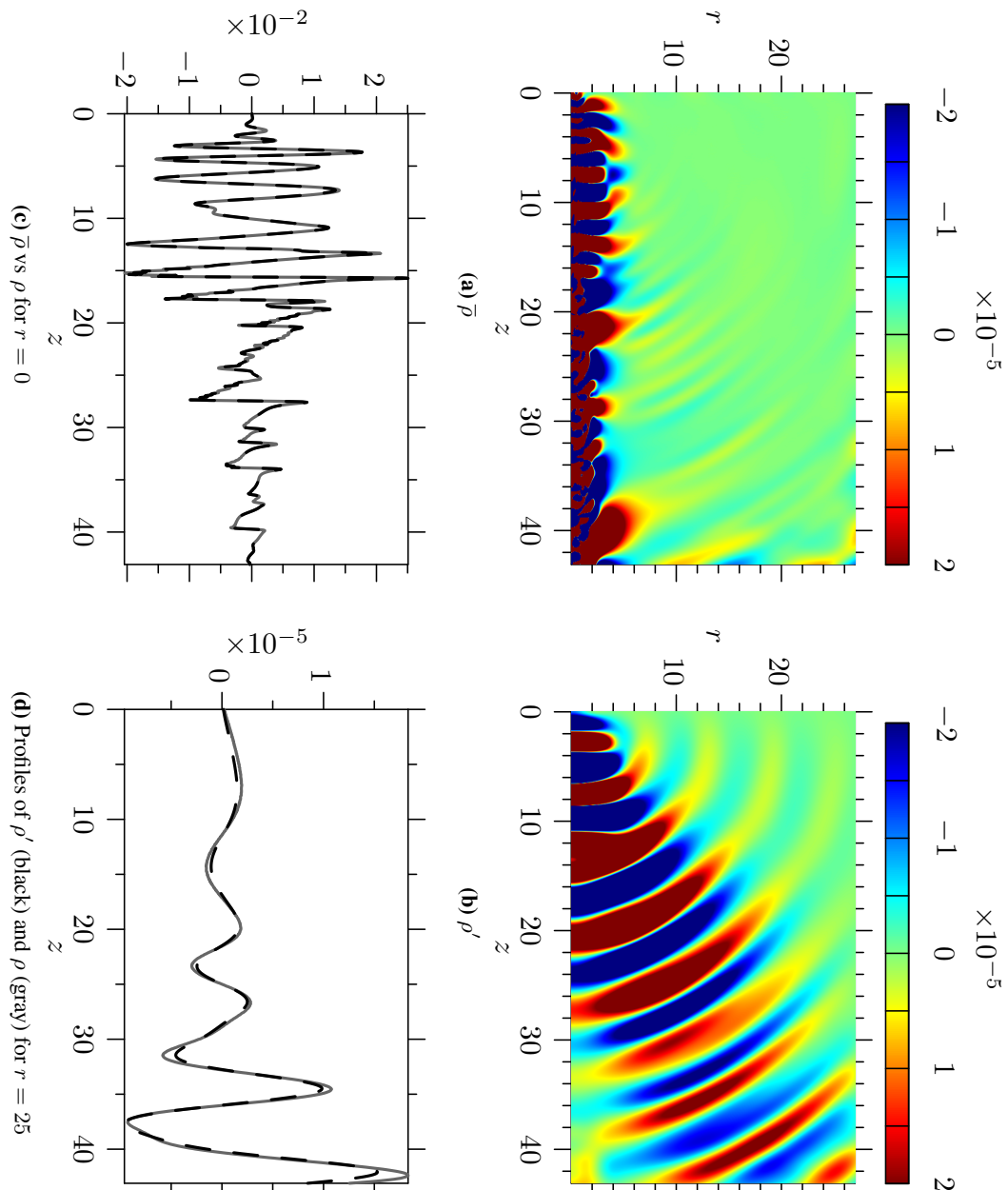


Figure B.11 – Pseudo colour plots and profiles of non radiating density $\bar{\rho}$ ((a) and (c)) and radiating density ρ' ((b) and (d)) at time $t = 0$. The profiles are taken both in the source region (c) and acoustic region (d), at $r = 0$ and $r = 25$ respectively. In the profiles ((c) and (d)), the gray solid line represents $\rho - \rho_0$. The dashed black line represents $\bar{\rho} - \rho_0$ in (c) and ρ' in (d).

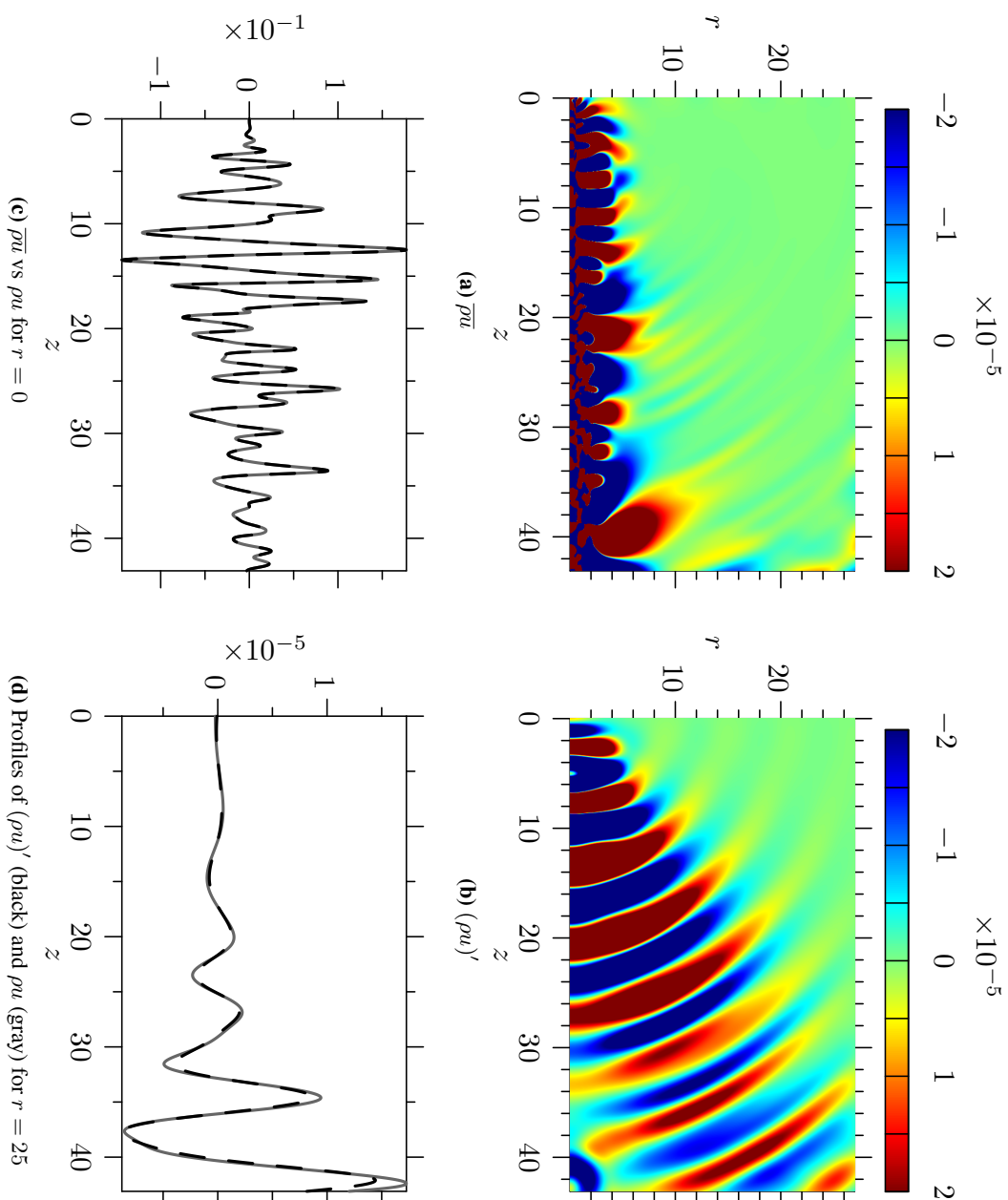


Figure B.12 – Pseudo colour plots and profiles of non radiating axial momentum $\bar{\rho}u$ ((a) and (c)) and radiating axial momentum $(\rho u)'$ ((b) and (d)) at time $t = 0$. The profiles are taken both in the source region (c) and acoustic region (d), at $r = 0$ and $r = 25$ respectively. In the profiles ((c) and (d)), the gray solid line represents $\bar{\rho}u - (\bar{\rho}u)_0$. The dashed black line represents $\bar{\rho} - \rho_0$ in (c) and $(\rho u)'$ in (d).

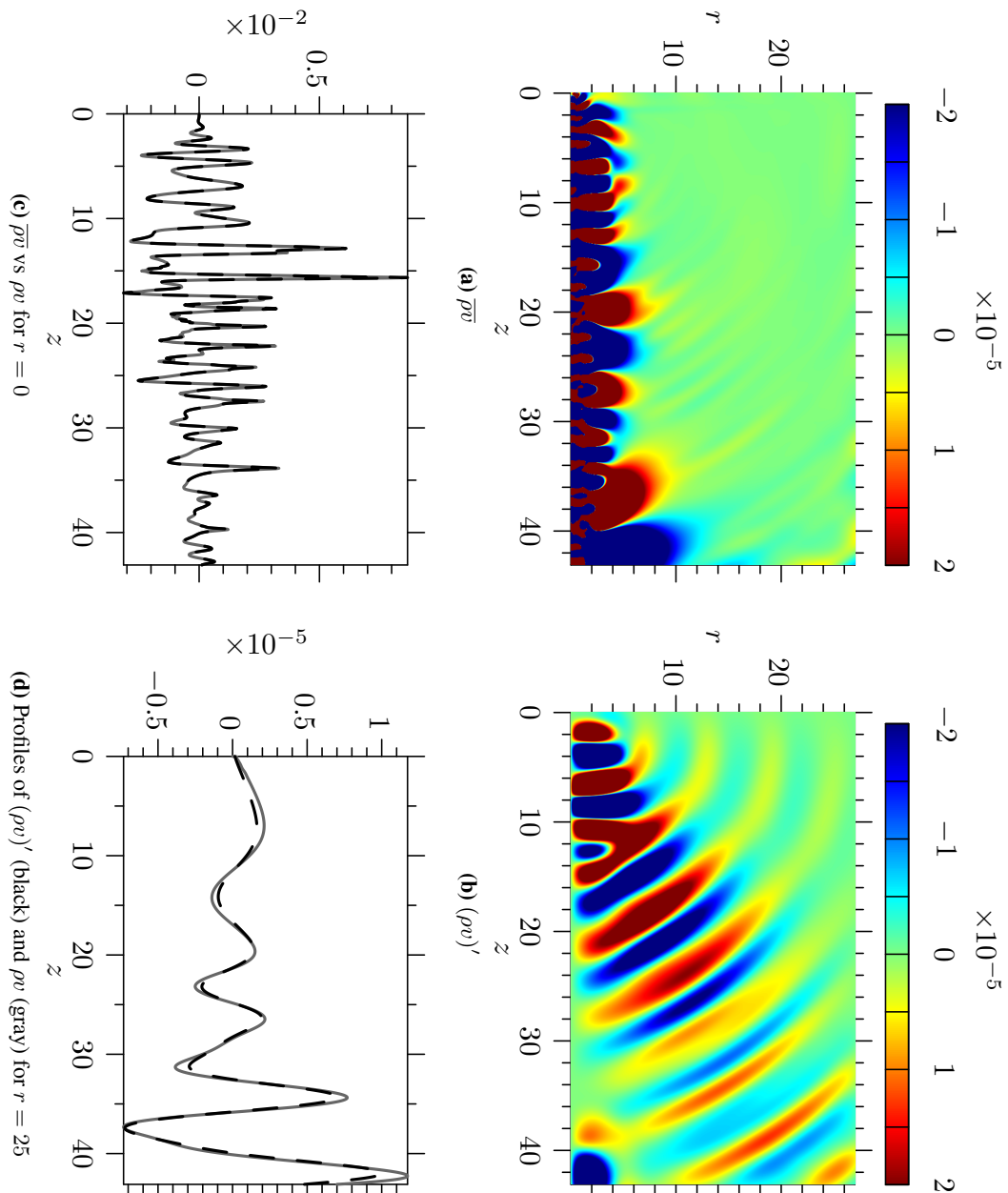


Figure B.13 – Pseudo colour plots and profiles of non radiating axial momentum $\bar{\rho}\bar{v}$ ((a) and (c)) and radiating axial momentum $(\rho v)'$ ((b) and (d)) at time $t = 0$. The profiles are taken both in the source region (c) and acoustic region (d), at $r = 0$ and $r = 25$ respectively. In the profiles ((c) and (d)), the gray solid line represents $\rho v - (\rho v)_0$. The dashed black line represents $\bar{\rho} - \rho_0$ in (c) and $(\rho v)'$ in (d).

B.3 NRBF sources

- Components of radiating source vector $(\mathbf{q}')_{1.0}$ in the time and wavenumber domains: figure B.14.
- Snapshots and profiles of the NRBF sources $(f_{1z})_{1.0}$ and $(f_{1r})_{1.0}$ at frequency 1.0: figure B.15.
- Components of radiating source vector $(\mathbf{q}')_{2.2}$ in the time and wavenumber domains: figure B.16.
- Snapshots and profiles of the NRBF sources $(f_{1z})_{2.2}$ and $(f_{1r})_{2.2}$ at frequency 2.2: figure B.17.
- Validation of the NRBF sources at frequency 1.0, the pressure field: figure B.18.
- Validation of the NRBF sources at frequency 2.2, pressure field: figure B.19.
- Validation of the NRBF sources at frequency 1.2, density, axial momentum and radial momentum: figure B.20.
- Validation of the NRBF sources at frequency 1.0, density, axial momentum and radial momentum: figure B.21.
- Validation of the NRBF sources at frequency 2.2, density, axial momentum and radial momentum: figure B.22.

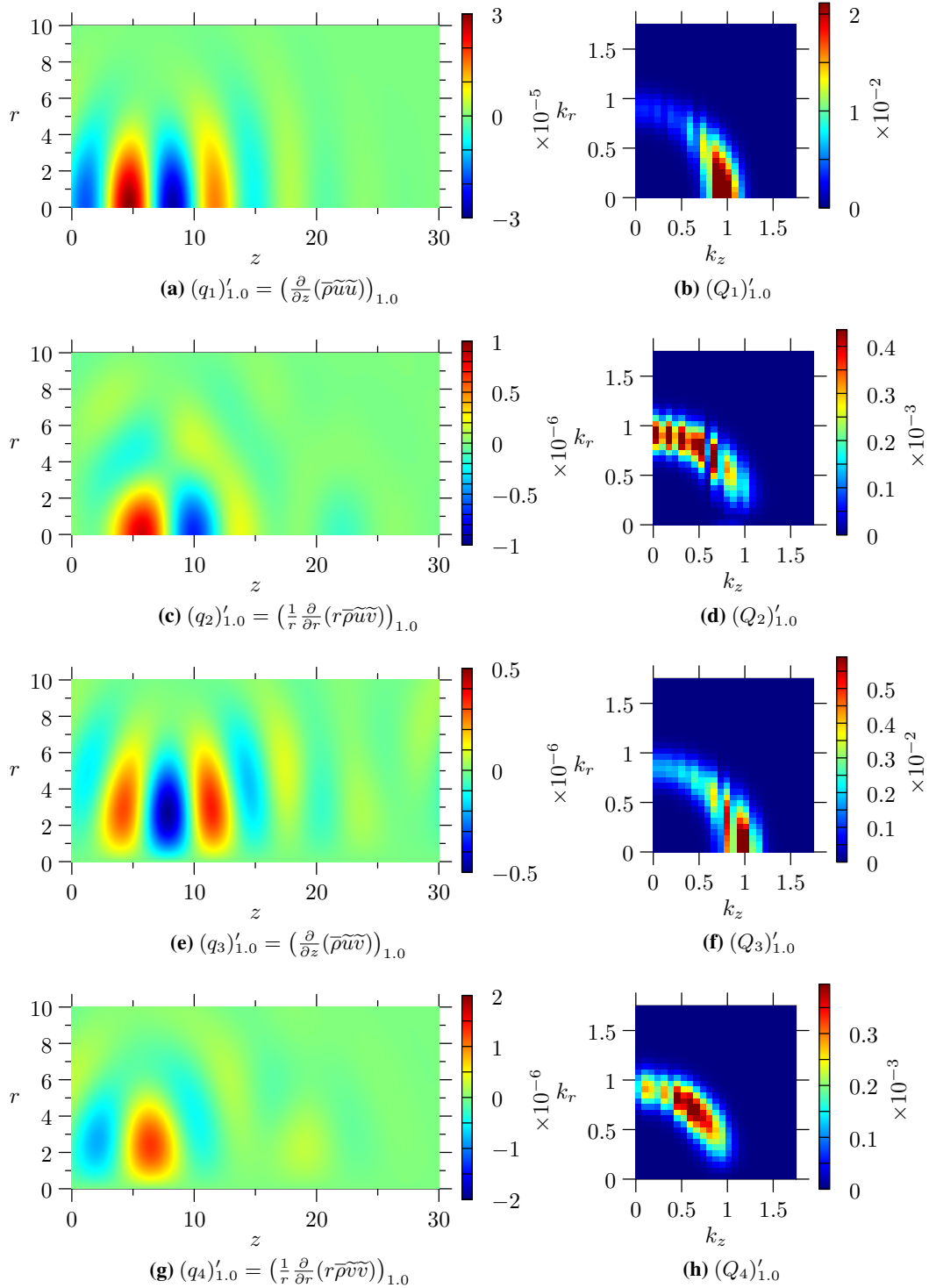


Figure B.14 – Components of radiating source vector $(\mathbf{q}')_{1.0}$ at frequency 1.0 and time $t = 0$, in the space domain (left column) and wavenumber domain (right column).

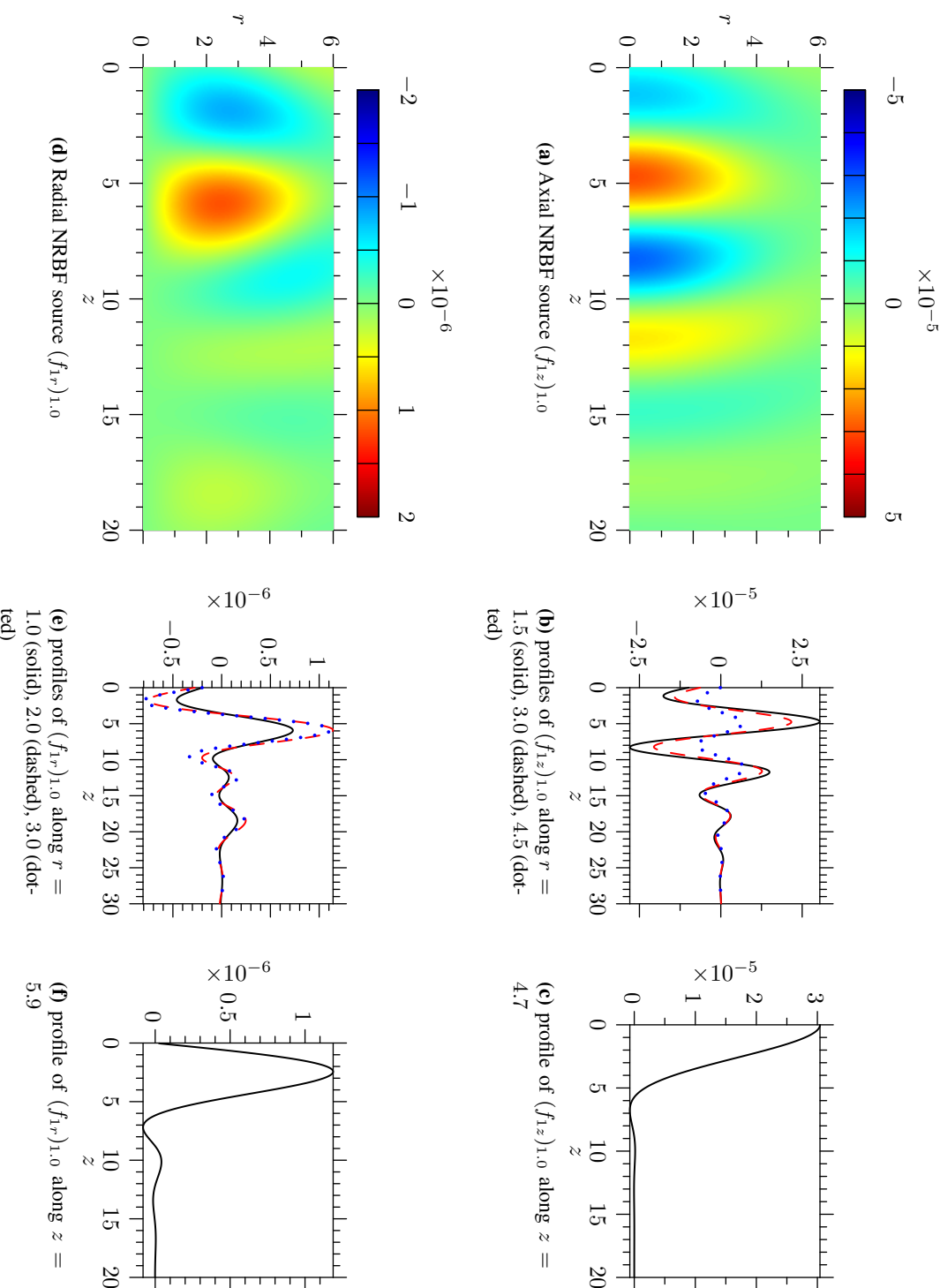


Figure B.15 – NRBFF sources $(f_{1z})_{1,0}$ and $(f_{1r})_{1,0}$ at frequency 1.0 and time $t = 0$.

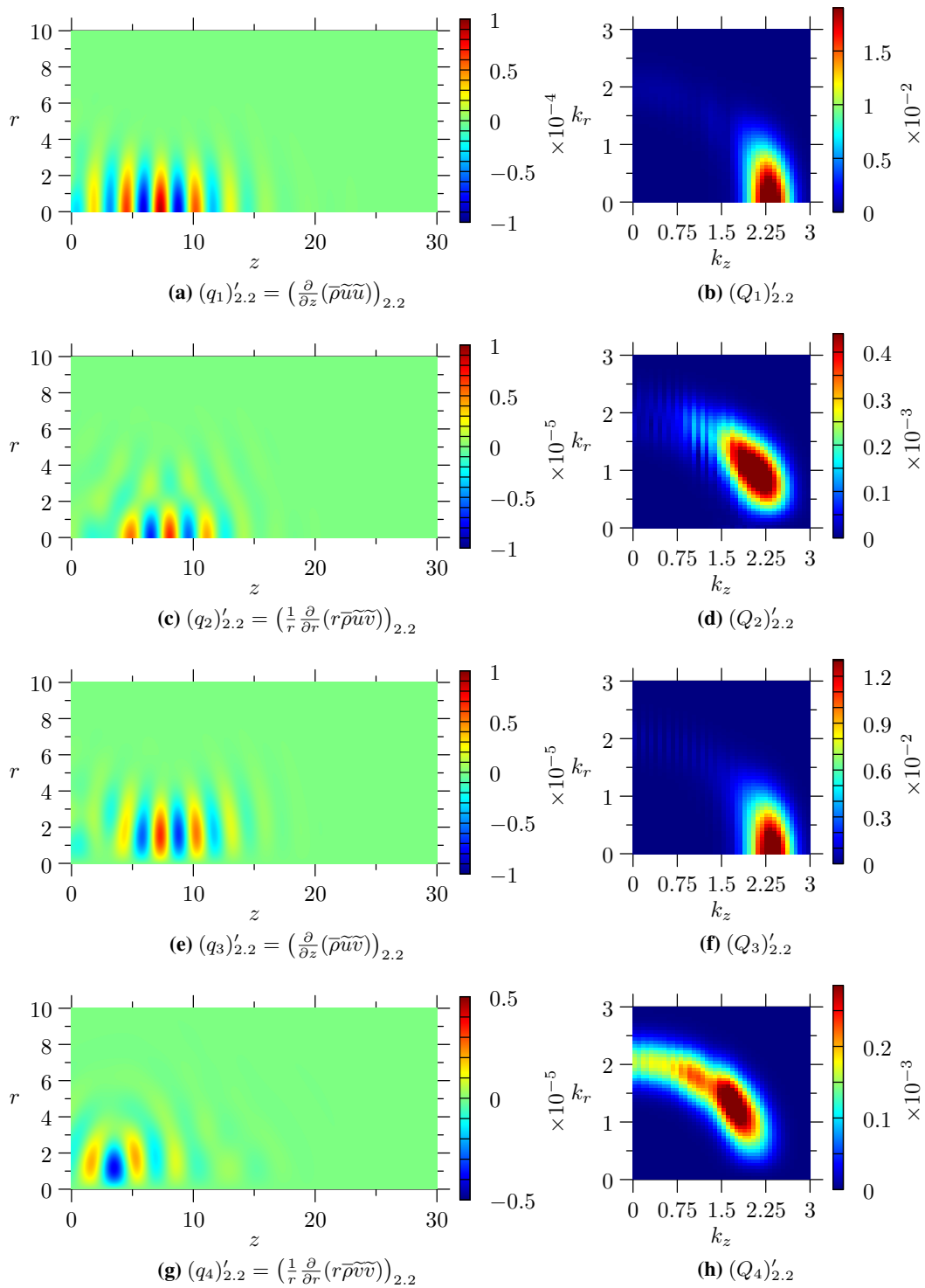


Figure B.16 – Components of radiating source vector $(\mathbf{q}')_{2.2}$ at frequency 2.2 and time $t = 0$, in the space domain (left column) and wavenumber domain (right column).

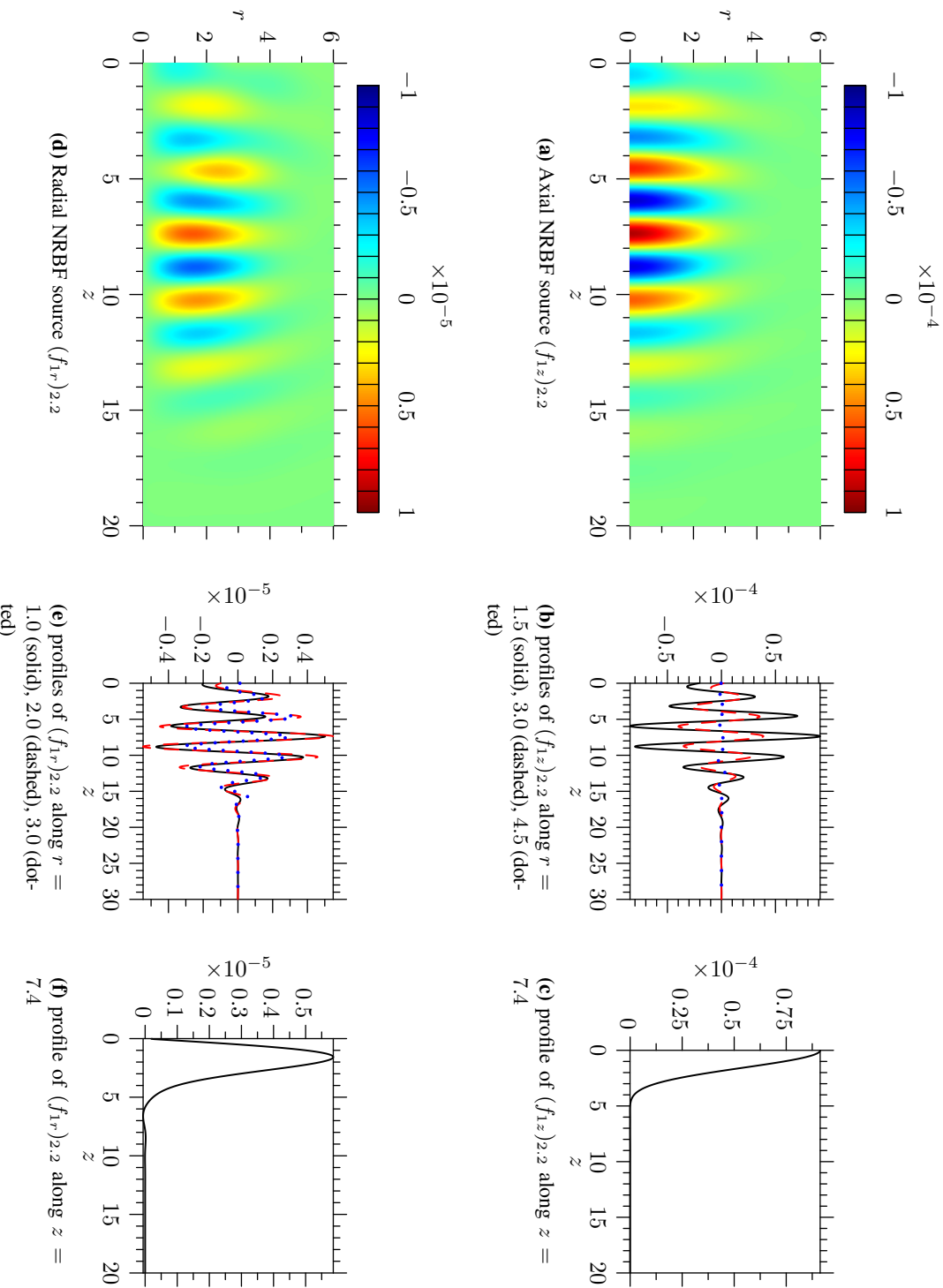


Figure B.17 – NRBFF sources $(f_{1z})_{2,2}$ and $(f_{1r})_{2,2}$ at frequency 2.2 and time $t = 0$.

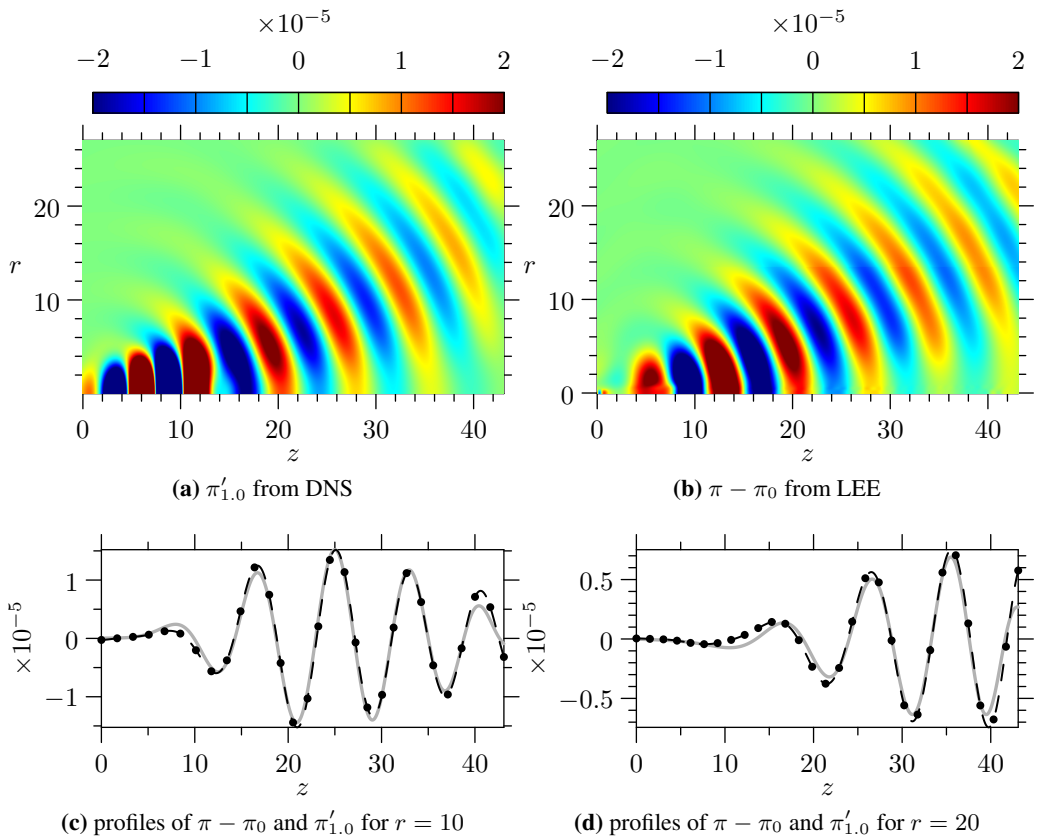


Figure B.18 – Comparison of the pressure field $\pi - \pi_0$, obtained by driving the LEE with the NRBF sources $(f_{1z})_{1.0}$ and $(f_{1r})_{1.0}$, with the radiating pressure field $\pi'_{1.0}$ at frequency 1.0. The bottom figures give profiles along $r = 10$ and $r = 20$: the gray line represents the DNS solution ($\pi_{1.0}$) and the dashed black line with black circles the LEE solution ($\pi - \pi_0$).

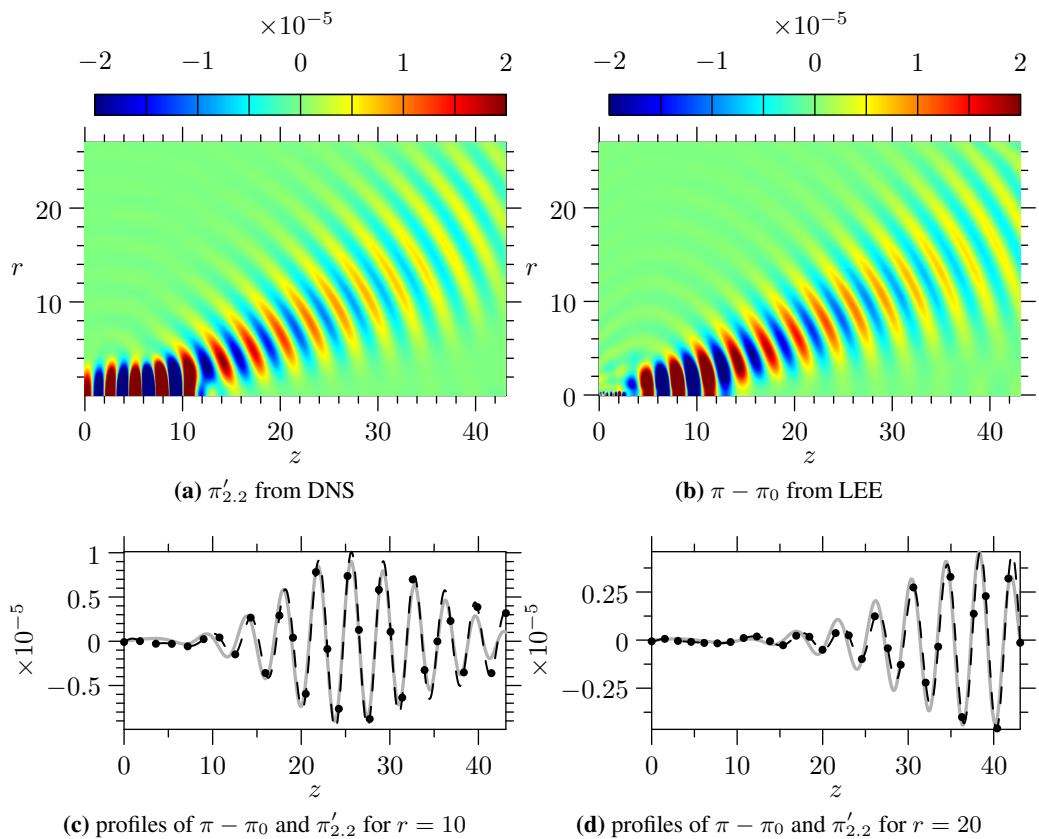


Figure B.19 – Comparison of the pressure field $\pi - \pi_0$, obtained by driving the LEE with the NRBF sources $(f_{1z})_{2.2}$ and $(f_{1r})_{2.2}$, with the radiating pressure field $\pi'_{2.2}$ at frequency 2.2. The bottom figures give profiles along $r = 10$ and $r = 20$: the gray line represents the DNS solution ($\pi'_{2.2}$) and the dashed black line with black circles the LEE solution ($\pi - \pi_0$).

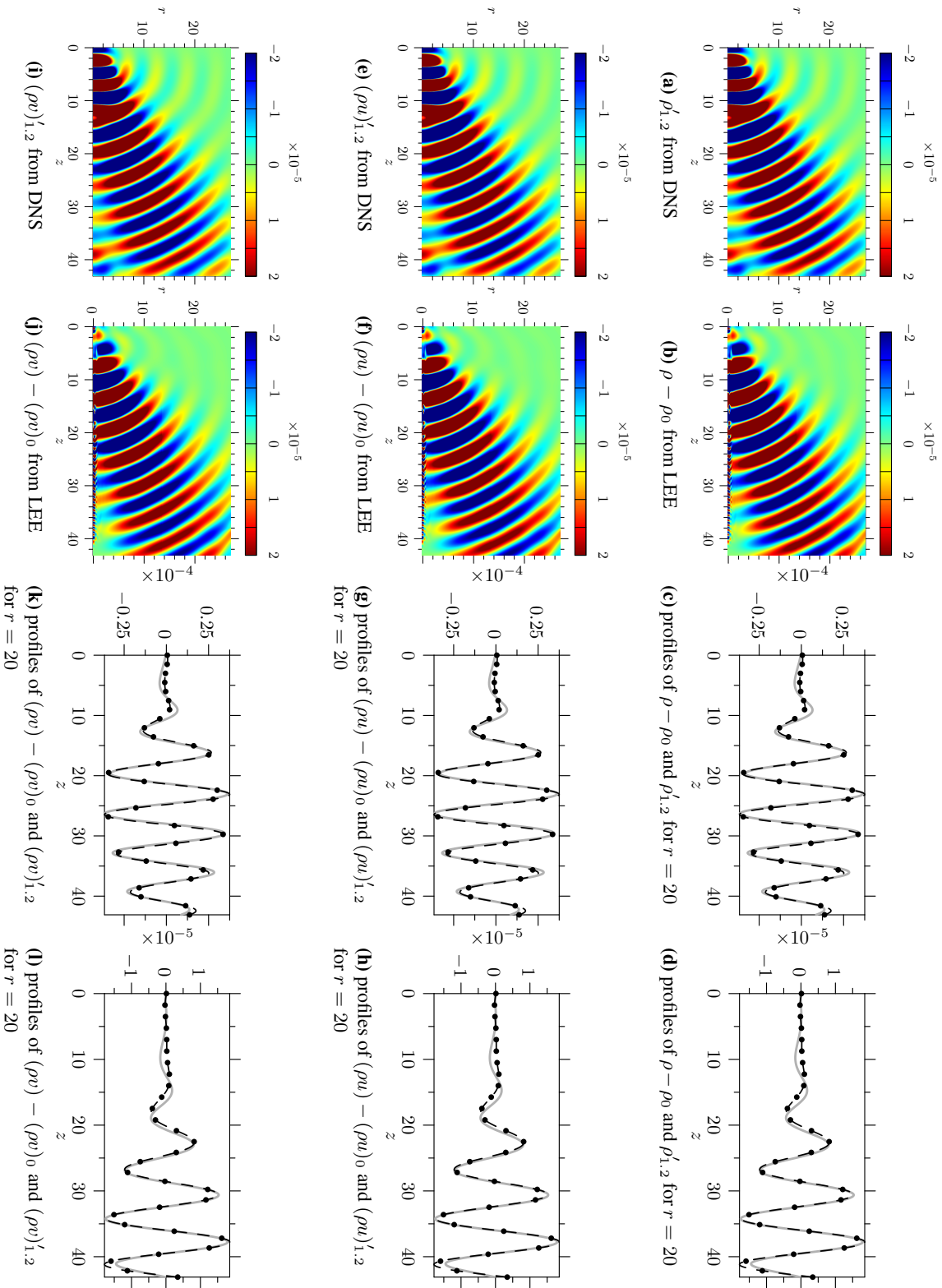


Figure B.20 – Comparison of the density, axial momentum and radial momentum fields obtained by driving the LEE with the NRBf sources $(f_{1z})_{1,2}$ and $(f_{1r})_{1,2}$, with the corresponding fields from the DNS solution. The bottom figures give profiles along $r = 10$ and $r = 20$: gray line represents the DNS solution and the dashed black line with black circles the LEE solution.

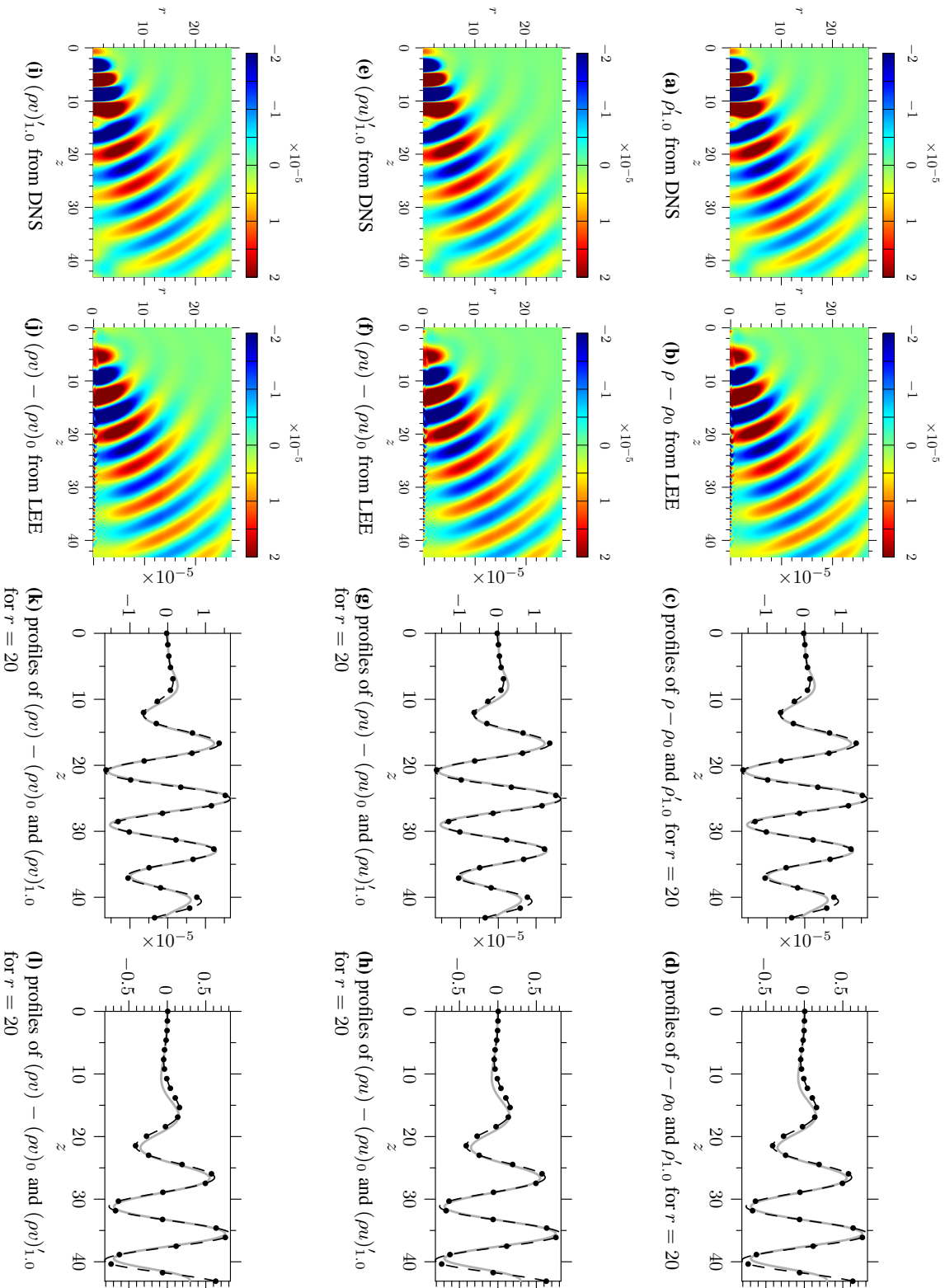


Figure B.21 – Comparison of the density, axial momentum and radial momentum fields obtained by driving the LEE with the NRBf sources $(f_{1z})_{1,0}$ and $(f_{1r})_{1,0}$, with the corresponding fields from the DNS solution. The bottom figures give profiles along $r = 10$ and $r = 20$: gray line represents the DNS solution and the dashed black line with black circles the LEE solution.

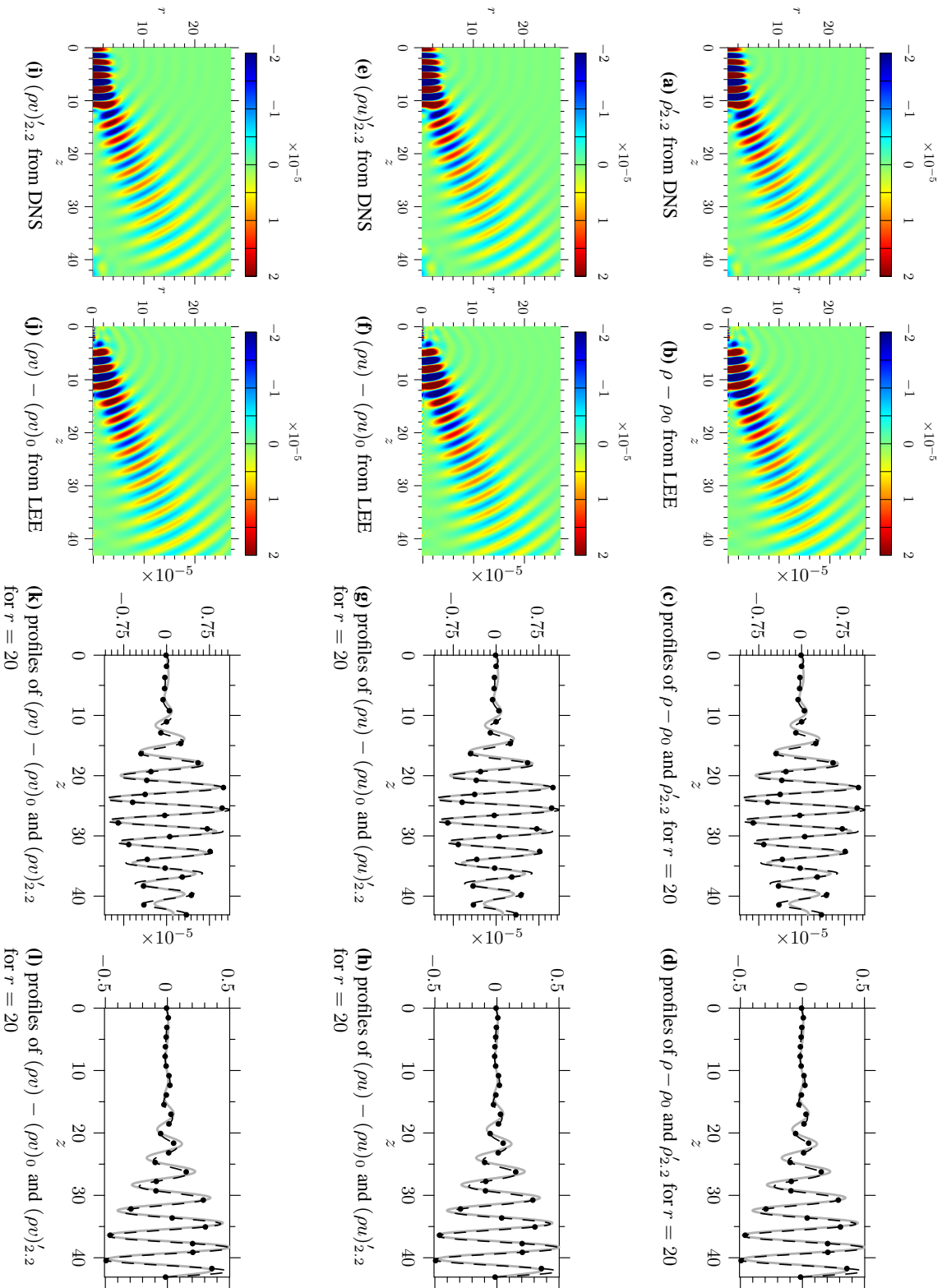


Figure B.22 – Comparison of the density, axial momentum and radial momentum fields obtained by driving the LEE with the NRBf sources $(f_{1z})_{2,2}$ and $(f_{1r})_{2,2}$, with the corresponding fields from the DNS solution. The bottom figures give profiles along $r = 10$ and $r = 20$: gray line represents the DNS solution and the dashed black line with black circles the LEE solution.

B.4 Source based on a time-averaged base flow

Validation of the sources of sound based on a time average base flow at frequency 1.2 for the density, axial momentum and radial momentum: figure B.23.

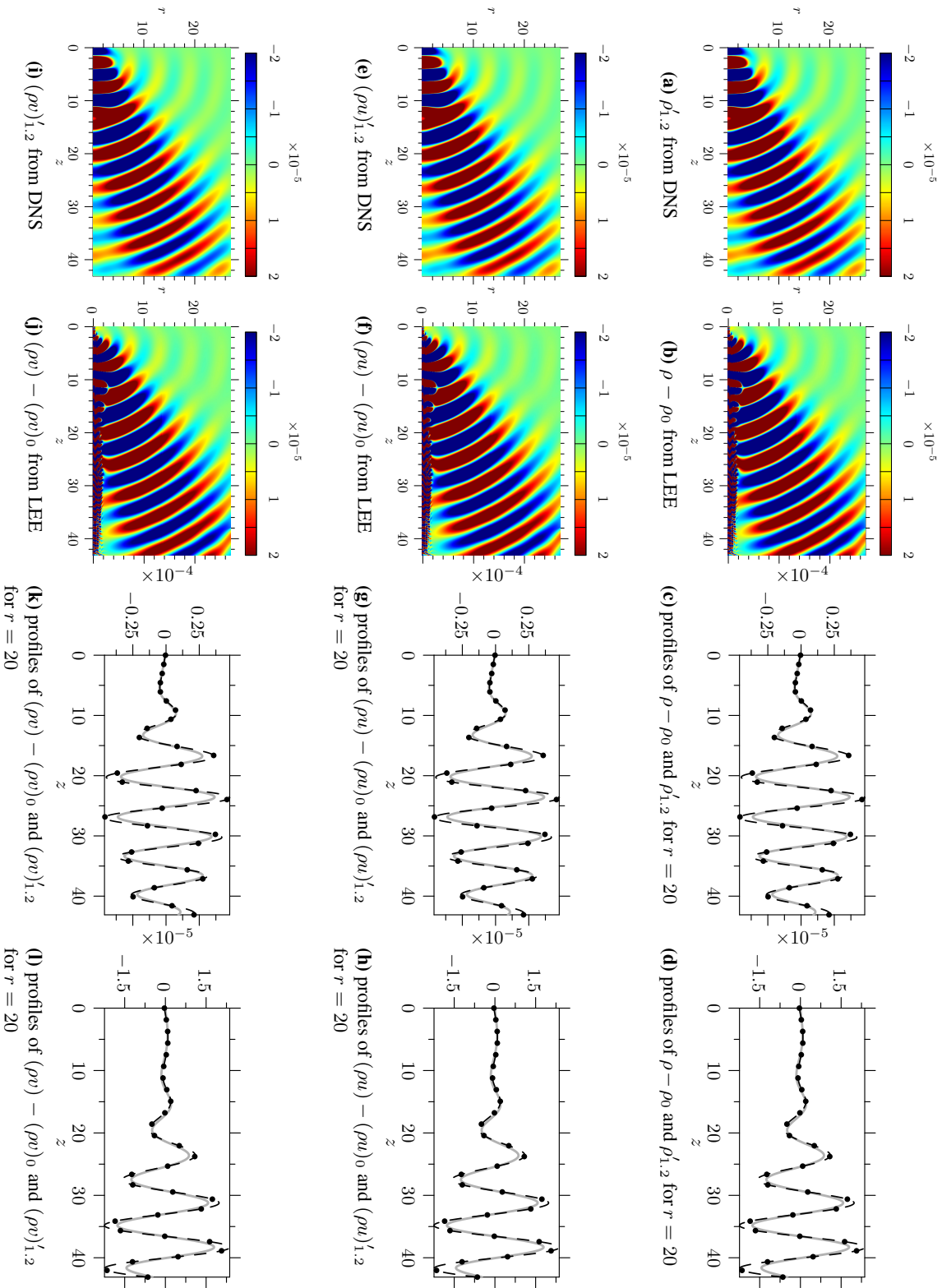


Figure B.23 – Comparison of the density, axial momentum and radial momentum fields obtained by driving the LEE with the time averaged sources $(f_{2z})_{1,2}$ and $(f_{2r})_{1,2}$, with the corresponding fields from the DNS solution. The bottom figures give profiles along $r = 10$ and $r = 20$: gray line represents the DNS solution and the dashed black line with black circles the LEE solution.

Bibliography

Bibliography

- [1] M. J. LIGHTHILL. On Sound Generated Aerodynamically. I. General Theory. *Proceedings of the Royal Society of London*, 211(1107):pp. 564–587, **1952**.
- [2] M. E. GOLDSTEIN. On identifying the true sources of aerodynamic sound. *Journal of Fluid Mechanics*, 526:pp. 337 – 347, **2005**.
- [3] A. P. DOWLING AND T. P. HYNES. Sound generation by turbulence. *European Journal of Mechanics-B/Fluids*, 23(3):pp. 491–500, **2004**.
- [4] E. J. RICHARDS. Research on Aerodynamic Noise from Jets and Associated Problems. *Journal of Royal Aeronautical Society*, 57(509):pp. 318–342, **1953**.
- [5] A. POWELL. A survey of experiments on jet noise. *Aircraft Engineering*, 26(299):pp. 2–9, **1954**.
- [6] M. CABANA, V. FORTUNÉ, AND P. JORDAN. Identifying the radiating core of Lighthill’s source term. *Theoretical and Computational Fluid Dynamics*, 22(2):pp. 87 – 106, **2008**.
- [7] G. M. LILLEY. On the noise from jets. In *AGARD Conference Proceedings No.131 on Noise Mechanisms*, pp. 13 – 1. Brussels, Belgium, **1974**.
- [8] D. C. PRIDMORE-BROWN. Sound propagation in a fluid flowing through an attenuating duct. *Journal of Fluid Mechanics*, 4:pp. 393–406, **1958**.
- [9] H. S. RIBNER. Perspectives on jet noise. *AIAA Journal*, 19 (12):pp. 1513 – 1526, **1981**.
- [10] C. BOGEY, C. BAILLY, AND D. JUVÉ. Computation of flow noise using source terms in linearized Euler’s equations. *AIAA journal*, 40(2):pp. 235–243, **2002**.
- [11] D. G. CRIGHTON. Basic principles of aerodynamic noise generation. *Progress in Aerospace Sciences*, 16:pp. 31–96, **1975**.

- [12] J. B. FREUND. Noise sources in a low-reynolds-number turbulent jet at mach 0.9. *Journal of Fluid Mechanics*, 438:pp. 277 – 305, **2001**.
- [13] C. E. TINNEY AND P. JORDAN. The near pressure field of co-axial subsonic jets. *Journal of Fluid Mechanics*, 611:pp. 175 – 204, **2008**.
- [14] R. EWERT AND W. SCHRÖDER. Acoustic perturbation equations based on flow decomposition via source filtering. *Journal of Computational Physics*, 188(2):pp. 365–398, **2003**.
- [15] G. M. LILLEY. Jet noise classical theory and experiments. In *In NASA. Langley Research Center, Aeroacoustics of Flight Vehicles: Theory and Practice. Volume 1: Noise Sources p 211-289 (SEE N92-10598 01-71)*, volume 1, pp. 211–289. **1991**.
- [16] S. C. CROW AND F. H. CHAMPAGNE. Orderly structure in jet turbulence. *Journal of Fluid Mechanics*, 48(3):pp. 547–591, **1971**.
- [17] H. FUCHS. Measurement of pressure fluctuations within subsonic turbulent jets. *Journal of Sound and Vibration*, 22(3):pp. 361–378, **1972**.
- [18] R. ARMSTRONG. Influence of Mach number on coherent structure relevant to jet noise. *AIAA Journal*, 19:pp. 677–683, **1981**.
- [19] E. MOLLO-CHRISTENSEN, M. A. KOLPIN, AND J. R. MARTUCCELLI. Experiments on jet flows and jet noise far-field spectra and directivity patterns. *Journal of Fluid Mechanics*, 18(02):pp. 285–301, **1986**.
- [20] C. K. W. TAM, M. GOLEBIOWSKI, AND J. M. SEINER. On the two components of turbulent mixing noise from supersonic jets. *Proceedings of the Second AIAA/CEAS Aeroacoustics Conference, State College, PA*, AIAA Paper No. 1996-1716, **1996**.
- [21] K. VISWANATHAN. Analysis of the two similarity components of turbulent mixing noise. *AIAA Journal*, 40(9):pp. 1735 – 44, **2002**.
- [22] C. BOGEY, C. BAILLY, AND D. JUVÉ. Noise investigation of a high subsonic, moderate Reynolds number jet using a compressible large eddy simulation. *Theoretical and Computational Fluid Dynamics*, 16(4):pp. 273–297, **2003**.
- [23] J. L. STROMBERG, D. K. McLAUGHLIN, AND T. R. TROUTT. Flow field and acoustic properties of a Mach number 0.9 jet at a low Reynolds number. *Journal of Sound and Vibration*, 72(2):pp. 159–176, **1980**.
- [24] C. BOGEY AND C. BAILLY. Investigation of downstream and sideline subsonic jet noise using large eddy simulation. *Theoretical and Computational Fluid Dynamics*, 20(1):pp. 23–40, **2006**.

- [25] D. JUVÉ, M. SUNYACH, AND G. COMTE-BELLOT. Intermittency of the noise emission in subsonic cold jets. *Journal of Sound and Vibration*, 71(3):pp. 319 – 32, **1980**.
- [26] M. SCHAFFAR. Direct measurements of the correlation between axial in-jet velocity fluctuations and far field noise near the axis of a cold jet. *Journal of Sound and Vibration*, 64(1):pp. 73–83, **1979**.
- [27] J. PANDA AND R. G. SEASHOLTZ. Experimental investigation of density fluctuations in high-speed jets and correlation with generated noise. *Journal of Fluid Mechanics*, 450:pp. 97–130, **2002**.
- [28] J. PANDA, R. G. SEASHOLTZ, AND K. A. ELAM. Investigation of noise sources in high-speed jets via correlation measurements. *Journal of Fluid Mechanics*, 537:pp. 349–385, **2005**.
- [29] C. BOGEY, S. BARRÉ, D. JUVÉ, AND C. BAILLY. Simulation of a hot coaxial jet: Direct noise prediction and flow-acoustics correlations. *Physics of Fluids*, 21:p. 035105, **2009**.
- [30] N. D. SANDHAM, C. L. MORFEY, AND Z. W. HU. Nonlinear mechanisms of sound generation in a perturbed parallel jet flow. *Journal of Fluid Mechanics*, 565:pp. 1 – 23, **2006**.
- [31] V. SUPONITSKY, N. D. SANDHAM, AND C. L. MORFEY. Linear and nonlinear mechanisms of sound radiation by instability waves in subsonic jets. *Journal of Fluid Mechanics*, 658:pp. 509–538, **2010**.
- [32] K. VISWANATHAN. Investigation of noise source mechanisms in subsonic jets. *AIAA Journal*, 46(8):pp. 2020 – 2032, **2008**.
- [33] D. RONNEBERGER AND U. ACKERMANN. Experiments on sound radiation due to non-linear interaction of instability waves in a turbulent jet. *Journal of Sound and Vibration*, 62(1):pp. 121–129, **1979**.
- [34] J. E. FFOWCS WILLIAMS AND D. L. HAWKINGS. Sound Generation by Turbulence and Surfaces in Arbitrary Motion. *Philosophical Transactions for the Royal Society of London. Series A, Mathematical and Physical Sciences*, 264(1151):pp. 321–342, **1969**.
- [35] G. M. LILLEY. The Generation and Radiation of Supersonic Jet Noise. Vol. IV - Theory of Turbulence Generated Jet Noise, Noise Radiation from Upstream Sources, and Combustion Noise. Part II: Generation of Sound in a Mixing Region. *US Air Force Aero Propulsion Lab., AFAPL-TR-72-53, July*, **1972**.
- [36] C. K. W. TAM. Supersonic jet noise. *Annual Review of Fluid Mechanics*, 27:pp. 17 – 43, **1995**.

- [37] A. AGARWAL, P. J. MORRIS, AND R. MANI. Calculation of sound propagation in nonuniform flows: Suppression of instability waves. *AIAA Journal*, 42(1):pp. 80 – 88, **2004**.
- [38] M. E. GOLDSTEIN. *Aeroacoustics*. McGraw-Hill International Book Co., **1976**.
- [39] M. E. GOLDSTEIN. A theoretical basis for identifying the sound sources in a turbulent flow. *International Journal of Aeroacoustics*, 8(4):pp. 283–300, **2009**.
- [40] M. E. GOLDSTEIN. A generalized acoustic analogy. *Journal of Fluid Mechanics*, 488:pp. 315 – 33, **2003**.
- [41] C. L. MORFEY AND M. C. M. WRIGHT. Extensions of lighthill's acoustic analogy with application to computational aeroacoustics. *Proceedings of the Royal Society of London, Series A (Mathematical, Physical and Engineering Sciences)*, 463(2085):pp. 2101 – 2127, **2007**.
- [42] D. DUFFY. *Green's functions with applications*. CRC Press, **2001**.
- [43] M. S. HOWE. *Theory of vortex sound*. Cambridge Univ Pr, **2003**.
- [44] G. N. WATSON. *A treatise on the theory of Bessel functions*. Cambridge Univ Pr, **1995**.
- [45] K. SHIN AND J. HAMMOND. *Fundamentals of signal processing for sound and vibration engineers*. Wiley, **2008**.
- [46] V. SUPONITSKY AND N. D. SANDHAM. Nonlinear mechanisms of sound radiation in a subsonic flow. *AIAA paper 2009-3317*, **2009**.
- [47] M. GUIZAR-SICAIROS AND J. C. GUTIÉRREZ-VEGA. Computation of quasi-discrete Hankel transforms of integer order for propagating optical wave fields. *Journal of the Optical Society of America A*, 21(1):pp. 53–58, **2004**.
- [48] M. ABRAMOWITZ AND I. A. STEGUN, editors. "Zeros." *9.5 in Handbook of Mathematical Functions with Formulas, Graphs, and Mathematical Tables*, 9th printing. Dover Publications, **1972**.
- [49] A. CLINE. FITPACK-software package for curve and surface fitting employing splines under tension. *Department of Computer Science, University of Texas, Austin, Texas*, **1981**.
- [50] H. LANGTANGEN. *Python scripting for computational science*. Springer Verlag, **2004**.
- [51] T. OLIPHANT. Guide to NumPy, **2006**.

- [52] E. JONES, T. OLIPHANT, P. PETERSON, ET AL. SciPy: Open source scientific tools for Python, **2001**–.
- [53] M. METCALF AND J. REID. *Fortran 90 explained*. Oxford University Press, Inc. New York, NY, USA, **1990**.
- [54] P. PETERSON. F2PY: a tool for connecting Fortran and Python programs. *International Journal of Computational Science and Engineering*, 4(4):pp. 296–305, **2009**.
- [55] C. K. W. TAM AND J. C. WEBB. Dispersion-relation-preserving finite difference schemes for computational acoustics. *Journal of Computational Physics*, 107(2):pp. 262 – 81, **1993**.
- [56] C. BOGEY AND C. BAILLY. A family of low dispersive and low dissipative explicit schemes for flow and noise computations. *Journal of Computational Physics*, 194(1):pp. 194 – 214, **2004**.
- [57] N. D. SANDHAM AND H. S. SANDHU. Boundary conditions for spatially growing compressible shear layers. Technical Report QMW-EP-1100, Faculty of Engineering, Queen Mary and Westfield College, University of London, **1994**.
- [58] M. ABRAMOWITZ AND I. A. STEGUN, editors. "Bessel functions of integer order." 9.1 in *Handbook of Mathematical Functions with Formulas, Graphs, and Mathematical Tables*, 9th printing. Dover Publications, **1972**.